POLITECNICO
MILANO 1863

School of Civil, Environmental and Land Management Engineering

MSc in Civil Engineering – Hydraulics

LAND SURFACE TEMPERATURE DOWNSCALING TECHNIQUES AND THEIR APPLICATION FOR THE CALIBRATION OF A DISTRIBUTED HYDROLOGICAL MODEL IN A CHINESE INLAND RIVER BASIN

Supervising professor

Ing. Chiara CORBARI

Co-supervising professor

Prof. Marco MANCINI

Student

Nicola PACIOLLA

Academic Year 2016-2017

Contents

List of images

List of tables

Abstract

The exponential growth of Remote Sensing technologies has open new frontiers for hydrology, allowing the accurate study of areas that were close to inaccessible only some decades ago.

In this study, a distributed hydrological model, FEST-EWB, has been calibrated in the Heihe river basin, an inland river basin in China. The calibration has been conducted using Land Surface Temperature data obtained from Remote Sensing. The model is then to be validated with evapotranspiration data from ground measurements and from a Chinese remote sensing model.

Land Surface Temperature data is easily retrieved using Remote Sensing, and is available in different time- and spatial-resolutions. In the first part of this study, a survey of some of these sources has been conducted. LST data of the basin, coming from the available data with the highest spatial but low temporal resolution (LANDSAT 7 ETM+), has been compared with low resolution daily Terra's MODIS data and two temperature downscaling algorithms (StarFM and Kustas) over 11 test dates in year 2012. The results have also been filtered through land cover classification and lighting degree ("in light" or "in shadow") of each pixel.

After having chosen Terra's MODIS as the best LST source, its data have been applied for the calibration of the hydrological model: soil and vegetation parameters have been modified in order to fit the forecasts of the model to the actual, remotely sensed, LSTs.

Sintesi

Il progressivo sviluppo delle tecniche di telerilevamento ha aperto nuove frontiere in moltissimi campi, fra i quali è compresa l'idrologia. Queste tecniche, infatti, hanno reso possibile la raccolta dati in zone sino a qualche decennio fa assai poco conosciute. Nel caso dei modelli idrologici, la calibrazione è tradizionalmente effettuata impiegando dati di portata ottenuti dalle stazioni idrometriche poste lungo le aste dei fiumi. Tuttavia, specie in anni recenti, si è andata sviluppando la tecnica di calibrazione tramite LST (Land Surface Temperature, Temperatura Superficiale Terrestre). Quest'ultima, a differenza dei dati di portata, è facilmente ottenibile tramite satellite, in diversi formati e con diverse risoluzioni temporali e spaziali, a seconda delle necessità.

Scopo di questo studio è determinare quale sia la miglior fonte di LST per la calibrazione del modello idrologico distribuito FEST-EWB sul bacino endoreico del fiume Heihe, in Cina. In seguito, è stata effettuata la calibrazione del modello impiegando le misure di LST scelte in precedenza. Infine, è da portare avanti una procedura di validazione del modello tramite dati di evapotraspirazione provenienti da misurazioni al terreno ed un modello cinese che utilizza dati da satellite.

Nella prima parte, ci si è concentrati sull'analisi delle diverse fonti di LST. In particolare, si sono studiate quattro categorie di LST: i dati con risoluzione 30 m dell'ETM+ (strumento a bordo del satellite LANDSAT 7); i dati a risoluzione 1000 m del MODIS (strumento del satellite Terra); i dati ottenuti a 30 m di risoluzione dall'algoritmo StarFM; i dati ottenuti a 30 m di risoluzione dall'algoritmo di Kustas.

Ciascuna di queste fonti è descritta nei suoi punti forti e nelle sue debolezze; il LANDSAT è risultato il dato più preciso, ma la sua rada frequenza temporale e l'impossibilità di coprire tutto il bacino in un'unica immagine lo rendono poco appetibile per la calibrazione del modello su questo bacino. Per determinare quale degli altri tre metodi (che forniscono

un'immagine di LST ogni giorno) sia il più preciso, si è svolto un confronto con il LANDSAT. Questo confronto ha riguardato una zona centrale del bacino, in 11 date dell'anno di interesse per questo studio, il 2012.

L'analisi è stata condotta sia in termini generali, sia filtrando i risultati attraverso 6 macro-categorie di copertura del suolo e 2 possibili stati di illuminazione ("pixel illuminato" o "pixel in ombra"). Il dato del MODIS (l'unico originalmente a 1000 m e ri-scalato a 30 m per il confronto) si è rivelato essere il più preciso ed è stato quindi impiegato nella successiva calibrazione.

La fase di calibrazione ha previsto che i dati riguardanti il suolo e la vegetazione fossero modificati a più riprese per cercare di adattare le temperature superficiali previste dal modello a quelle effettivamente misurate dal MODIS.

Introduction

Research Contest

Studying the mechanics of river basins is the first step in optimizing the use of the water resource [Li et al, 2015] [Zhang et al, 2017]. Understanding each mass transfer in the mass balance can be a useful tool with both assigning water quotas for irrigation [Wang et al, 2015] and a helpful instrument to forecast future water availability [Yin et al, 2017].

Numerous models exist that sum up each contribution to the water budget [Arnold et al, 2012], ranging from the simplest expressions (which describe the output as a fixed fraction of the input) to more complex systems which feature both a mass and an energy balance equation [Corbari-Ravazzani-Mancini, 2012] [Corbari et al, 2010] [Wang et al, 2009].

Some approaches compute the river runoff as a result of energy balances which need Land Surface Temperature (LST) as an input variable. These are divided in one-source schemes, which lump all land cover types as one (such as SEBAL [Bastiaanssen et al., 1998] or SEBS [Su, 2002]), and two-source ones, which distinguish bare soil from vegetated one (like TSEB, [Norman et al, 1995]; [Yang et al, 2015]). More comprehensive models work on a number of input parameters to compute all energy and water balances in a continuous way. Thus, LST becomes an output variable, suitable for calibration and validation needs. FEST-EWB (Flash-Flood Event-based Spatially-distributed rainfall-runoff Transformation – Energy/Water Balance), developed by [Corbari-Ravazzani-Mancini, 2012], is one such model.

Remote sensing has hugely developed in recent years, with new image products that fit a wide range of possible applications: estimating surface temperature for lakes [Zhang et al, 2014] and rivers [Handcock et al, 2012]; estimating river discharge [Tarpanelli et al, 2011]; modelling energy and mass fluxes [Corbari et al, 2012], [Corbari et al, 2015]; mapping soil moisture [Campo et al, 2011]; monitoring snow coverage [Corbari et al, 2008]; identifying vegetation dynamics [Yin et al, 2015]; understanding the role of land cover in energy transfers [Parida et al, 2007].

Many hydrological models are calibrated employing flow discharge time series. Some allow for a double-calibration, involving also Land Surface Temperature (LST) data [Corbari-Mancini, 2014] [Corbari et al, 2012]. Developing accuracy in this type of calibration is key to understand basins for which discharge data is lacking or has low quality. LST data are available with different spatial resolutions and time frequencies, and the debate on which is the best-suited for this kind of studies is still open.

Some studies (for example concerning cultivated areas organised in little fields [Platonov et al, 2008] [Farg et al, 2016] [Senay et al, 2016], [Cuenca et al, 2013]) may require daily, high-resolution data. As high spatial resolution is often associated with (relatively) low temporal frequency, the need for the development of temperature downscaling techniques arises. The problem may be tackled in two ways: either data from different satellite instruments is combined based on statistic and physically-based principles [Gao et al, 2006] [Gutierrez et al, 2012] [Hamlet et al, 2010] [Pang et al, 2017] [Weng et al, 2014], or a relation is established between the desired variable and other satellite products, which in turn are available at the desired resolution [Kustas et al, 2003].

The combination of climate change, population growth and urbanization calls for a direct tackling of the water resource problem [Wang et al, 2015] [Yan et al, 2014] [Wu et al, 2014] [Geng et al, 2015] [Huang et al, 2017] [Liu et al, 2013]. Better understanding the dynamics described in this study is the first step in doing so.

Thesis goals

The goal of this study can be summarized as such:

To apply the FEST-EWB hydrological model to the Heihe River Basin in China, calibrating it with Land Surface Temperature data, retrieved using Remote Sensing. A number of different LST sources will be compared, in order to determine the most useful.

Outline

The first chapter of this study, called "Methodology", introduces the instruments of this analysis. In its first section, the hydrological model FEST-EWB is explained, with a complete description of its ruling equations and needed parameters. In the second section, the four LST sources are described in their origin and characteristics.

The second chapter, called "Case Study Overview", surveys the Heihe River basin. First, a historical-political overview, then a detailed description of the basin's geomorphology, pedology and its climatic and meteorological conditions.

The third chapter of the study, called "LST Downscaling, a performance comparison", contrasts the LST data provided by three of the available sources with the data from LANDSAT 7 ETM+, which are the ones with the highest spatial resolution but have low temporal frequency.

The fourth chapter, called "Model Calibration", illustrates the calibration process of the model, following its statistics and the evolution of the soil and vegetation parameters.

The fifth chapter, called "Conclusions & Recommendations", gathers up all the results of the study and proposes further work on the subject.

Chapter 1

Methodology

In this chapter, the methodology followed by the thesis is described. The first part deals with the description of the hydrological model FEST-EWB and its main processes and variables, in the second part the analysis and downscaling of satellite images of Land Surface Temperature are described.

1.1 FEST-EWB hydrological model

1.1.1 Overview

The FEST-EWB (*Flash-flood Event-based Spatially-distributed rainfall-runoff Transformation – Energy and Water Balance*) is a hydrological model which converts rainfall and other inputs, such as snowmelt, into river runoff [Mancini, 1990] [Corbari et al., 2011]. Being a distributed model, it closes each water and energy balance at pixel level, considering a certain soil depth (until an impermeable layer below) and the lower atmosphere immediately above.

Each vertical mass/energy flux is computed to obtain the runoff volume from the single cell, which is then channelled through the hydrologic network established by the elevation raster, in the form of a Digital Elevation Model (DEM).

In order to compute the runoff, the model applies the SCS-CN (Soil Conservation Service – Curve Number), updating the retention potential of each cell before each precipitation event and employing the Muskingum-Cunge algorithm.

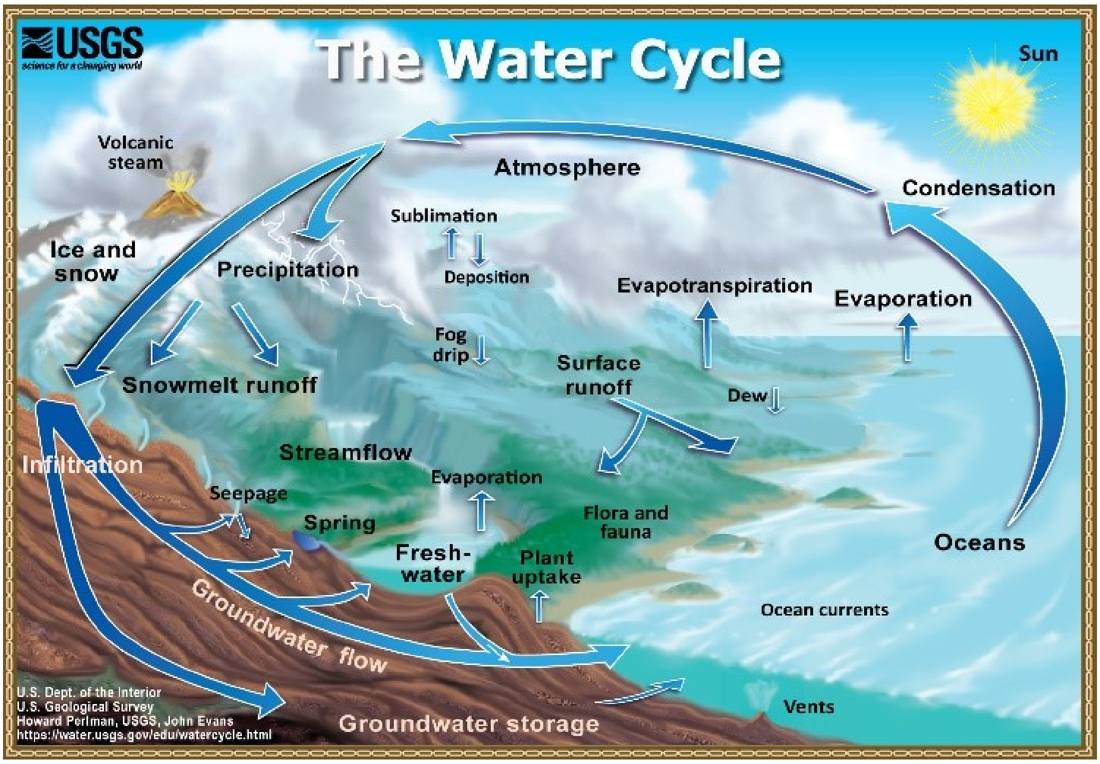

Figure 2 *- The Water Cycle [available at https://water.usgs.gov/edu/watercycle.html]*

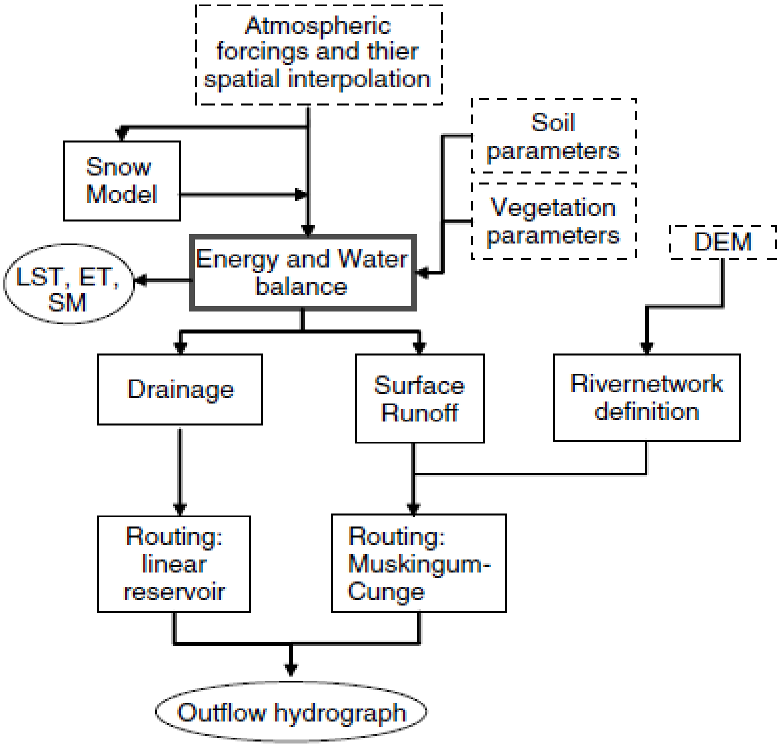

Figure 1 *- FEST-EWB scheme [from Corbari-Ravazzani-Mancini, 2012]*

The model requires some input data:

- Atmospheric data, like air temperature, wind velocity, precipitation or air humidity
- Digital Elevation Model (DEM)
- Soil data, as for example hydraulic conductivity or soil depth
- Vegetation data, such as Leaf Area Index (LAI) or vegetation height

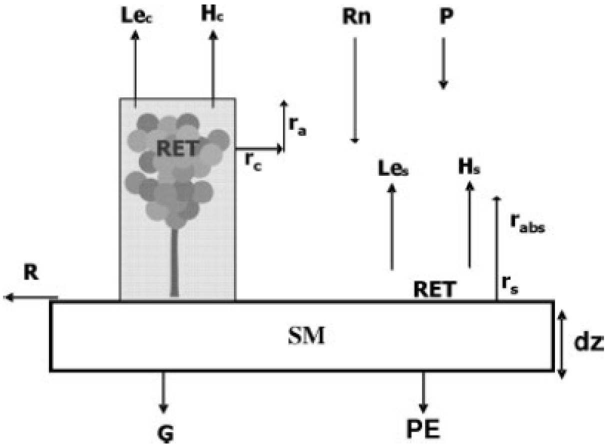

Figure 3 *- The elements of the mass and energy balances [Corbari-Ravazzani-Mancini, 2012]*

The model is based on a system of two equations, the mass and the energy balances, whose variables are the cell runoff (R) and the Representative Equilibrium Temperature (RET). The latter is the surface temperature that closes the balance. Both variables can be compared with measurements for the calibration process.

$$\begin{cases} \dfrac{\partial SM}{\partial t} = \dfrac{P - R - PE - ET}{dz}, & mass\ balance \quad (1) \\ Rn - G - (Hs + Hc) - (LEs + LEc) = \dfrac{\Delta W}{\Delta t}, & energy\ balance \quad (2) \end{cases}$$

1.1.2 Water balance equation

The first equation weighs the water mass fluxes through the cell unit. Any temporal variation of Soil Moisture (SM) results from the imbalance of four main contributes, such as:

(a) Rainfall (P), the amount of water effectively reaching the ground; it can be gathered using data from meteorological stations or satellites

(b) Runoff flux (R), the superficial fraction of the total runoff, usually far bigger than its topsoil counterpart

(c) Deep Percolation (PE), the amount of water "lost" to lower aquifers, depends on soil permeability and amount of water in soil

(d) Evapotranspiration (ET), the combination of the water directly evaporated from the soil and all the collecting surfaces (E) and the water transferred to the atmosphere by the canopy during the photosynthesis process (T).

1.1.3 Energy Balance Equation

The amount of energy "stored" in the single cell unit can vary over time because of the energy fluxes both incoming and outgoing. However, at a spatial resolution as low as the one used in this study (around 1000m), such a variation can be safely assumed to be negligible. This means that the net balance of the other contributions will be null.

The net radiation (Rn) involves the balance between incoming and outgoing short-wave and long-wave radiation.

$$Rn = Rn^{(longwave)} + Rn^{(shortwave)} \tag{3}$$

Longwave radiation is associated with wavelengths bigger than the infrared. This makes them the chief emission radiating from the Earth itself or the atmosphere immediately above the ground. Thus, the net longwave radiation comes from the positive contribution of the atmosphere aboveground (of temperature T_A) and the negative one of the soil (RET), through the application of Stefan-Boltzmann law:

$$Rn^{(longwave)} = \varepsilon_A \sigma T_A^4 - \varepsilon_{soil} \sigma RET^4 \tag{4}$$

Where the varying emissivity ε accounts for the lower atmosphere and the topsoil not being black bodies; σ, instead, is Stefan-Boltzmann's constant ($5.67\ 10^{-8}$ W m^{-2} K^{-4}).

Short-wave radiation involves wavelengths between the near-ultraviolet (NUV) and near-infrared (NIR) spectra (λ = 300-1400 nm). The actual absorbed radiation depends on a number of factors: each day in the solar year sees a different amount of solar radiation reach the Earth; of such amount, only the orthogonal component participates in the energy transfers, and this varies with latitude, longitude and sampling time; local weather can affect the actual amount of energy absorbed, both because of cloud cover and atmospheric refraction (even in clear sky conditions); local topography plays a pivotal role, as neighbouring terrain can either shield the pixel from the direct irradiation (by shadowing) or reflect part of the solar radiation to the pixel itself.

The theoretical radiation R* is in first place determined as the component orthogonal to the Earth surface of the incoming solar radiation:

$$R^* = Ie + D \tag{5}$$

Where *Ie* is the expected radiation intensity obtained by correcting the solar constant *Io* (which is the mean radiation influx throughout the year and amounts to 1353 W/m^2) with the solar elevation angle *h* and the atmospheric attenuation χ:

$$Ie = Io \cdot \sin(h) \cdot \chi \tag{6}$$

$$\sin(h) = \sin(\varphi) \cdot \sin(\delta) + \cos(\varphi) \cdot \cos(\delta) \cdot \cos(\tau) \tag{7}$$

$$\delta = 23.45° \cdot \sin\left[\frac{360}{365} \cdot (284 + DOY)\right] \tag{8}$$

$$\chi = \exp(-\frac{s}{\sin(h)}) \tag{9}$$

$$s = s_o \cdot \frac{P}{P_o} = s_o \cdot \left[\frac{288 - 0.0065 \cdot z}{288}\right]^{5.256} \tag{10}$$

The solar elevation angle *h* is obtained using the latitude ϕ, the hour angle τ (which accounts for time zones and possible summer times) and the declination δ. The atmospheric attenuation χ is an exponential function of the atmospheric optical depth s, itself a function of the atmospheric height z.

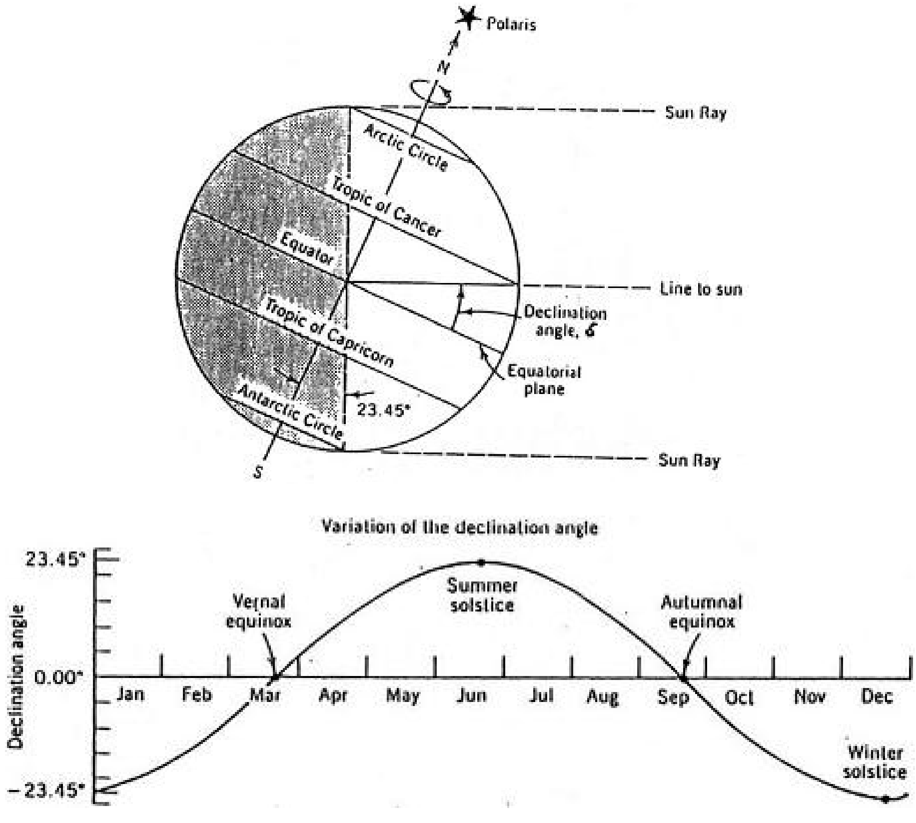

Figure 4 *- The rationale and evolution of the Solar Declination [available at reuk.co.uk]*

D computes the scattering effect of the atmosphere, using a brightness coefficient Kb

$$D = Kb \cdot (Io \cdot \sin(h) - Ie) = Kb \cdot (1 - \chi) \cdot Io \cdot \sin(h) \tag{11}$$

However, actually measured radiation (Rs) can be even lower than the expected amount; this underperformance of the equation can be obtained from past experience as a scaling coefficient Kt. The scattered energy is computed as

$$DF = \min[Rs \cdot D \cdot (1 - Kt); Rs \cdot Kt] \tag{12}$$

So that the direct radiation component is Q=Rs-DF. To account for topographic characteristics, the actual incoming energy Q_A is computed

$$Q_A = Q \cdot \frac{\cos(\mathrm{C})}{\sin(h)} \tag{13}$$

Where C is the angle between the sunbeam direction and the perpendicular to the ground, evaluated as

$$\cos(C) = \cos(h) \cdot \sin(\alpha) \cdot \cos(Az - E) + \sin(h) \cdot \cos(\alpha) \tag{14}$$

Where α is the mountain slope, E the mountain aspect and Az the Solar Azimuth angle.

The last quantity to compute is the radiation reflected from neighbouring terrain A, which is obtained from the slope and the albedo (r) as

$$A = Q_A \cdot r \cdot \alpha / 180\,° \tag{15}$$

The last step in the algorithm requires the computation of the topographical angle ψ, which is the angle, in the Solar Azimuth direction, between the tallest obstacle as seen from the cell in question and the ground. It will simply be

$$\psi = \operatorname{atan}\left[\frac{z_m - z_O}{\sqrt{(x_m - x_O)^2 + (y_m - y_O)^2}}\right] \tag{16}$$

Where (x_O, y_O, z_O) are the three spatial coordinates of the observation point (the cell in question); (x_m, y_m, z_m) indicate the position of the tallest obstacle in the sunbeam's direction (the Solar Azimuth).

All in all, if the pixel is shadowed by some obstacle, only the scattered radiation (DF) will be accounted for; otherwise, also the reflection from neighbouring pixels (A) and the actual incoming radiation R_S will be considered.

$$Rn^{(shortwave)} = (1 - r) \cdot Rs, \;\; Rs = \begin{cases} DF, & if\ \psi \le h \\ Q_A + DF + A, & if\ \psi > h \end{cases} \tag{17}$$

Soil heat flux is due to the fact that, while the topsoil temperature (RET) varies with the sun patterns, the lower part of the ground stays substantially isolated (T_{soil}), creating a temperature gradient within the soil itself. This drives a certain amount of energy either downwards (in summer, when the topsoil is warmer) or upwards (in winter, when it is colder). The rate at which this heat is transferred depends on the soil's thermal conductivity (g_{term}), which is a function of soil moisture; the more air is present within the soil pores (so the less the soil moisture is), the slower the heat is transferred.

$$G = \frac{g_{term}}{dz} \cdot (RET - T_{soil}) \tag{18}$$

The existence of a temperature difference between topsoil (RET) and lower atmosphere (T_A) prompts a certain amount of heat to be transferred in the direction of the existing gradient. This heat transmission is ruled by different factors depending on the presence or absence of canopy. For the vegetated fraction of the basin (f_V) it depends on the aerodynamic resistance of the given canopy ($r_A^{(canopy)}$); for the remaining part, it is regulated by a "bare soil" equivalent of the aerodynamic resistance:

$$H = H_{canopy} + H_{baresoil} = f_V \cdot \frac{\rho_{ha} c_p}{r_A^{(canopy)}} + (1 - f_V) \cdot \frac{\rho_{ha} c_p}{r_A^{(baresoil)}} \tag{19}$$

Where ρ_{ha} is the density of humid air and c_P is its specific heat (the energy to be transferred to change by one degree the temperature of a unit mass).

The latent heat flux is a measure of the heat employed for the direct evaporation of some of the soil moisture. Similarly to the sensible heat, it is expressed by:

$$LE = f \cdot \frac{\rho c}{r_A^{(tot)}} \cdot \frac{\Delta e}{\gamma} \tag{20}$$

Where the "total" aerodynamic resistance is obtained considering both the soil and canopy one. Both depend on the amount of moisture in the ground (θ), as relative to the saturation amount or the (wilting point – field capacity) range.

$$r_A^{(soil)} = 3.5 \cdot \left(\frac{\theta_{sat}}{\theta}\right)^{2.3} + 33.5 \tag{21}$$

$$r_A^{(canopy)} = \frac{r_{S,min}}{LAI} \cdot \frac{FC - WP}{\theta - WP} \tag{22}$$

The Δe is the vapour pressure excess of the saturation value over the actual one, as it constitutes the major driving force of the process.

The Latent Heat is also connected to the Evapotraspiration (ET) element in the water mass balance, through the latent heat of vaporization (λ) and water density ρ_W:

$$LE = \lambda \cdot \rho_W \cdot ET \tag{23}$$

Summing up, most of these processes have a strong link with the water bass balance which constitutes the other half of the governing mechanism of the FEST-EWB model.

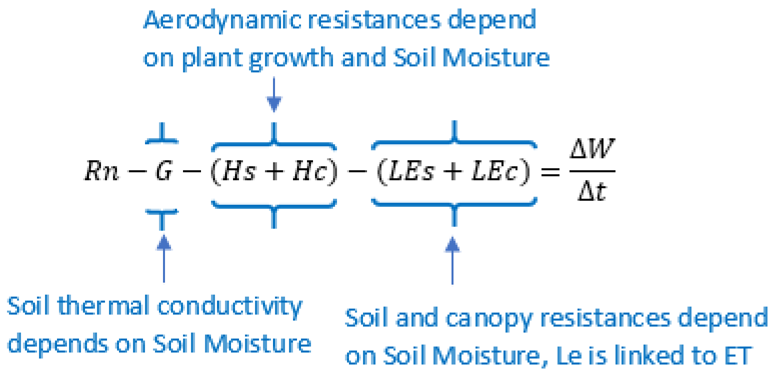

Figure 5 *- The links between the elements of the mass and energy balances*

1.2 Satellite Land Surface Temperature downscaling

The variable chosen for calibration of the FEST-EWB model is the Land Surface Temperature (LST). While discharge calibration requires data from hydrometric stations, temperature can be more easily retrieved using remote sensing (RS) [Corbari et al., 2014] [Corbari-Mancini, 2014]. The quality of data thus obtained, however, can vary significantly. Four main sources will be investigated:

(1) MODIS
(2) LANDSAT
(3) StarFM downscaling algorithm
(4) Kustas downscaling algorithm

1.2.1 MODIS

MODIS (MODerate resolution Imaging Spectroradiometer) is an instrument aboard the satellite Terra. Using its 2330 km swath it provides the most complete image among all the Terra instruments. It can detect 36 bands of the electromagnetic spectrum, between 620 nm and 14385 nm; a wide range of possible applications can be met, from detecting cloud top altitude (bands 33-36) to atmospheric water vapour (17-19). Its orbit around the Earth has it passing from north to south across the equator every morning, thus sampling every place on planet Earth at least once a day. The sampling occurs at around 12:00 am local time, with products at 1000m spatial resolution.

Data from MODIS can be obtained "as-is" or already pre-processed into the required variable. In the LST product, clouded pixels are flagged with a "0" value; thus, a cloud cover mask can be obtained and applied to all the other methods.

The main advantage of such a source is the high temporal frequency. This allows to have a numerous calibration pool even after excluding excessively clouded pixels. However, the relatively "low" spatial resolution of these images can be a problem for basins with areas of important heterogeneity, like mountainous regions, where notable temperature differences occur within less than the 1000m distance of the resolution.

1.2.2 ETM+ (LANDSAT 7)

The LANDSAT program is made up of a network of satellites orbiting around the Earth since July 1972. A number of different satellites have been launched, the most recent being LANDSAT 8 in February 2013. For the purpose of this study, which looks at 2012, data from LANDSAT 7 (launched in April 1999) will be used. LANDSAT 7 has a slower orbit than MODIS, completing a full survey of the Earth in 16 days (against the single one of MODIS).

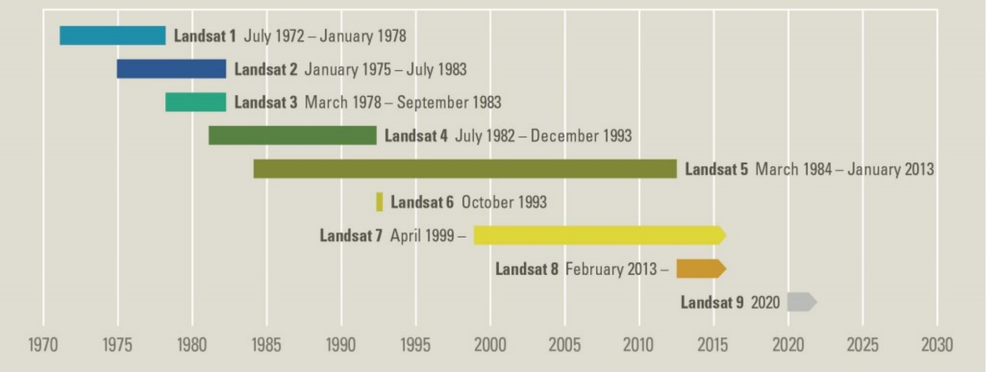

Figure 6 *- The LANDSAT program [https://landsat.usgs.gov/landsat-missions-timeline]*

The instrument aboard LANDSAT 7 is named Enhanced Thematic Mapper Plus (ETM+), and samples within 450 nm and 2350 nm, collecting these data in 8 bands. LANDSAT 7 organizes its images in scenes of 170km (across-path) x 180km (along-path); all the scenes sampled in a day belong to the same "path", which follows the course of the satellite. The paths partially juxtapose with each other, thus having some areas sampled just once every 16 days and other more than once.

The band of interest for LANDSAT is Band 6, the only one sampled at 60m resolution but then re-sampled at 30m. Thus, however more sparse in time, LANDSAT images have better precision than MODIS'.

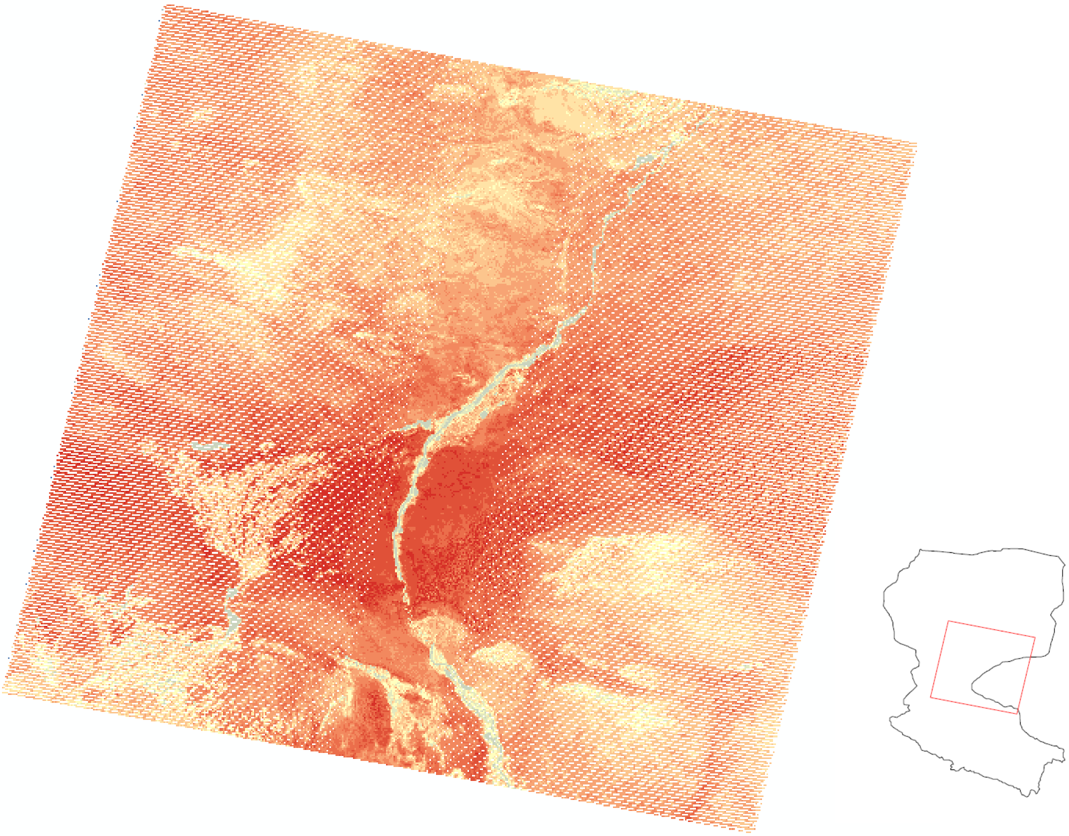

Figure 7 *- An example of LANDSAT 7 ETM+ scene from path 134, row 32 - band 6 (low gain)*

The Scan line corrector (SLC) is a tool of the LANDSAT satellite which compensates for LANDSAT's forward motion. In May 2003 it failed, thus creating problems with the images. The result is a zigzag sampling pattern: some areas have a "double" sampling, while others are not sampled at all. This means that groups of "NoData" cells "pollute" the image, losing an average 10% of 'Data' cells for each image.

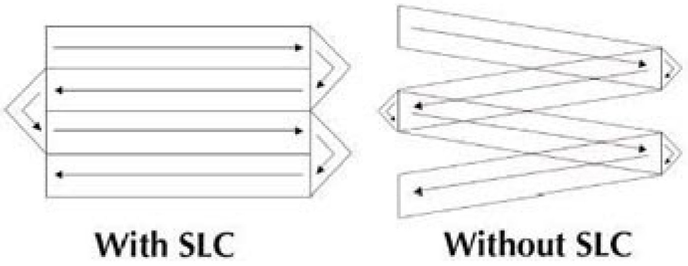

Figure 8 *- The data acquisition with (left) and without (right) the SLC tool*

Data from LANDSAT is organized in paths, that is strings of images that follow, more or less “north-to-south”, the trajectory of the satellite. Each path has a reference number, and partly overlaps with the neighbouring ones; this will be called “across-path juxtaposition”. Within a single path, the satellite divides the total sampled area in scenes, each one part of a numbered “row”. Each of these rows overlaps for a 5% of its length with the preceding and following ones, creating an “along-path juxtaposition”.

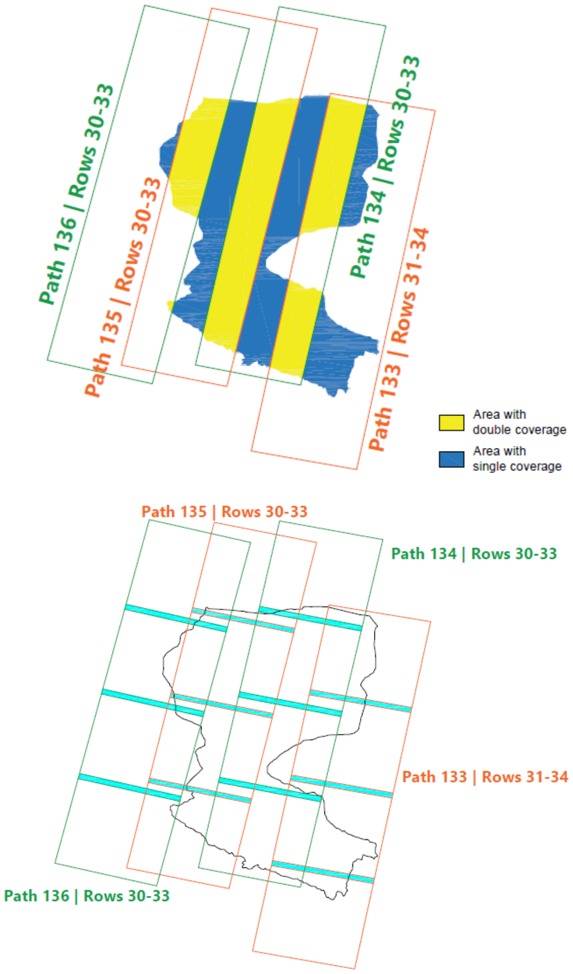

Figure 9 *- Across-path (above) and along-path (below) juxtapositions*

Data from Landsat is not pre-processed as MODIS’ is. The downloadable data consists of radiance values, measured “at-sensor”. The pre-processing, needed to obtain land surface temperature, will thus consist first in a “translation” of the data, so to obtain the “at-ground” version; then a conversion will be required to pass from radiance to temperature.

A simple way to obtain the correction of the radiance values is to apply a Radiative Transfer Model (RTM), that is a relation which “transfers” the data from the sensor to the ground accounting for the atmospheric conditions at the time of sampling [Coll et al, 2010]. As input, RTMs require the transmissivity τ(λ), the upwelling radiative flux (Lu(λ)) and the downwelling one (Ld(λ)). They all depend on the sampling frequency range and on the humidity conditions of the atmosphere. The "at-ground" radiance Lg will be:

$$Lg(\lambda) = \frac{Ls(\lambda) - Lu(\lambda)}{\varepsilon \cdot \tau(\lambda)} - \frac{1-\varepsilon}{\varepsilon} \cdot Ld(\lambda) \qquad (24)$$

Where Ls(λ) is the "at-sensor" radiance measured by LANDSAT. The emissivity ε(λ) can be retrieved from online libraries, such as ASTER's (ASTER is another instrument aboard the Terra satellite). In these libraries, a number of materials are stored, and for every material there is a reflectance (ρ) plot. From the reflectance values, the emissivity is obtained from the simple relation

$$\varepsilon(\lambda) = 1 - \rho(\lambda) \qquad (25)$$

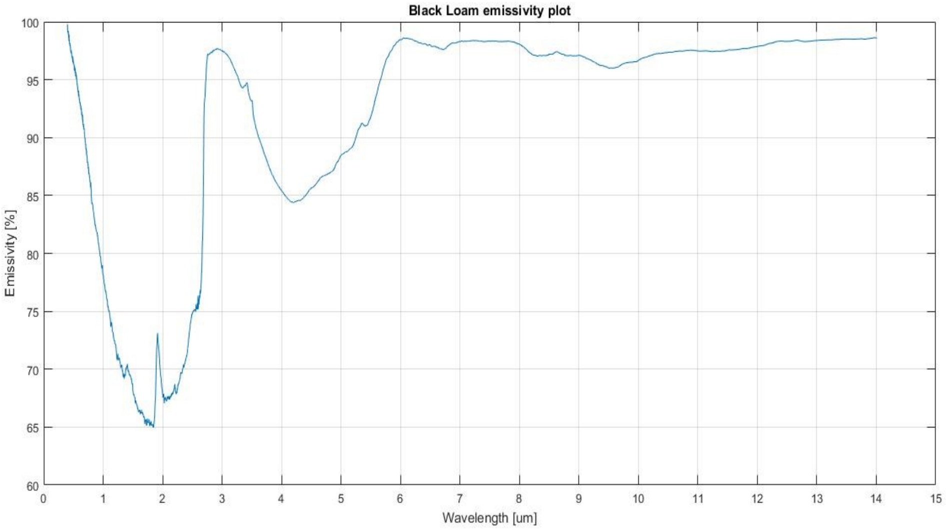

Figure 10 *- Black Loam emissivity plot (data from ASTER spectral library)*

Studying the pixel's land cover, a main material can be associated to each cell in the basin, thus allowing to choose the correct plot. A mean value of emissivity is then computed within the wavelength range of interest.

The other three parameters can be obtained, for a given point on Earth, from a NASA online tool called Atmospheric Correction Parameter Calculator, which computes them starting from climatic models that simulate the weather conditions for the given spot at the sampling time. Such calculation can be performed pixel-by-pixel or the values (Ld(λ), Lu(λ), τ(λ)) can be obtained for a limited number of control points and then inferred back for all the other basin pixels.

Once the corrected radiance is obtained, land surface temperature is given by Planck's Law:

$$Lg(\lambda, T) = \frac{2hc^2}{\lambda^5} \cdot \frac{1}{\exp\left(\frac{hc}{\lambda k_B T}\right) - 1} \rightarrow T(\lambda, W) = \frac{(hc/\lambda k_B)}{\ln\left(\frac{2hc^2}{\lambda^5 Lg} + 1\right)} \tag{26}$$

Where h is Planck's constant (6.626 10^{-34} Js), c is the speed of light (300000 km/s), λ is the reference wavelength (~11 μm), k_B is Boltzmann's constant (1.38 10^{-23} J/K).

LANDSAT's own metafile (used to describe all the data within each path-row combination) shortens up this relation to the form:

$$T = \frac{1282.71}{\ln\left(\frac{666.09}{Lg} + 1\right)} \tag{27}$$

With the result already expressed in Kelvin.

1.2.3 StarFM downscaling algorithm

This method has been developed by Monica Herrero-Huerta, Susana Lagüela, Silvia Alfieri and Massimo Menenti [Herrero-Huerta et al., 2017] at Technische Universiteit Delft.

As MODIS' data is highly frequent but too coarse, while LANDSAT's is sparser and finer, a method has been devised to combine the two with the aim of having each day one 30m-resolution image. Using the illustrated schematics, the algorithm uses LANDSAT radiance data on days 1 and 3 (wavy squares) and MODIS radiance data on days 1, 2, 3 (straight-lined squares) to obtain a synthetic, "LANDSAT-like" image on day 2. The algorithm is here explained in its simpler form, when using just data from days 1 and 2 to obtain the target image on day 2. Each equation can be extended to include data from day 3.

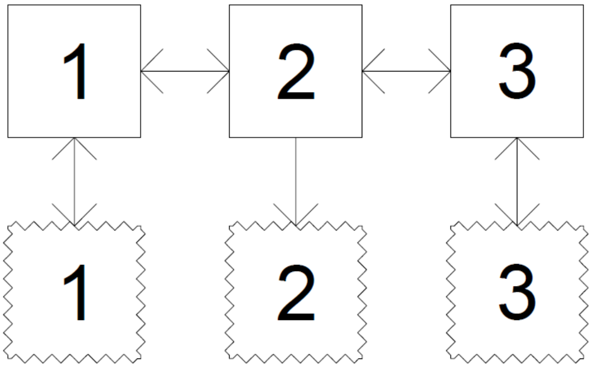

Figure 11 *- StarFM operational scheme (straight lines stand for MODIS data, wavy ones for LANDSAT)*

Neglecting geolocation errors and divergencies in atmospheric correction, the other differences between LANDSAT and MODIS (caused by slightly different retrieval times, and thus solar geometry, or different bandwidth) can be collected in the epsilon parameter in:

$$L(x_i, y_j, t_k) = M(x_i, y_j, t_k) + \varepsilon_k \tag{28}$$

where L is the LANDSAT radiance value, M the MODIS one and each $(x_i,y_j)_{i,j}$ identifies a single pixel at LANDSAT's resolution, to which MODIS' data is resampled. Assuming the error ε_k to be constant with time k, for any (0,k) time instants the relation is

$$L(x_i, y_j, t_0) = M(x_i, y_j, t_0) + L(x_i, y_j, t_k) - M(x_i, y_j, t_k) \tag{29}$$

Using this relation, each pixel's L value can be found at time t_0, provided that the M values at times t_0 and t_k and the L value at time t_k are known. However, this relation neglects the possibility that one single MODIS pixel could include different land cover types which are instead found at LANDSAT's resolution. Furthermore, time variations of emissivity (because of changing canopy, for example) and solar radiation (because of different sunbeam geometries along the year) should be properly accounted for.

These uncertainties are dealt with introducing more data from neighbouring pixels, choosing among spectrally similar ones. Around each pixel, a searching window of amplitude w is built, and the final computed value will be

$$L(x_{w/2}, y_{w/2}, t_0) = \sum_{i=1}^{w}\sum_{j=1}^{w}\sum_{k=1}^{n} W_{ijk} \cdot [M(x_i, y_j, t_0) + L(x_i, y_j, t_k) - M(x_i, y_j, t_k)] \tag{30}$$

Where to each neighbouring pixel within the searching window is assigned a weight W_{ijk}, depending on three factors:

(a) Spectral difference between MODIS and LANDSAT data for the same time (S_{ijk})
(b) Time variation of MODIS values between t_0 and any given t_k (T_{ijk})
(c) Distance of the "neighbouring" pixel from the interest one (D_{ijk})

Using a correcting coefficient B, these parameters are gathered as

$$C_{ijk} = \ln(S_{ijk} \cdot B + 1) \cdot \ln(T_{ijk} \cdot B + 1) \cdot D_{ijk} \tag{31}$$

$$W_{ijk} = \frac{1/C_{ijk}}{\sum_{i=1}^{w}\sum_{j=1}^{w}\sum_{k=1}^{n}(1/C_{ijk})} \tag{32}$$

Theoretically, the algorithm can be as complete as described above or simpler, without considering neighbouring pixels and/or without weighing properly each contribution to the final result. Such an algorithm would undoubtedly be quicker in elaborating the final image. However, [Gao et al, 2006] have proven that both "expansions" of the algorithm are quite important.

They have used synthetic images, defined by a main dimension called "Object Radius" (OR). The target image was produced for an increasing Object Radius in three different ways: without any spatial information; including neighbouring pixels in the analysis, but without any particular weight W_{ijk}; with the complete algorithm.

Mapping the evolution of the relative error of the prediction, spatial information initially was found to cause more problems than benefits: for Object Radiuses lower than ~300m, the relative error when using neighbouring pixels was higher than when looking just at the single pixel (~30% more for OR=90m, then decreasing). Furthermore, no actual difference was found between weighting or not the surrounding pixels.

After the 300m mark, using neighbouring pixels with weighting meant that the error collapsed almost to 0%; without weighting, the error was 10%-30% more; without spatial contributions, it could be even 60% more, around 480m.

This explicates the limits of the model: relatively little objects (like some crop fields, or some steep and narrow mountain valleys) can be misrepresented by the model, but the accuracy grows with the nominal dimension of the target object.

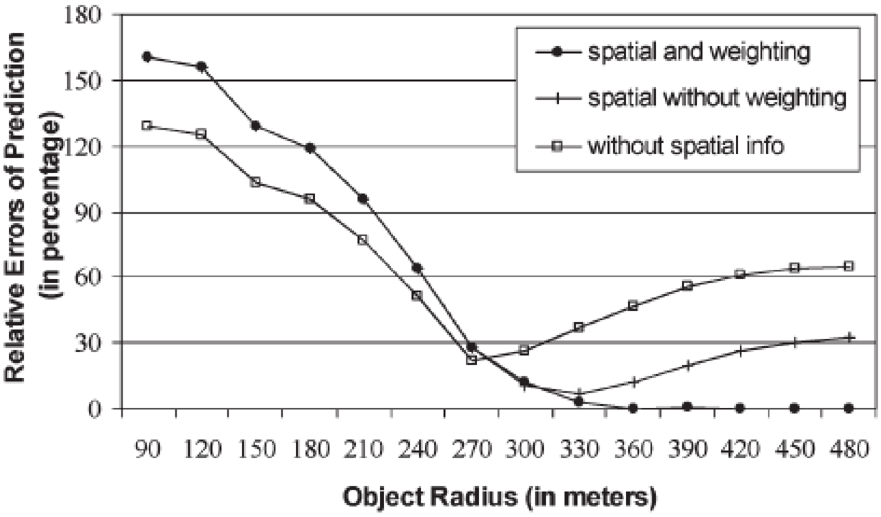

Figure 12 *- Different error patterns for different StarFM configurations, from [Gao et al, 2006]*

Furthermore, the method was originally [Herrero-Huerta et al, 2017] employed using LANDSAT 8 images (which do not suffer of the SLC failure, and so show better quality than LANDSAT 7), further refining the image to a 10m resolution raster using the land cover data coming from Sentinel 2 MSI data.

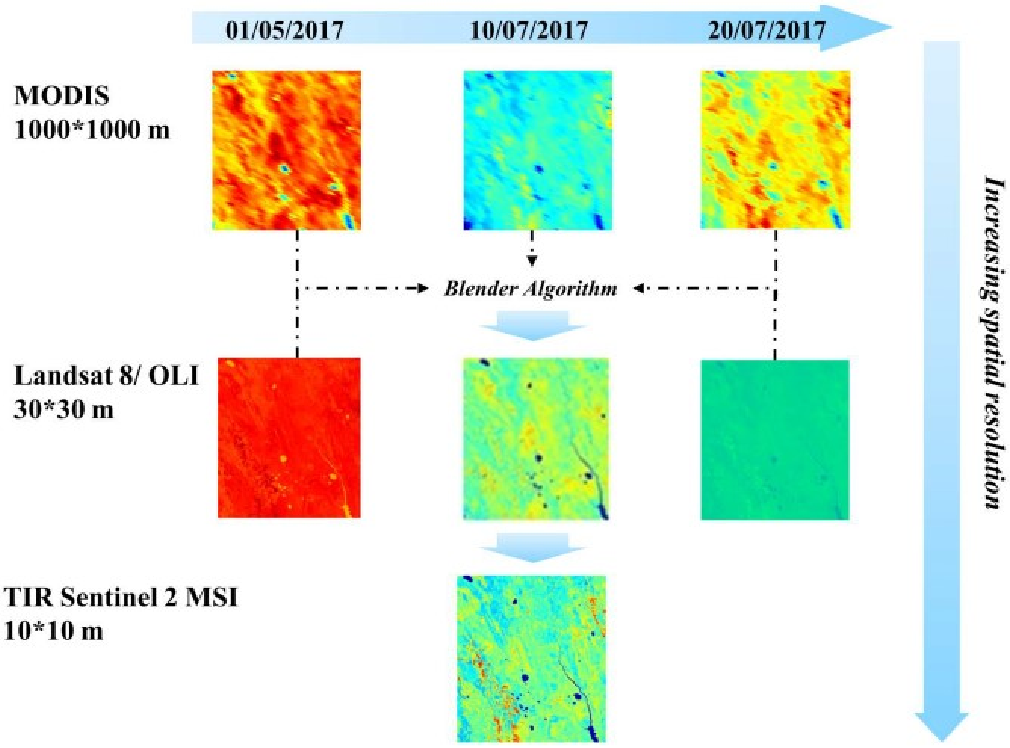

Figure 13 *- Operational scheme employed for [Herrero-Huerta et al, 2017]*

1.2.4 Kustas downscaling algorithm

Another method used to retrieve LST involves a very common index, the Normalized Difference Vegetation Index (NDVI), and has been developed by [Kustas et al, 2003].

The reason for its involvement is that it is often available at finer pixel resolution than LST and for its simple implementation; the aim of the method is to establish a univocal relation between NDVI and LST, in order to apply it to the easily-retrieved NDVI fine-resolution data to obtain an LST equivalent.

$$NDVI = \frac{NIR - red}{NIR + red} \tag{33}$$

The NDVI is the difference between the NIR light reflected by the leaves' cells (the higher the more leaves there are) and the red visible light reflected by the chlorophyll in the plants' cells (the lower the "greener" the vegetation is); this difference is then weighted on the total amount of available energy, so that the index conveniently varies within the range

-1 to +1. This definition means that the more developed the canopy is (the more red light is absorbed and NIR is reflected), the higher the NDVI index. Usually, values of NDVI<0.2 mean an almost bare soil, while values >0.5 correspond to a full canopy cover.

Assuming that an LST image at low resolution is available (LST_{LOW}), together with an NDVI image at higher resolution ($NDVI_{HIGH}$), the aim will be to identify the coefficients of a least-squares fit between the needed LST_{HIGH} and $NDVI_{HIGH}$, using a parabolic equation.

The first step requires to resample the high-resolution NDVI image to LST's low resolution, obtaining $NDVI_{LOW}$. For each pixel (i,j), a couple $NDVI_{LOW}(i,j)$ – $LST_{LOW}(i,j)$ will exist, allowing for a parabolic fitting of the type

$$\widehat{LST}_{LOW}(i,j) = a + b \cdot NDVI_{LOW}(i,j) + c \cdot NDVI^2_{LOW}(i,j) \tag{34}$$

The accuracy of this fitting can be measured with indexes like R^2 and RMSE/σ.

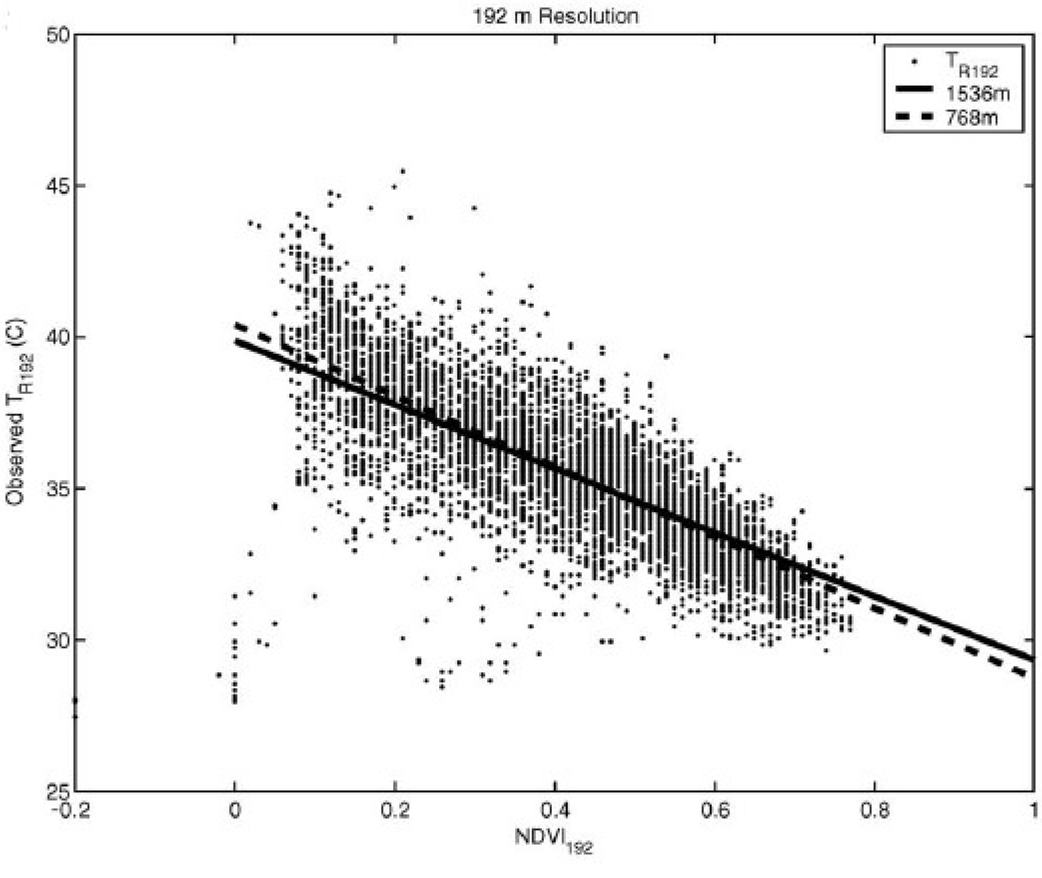

Figure 14 *- An interpolation example from Kustas et al, 2003*

As a second step, in order to account for space variability (especially because of soil moisture effects), an estimation error will be taken into account

$$\Delta LST_{LOW}(i,j) = LST_{LOW}(i,j) - \widehat{LST}_{LOW}(i,j) \tag{35}$$

Finally, after re-sampling ΔLST_{LOW} to ΔLST_{HIGH}, the final value for each pixel is obtained as

$$\widehat{LST}_{HIGH}(i,j) = a + b \cdot NDVI_{HIGH}(i,j) + c \cdot NDVI_{HIGH}^{2}(i,j) + \Delta LST_{HIGH}(i,j) \qquad (36)$$

[Kustas et al, 2003] have applied the method with interesting results, obtaining accurate fittings.

Their results have shown a good performance for target objects with main dimension comparable with MODIS' resolution (around 1000m). For higher-resolution images, the method has been compared with a simple re-sampling of the coarser image to the desired resolution. The algorithm has not shown any improvement to this method, in particular reaching its worst performance for target resolutions between 200m and 400m.

1.2.5 General comparison

Source	**MODIS**	**LANDSAT 7 ETM+**	**StarFM algorithm**	**Kustas algorithm**
Input Images	1 image	5 images	5 images (3 MODIS + 2 ETM+)	2 images (NIR, red at fine res. + LST at coarse res.)
Input Image type	Temperature	Radiance	Radiance	Radiance Temperature
Pre-processing parameters	Scale factor	ε(λ) Ld(λ) τ(λ) Lu(λ)	ε(λ) Ld(λ) τ(λ) Lu(λ)	ε(λ) Ld(λ) τ(λ) Lu(λ) Scale factor
Availability	Everyday	Once every 16 days	Everyday	Everyday
Spatial resolution	Visibile 500m Thermal 1000m	30m	30m	Same as NIR and red data

Table 1 *- Characteristics comparison between the LST sources*

Chapter 2

Case Study: Heihe River

In this chapter, Section 1 will deal with a general historical and political overview of the basin. Section 2 provides information on the geomorphology of the basin, while Section 3 focuses on the pedologic characteristics of the basin. Section 4 describes some satellite-retrieved data about vegetation, while Section 5 relates the land cover use of the terrain. The climatic an meteorological patterns of the basin are, finally, delved into in the last section, Section 6.

2.1 Overview

The Heihe River Basin is the second largest inland basin in China. "Hei He" literally means "Black River" (黑 河), as a reference to the dark black loam it transports. Along its route, it has been given other names, like "Ruo Shui" ("Weak Water", 弱 水), stemming from the low discharge in its lower reaches.

The river originates in the northern ranges of the Qilian mountains, running in south-east direction and collecting water from minor streams, on both banks. After about 200 km in the narrow valleys of the mountain range, the river turns north towards the valley beyond the mountains (the "Hexi Corridor"), creating a number of oases.

Past the city of Zhangye, the river turns north-west before describing a wide 90° turn along which more tributaries reach it from the south. 175 km after the turn, the river splits in two distributaries, the "eastern" (Dong He) and the "western" (Xi He) rivers. Each branch runs on another 220 km before emptying in two twin lakes which constitute the Ejina Basin: the Sago Nuur (East Juyan Lake) and the Gaxun Nuur (West Juyan Lake), respectively [Yin et al, 2015] [Liu et al, 2013] [Cui et al, 2016].

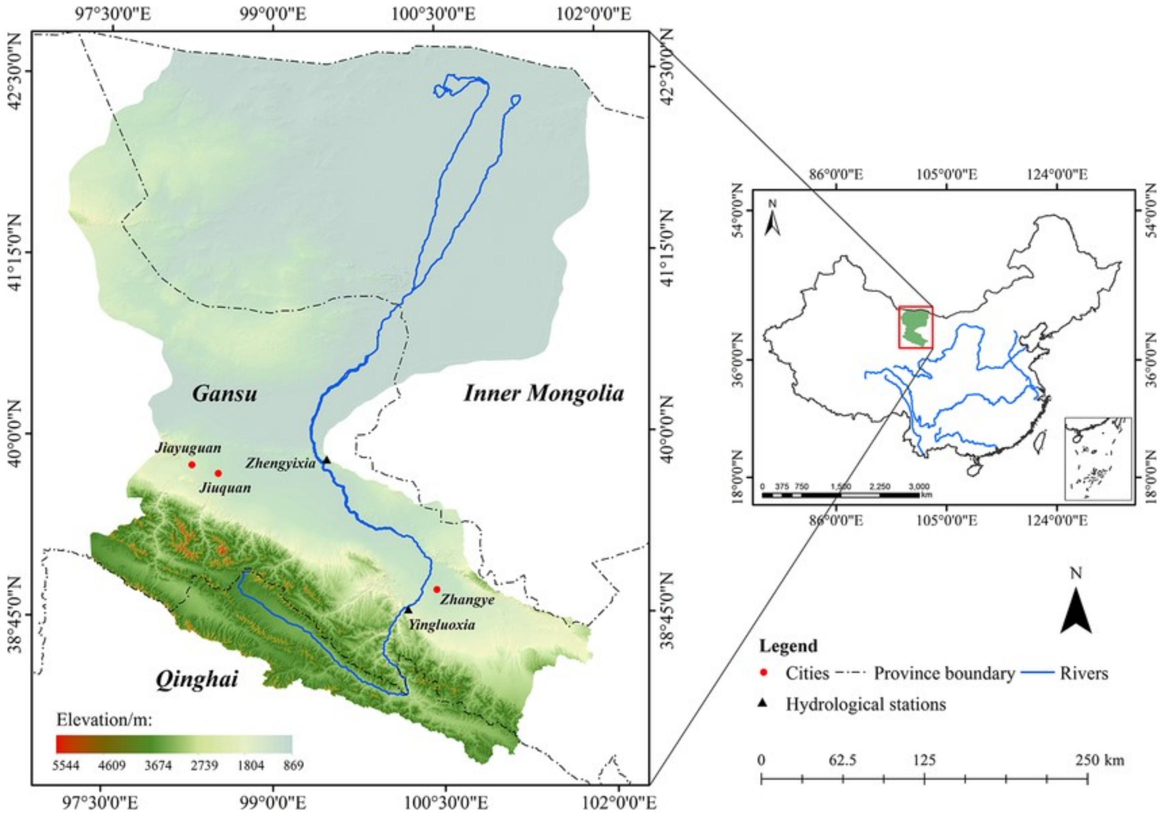

Figure 15 *- Heihe River basin from [Cui et al, 2016]*

These last reaches of the river are ephemeral, as the combination of evaporation and percolation weakens the river flow, often drying up the lakes and shortening the parallel branches. In this last part of its route, the river flows in the alluvial fan it has created during the years; this fan, characteristic of inland river deltas, constitutes the westernmost part of the Gobi Desert. The Heihe River basin occupies ~152000 km^2 with elevations ranging from the 5544m of the mountains to the 869m of the terminal lakes.

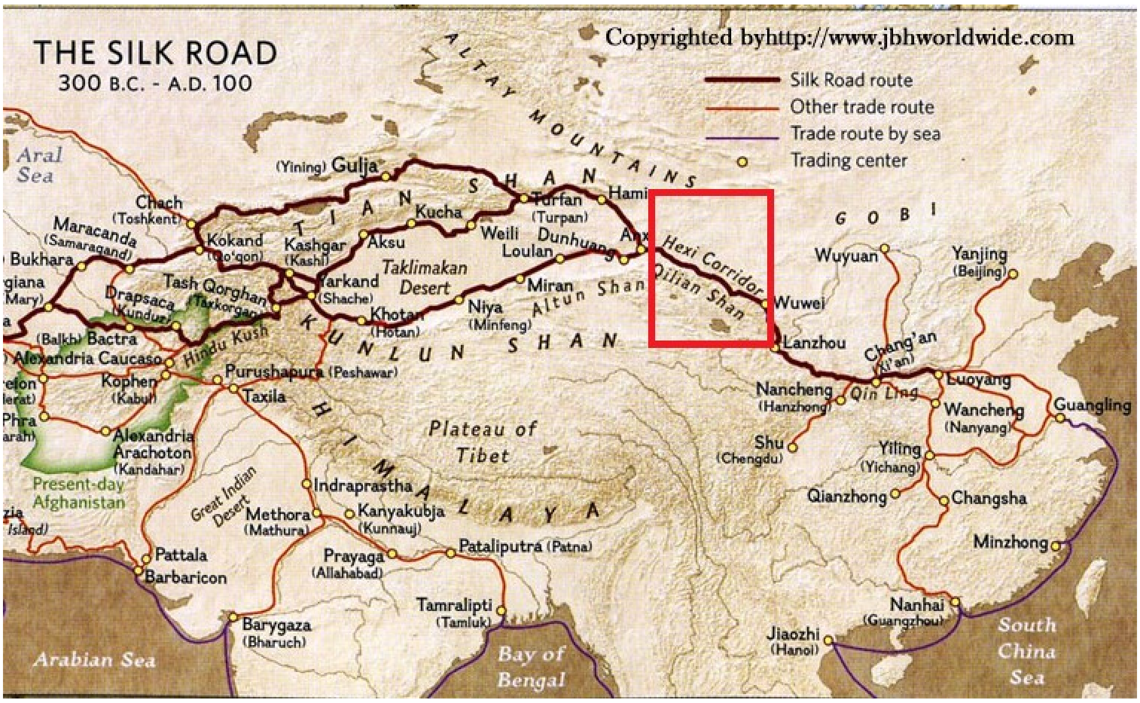

Figure 16 - *Ancient Silk Road and location of the Heihe River basin (in red), from chinadiscovery.com*

The river has the utmost historical importance, as it straddles the Hexi Corridor: this is a narrow strip of land, squished between the Gobi and Mongolian deserts to the north and north-east and the Qilian mountains to the south. As these latter represent the northernmost border of the Tibetan plateau, the corridor constitutes one of the few viable ways for land connections between Europe and the Far East. The three main sections of the Western Silk Road all come together to pass the corridor, before branching out again. The strategic position has led the oases along the way to grow into prosperous cities, like Zhangye. This prosperity brought on new population, whose needs were met with activities like logging and cultivation, this last one sustained by an extensive network of irrigation canals [Li et al, 2018]. Over the years, this has created a desertification danger in the area: the river has reached less and less into the desert (traces of old irrigation canals have been found in the Ejina oasis area, [Hu et al, 2017]), its riparian vegetation has massively decreased, the water table has shrunk in the ground and the topsoil has seen a growing salinization [Wang et al, 2015].

Water stress (the deficit of the water resource availability with respect to its demand) is a foremost problem in China. The combination of climate change effects (more frequent droughts and floods) and population growth have led to a critical situation.

Figure 17 *- Water stress evolution in China, from the World Resources Institute*

The Heihe River basin being amongst the most endangered areas, it has been included in a wide governmental campaign of reforestation and re-allocation of the water resource. In the specific case of the Heihe River basin, this new policy set out to better distribute the water resource between the middle and lower reaches; one of the measures was to always save 0.95 billion m^3 of water for the flow in the lower stream when the annual runoff at the entrance of the middle reaches surpasses 1.58 billion m^3 [Huang, 2015].

This ecological water diversion project (EWDP) has been implemented in 2000, and has since registered encouraging but still partial results [Shi et al, 2014] [Xin et al, 2018], as the map above shows. Studies such as this are what is needed to develop the knowledge of this basin and the mechanics of its water cycle.

2.2 Geomorphology of the basin

The basin can be split in three main regions: the upper reaches cover the mountainous ground, from the river source down to the Yingluoxia hydrometric station; the middle reaches occupy the narrow valley between the mountains and the desert and are the most urbanized and the most agriculturally exploited; the lower reaches span the alluvial fan of the river and have an arid environment dotted with isolated oases.

Section	Area [km^2]		Population [in.]		Density [in./km^2]
High reaches	27’376	17.94%	3’169’747	10.19%	116
Middle reaches	25’391	16.64%	23’869’741	76.77%	940
Low reaches	99’839	65.42%	4’053’878	13.04%	41

Table 2 *- General subdivision of the Heihe River basin (data about population from SEDAC Columbia)*

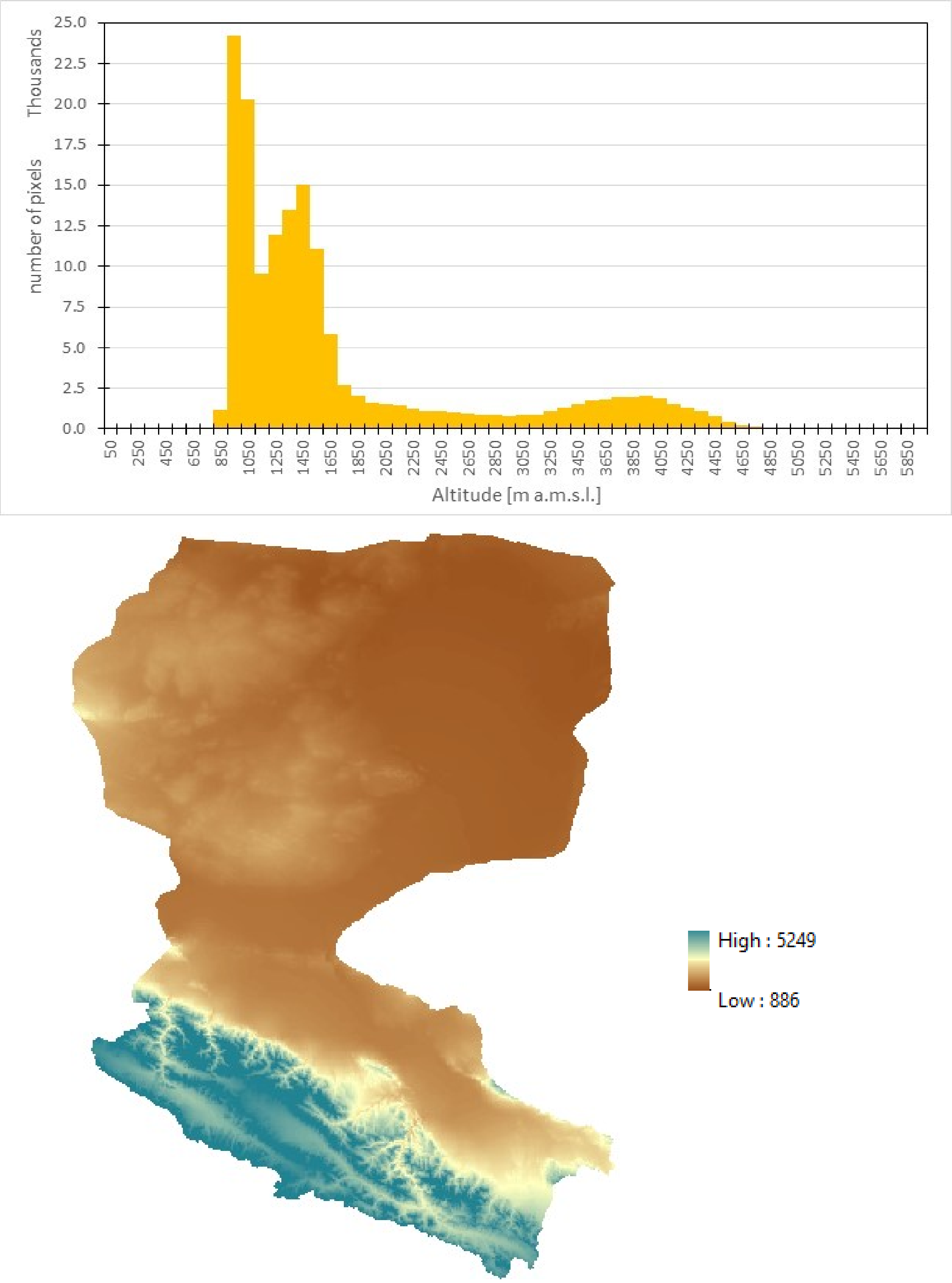

Figure 18 *- Altitude histogram and Digital Elevation Model*

A list of basin parameters will be featured in the pages to follow.

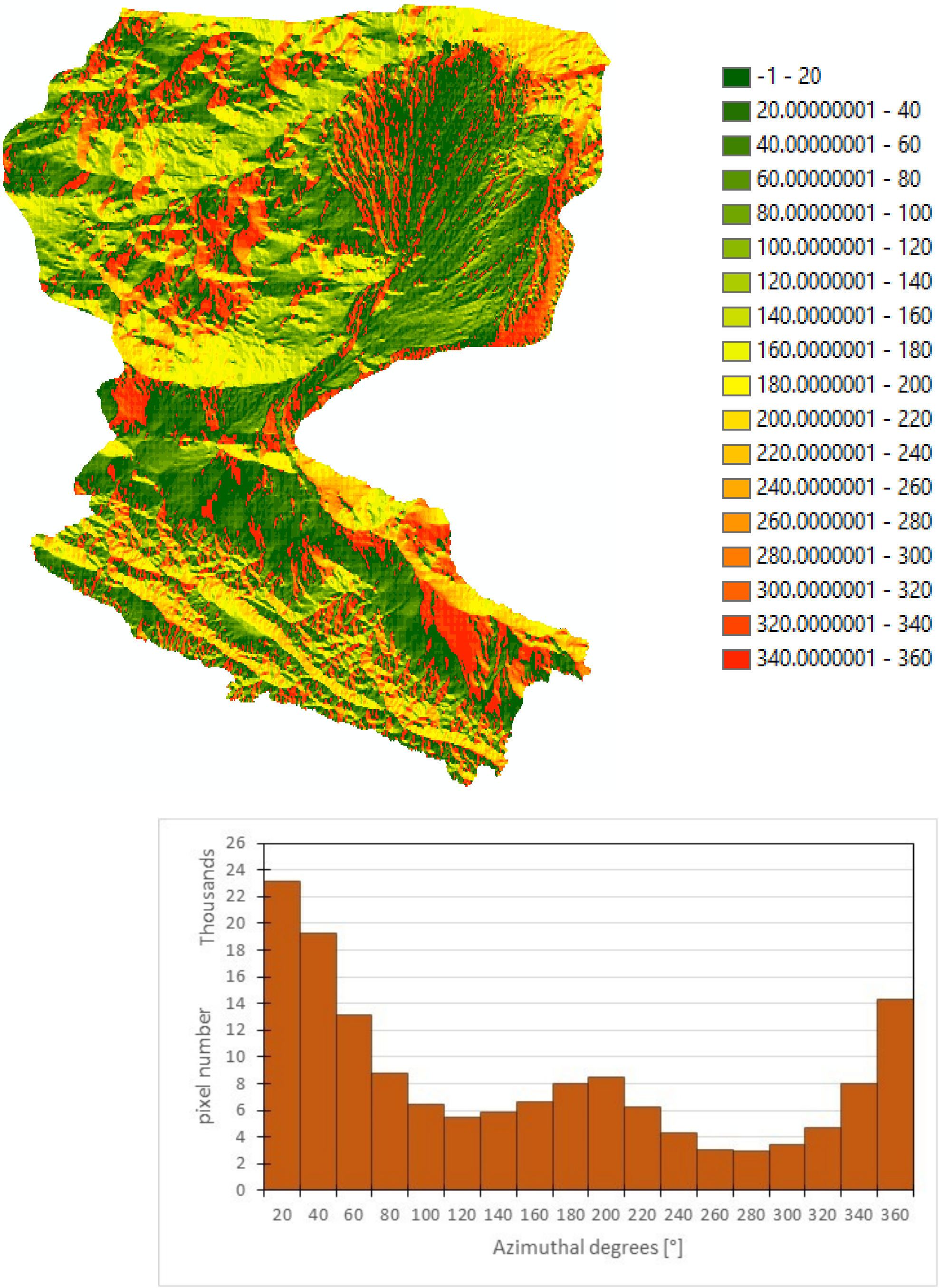

Figure 19 *- Aspect map and histogram(legend in Azimuthal degrees [°])*

The aspect is the exposition (here expressed in azimuthal degrees from the north) of each pixel. It is fundamentally important for the solar exposition, and is widely employed in FEST's algorithm. The mountain range in the southern part of the basin has widely varying aspects, while the valley immediately downriver has mainly northward aspects, where the terrain slopes toward the river. The same holds for the main alluvial fan, where the mainly northward direction of the river is reflected in how its solid load is deposited.

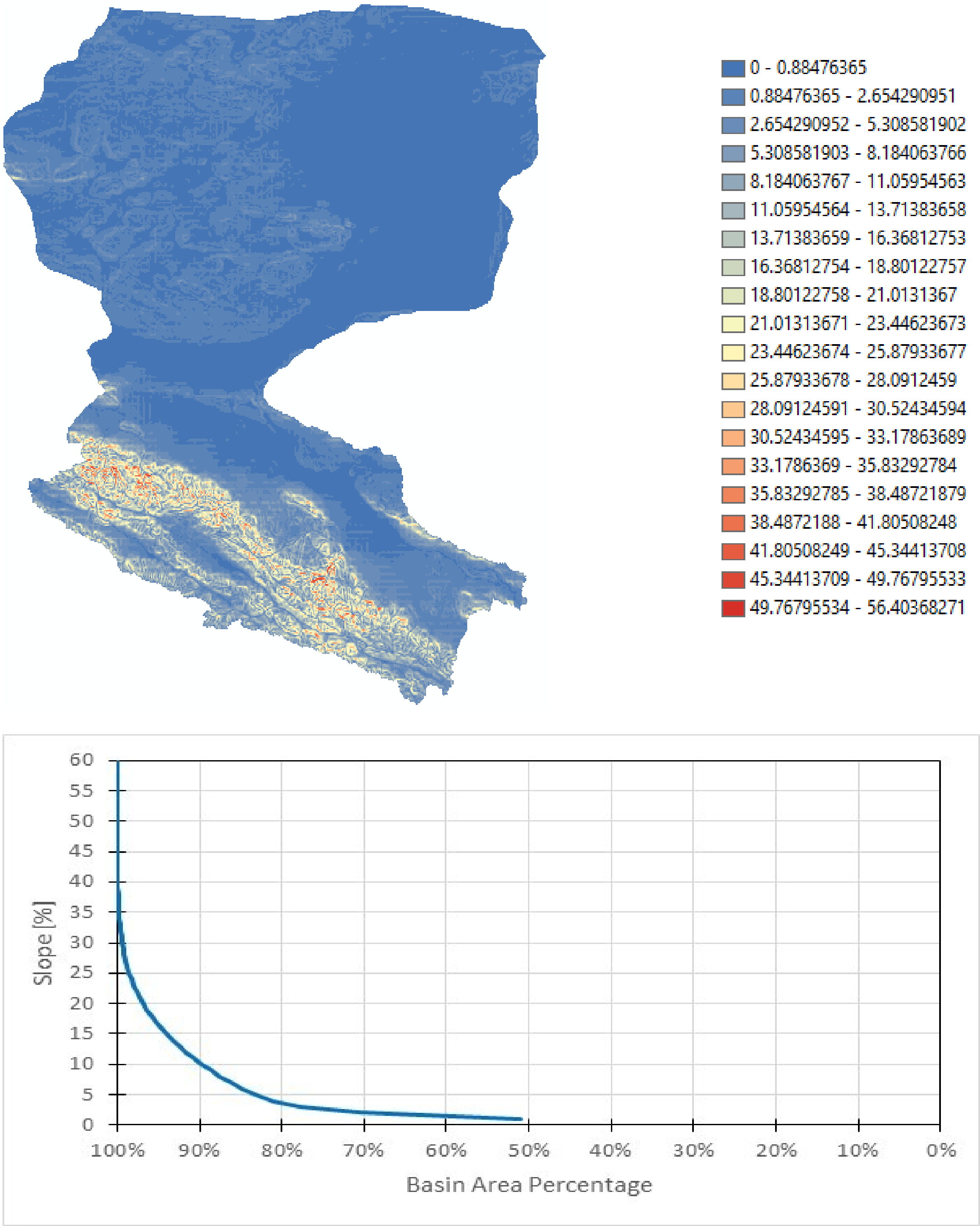

Figure 20 *- Slope map and frequency curve (legend in Percentage [%])*

Most of the region is quite plain, with most of the basin below 10% (circa 90% of the total area); the mountainous area can be quite steep, with peaks of 56%.

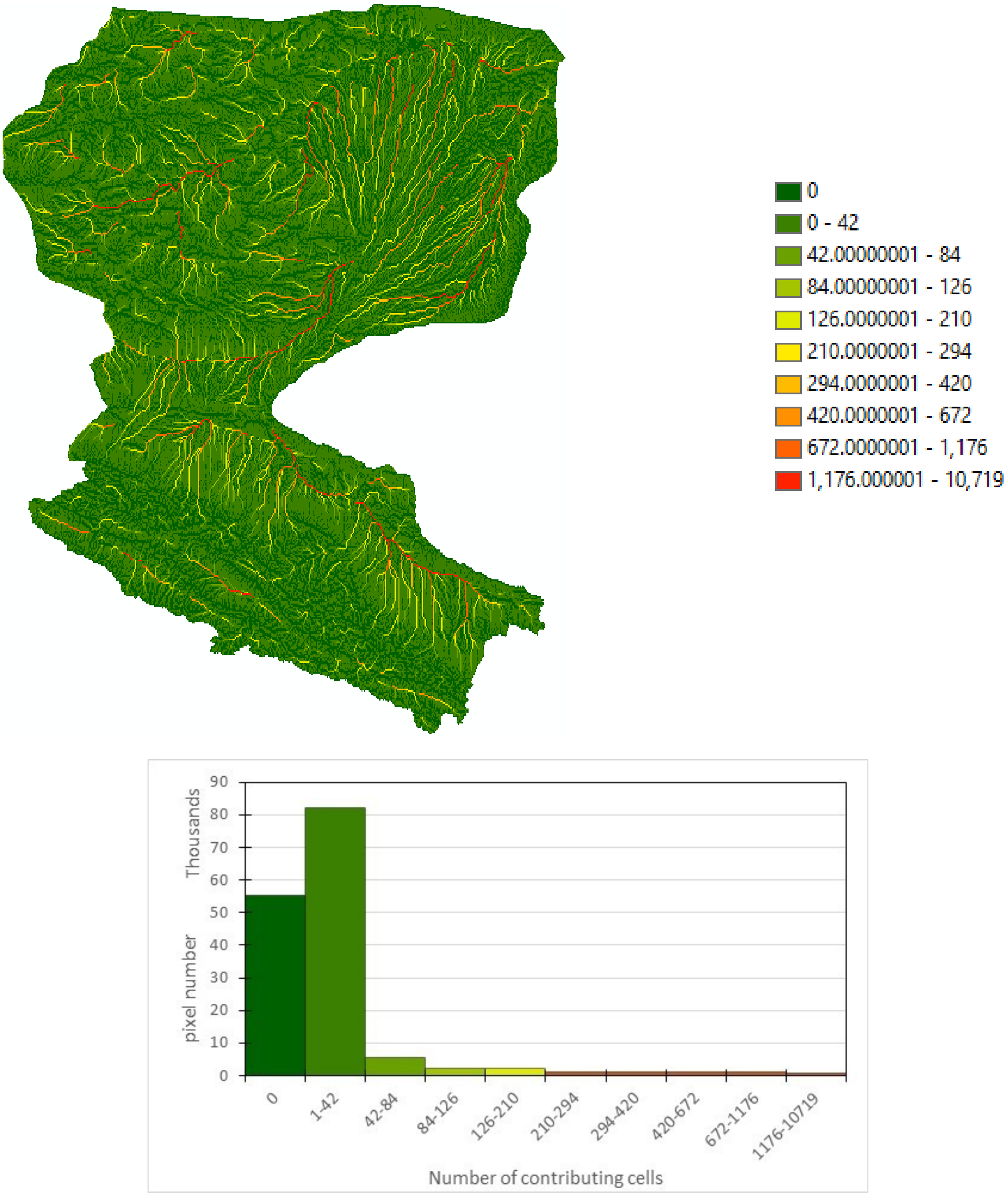

Figure 21 *- Flow Accumulation map and histogram (legend in nr. of contributing cells)*

This plot indicates, for each cell, the number of other cells whose output flows through the cell in question. With the "0" tag are labelled all the cells which constitute the "ridges" part of the basin, according to the FEST-EWB. This means that they are not part of the hydrological network proper, which is the main runoff conveyer of the basin. The flow accumulation plot is used by the FEST-EWB model to simplify the computation of the hydrological network, reducing it only to the cells labelled as "conveyer" ones.

2.3 Pedology of the basin

The pedology of the basin is a complex matter, as no detailed geological map of the area is available. Instead, numerous indexes have been mapped, such as the wilting point, the field capacity, the saturated hydraulic conductivity or the saturated water content.

From these, an ex-post soil classification can be obtained: crossing the available data, to each pixel is assigned a probability that the pixel in question belongs to a certain soil category. The pedologic class with the highest probability for each pixel is the one assigned to the cell itself. The analysis yields the following table.

Soil class	N° of pixels	Relative area
Loamy Sand	18682	12.24%
Loam	128810	84.41%
Silt Loam	4142	2.71%
Sandy Clay Loam	262	0.17%
Silty Clay Loam	424	0.28%
Silty Clay	286	0.19%

Table 3 *- Soil classes found in the basin and their incidence*

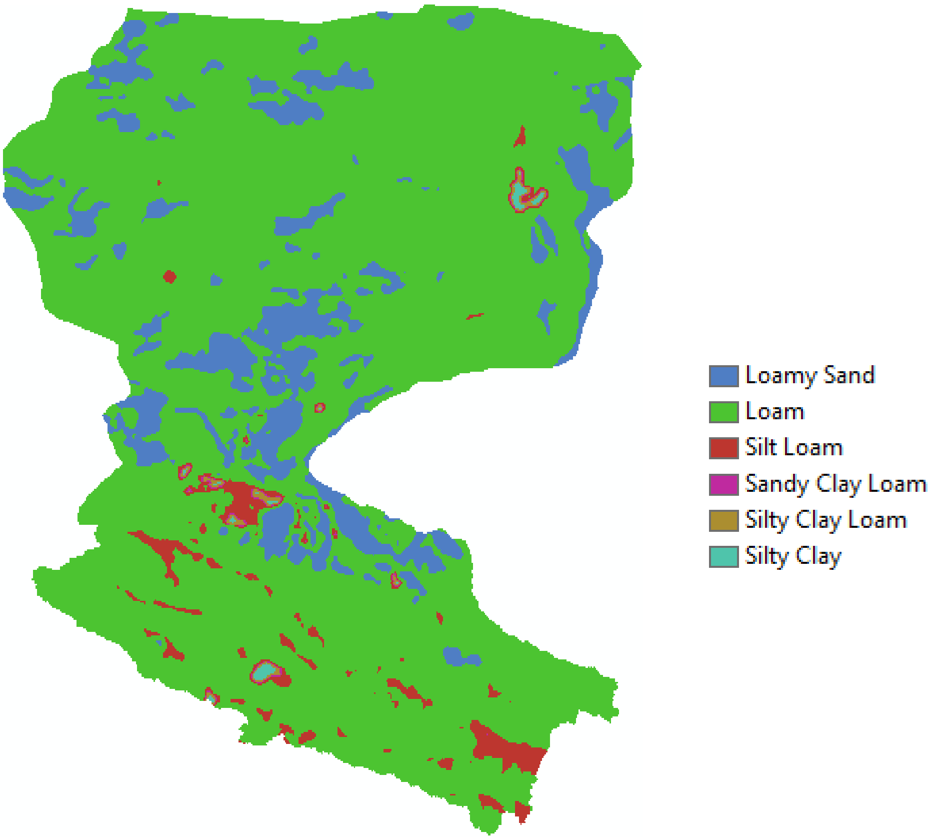

Figure 22 *- Soil texture classes found in the Heihe River basin*

The most diffused soil class in the basin is "Loam". This word frames a soil composed mostly of sand (particle size bigger than 63 µm) and silt (> 2 µm), with a little amount of clay (< 2 µm). By weight, the composition is about 40-40-20%, respectively. The other classes detected represent slight variations on that standard proportions. Generally, any soil where no clear predominance of one of the three categories is present is labelled as "loam". This soil composition usually holds more nutrients than sandy soils and guarantees better infiltration than silty soils. This mix is quite favourable to cultivation, thus being partly "responsible" for the agricultural "boom" in the region.

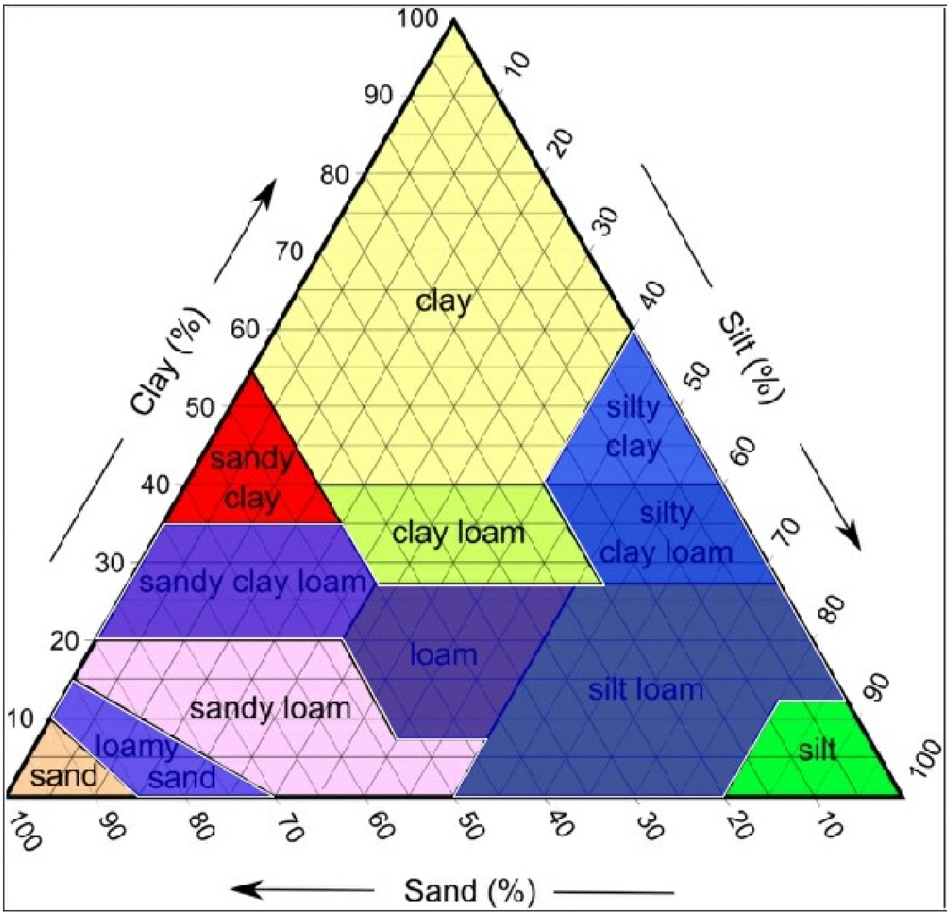

Figure 23 *- A soil mixtures classification scheme provided by the Handbook of Hydrology. Shadowed in blue, the categories found in the Heihe River basin*

The properties of such soil mixtures are displayed in the table below. For each parameter, an average value is given for any single category.

Soil class	Conductivity at saturation	Brooks-Corey index	Wilting Point	Field Capacity	Bubbling pressure	Residual water content
	K_{SAT} [μm/s]	**λ [-]**	**WP [-]**	**FC [-]**	**h_B [cm]**	**θ_R [-]**
Loamy Sand	13.889	0.553	5.50%	12.5%	8.69	3.5%
Loam	4.1667	0.252	11.7%	27.0%	11.15	2.7%
Silt Loam	1.3889	0.234	13.3%	33.0%	20.76	1.5%
Sandy Clay Loam	0.9722	0.319	14.8%	25.5%	28.08	6.8%
Silty Clay Loam	0.4167	0.177	20.8%	36.6%	32.56	4.0%
Silty Clay	0.2778	0.150	25.0%	38.7%	34.19	5.6%

Table 4 *- Average values of hydraulic parameters of certain soil mixtures, from the Handbook of Hydrology*

The table shows the different behaviour of the soil mixtures according to the relative ratio of its components. Loamy Sand, for example, is the mixture with the most sand, with clay and silt both below 15% and 30%, respectively, at their best. Such a soil offers less resistance to the transit of water, hence the highest soil conductivity (at saturation) of the basin; the high Brooks-Corey Index (which indicates a more homogeneous pore-size distribution than the other categories) and the relatively low WP and FC all agree with this assumption.

On the contrary, the last three categories show a more consistent presence of silt. The result is a wider variety of pore sizes, and an increased ability to withhold water (as testified by higher WP and FC), typical characteristic of silty soils. However, these pores have little communication with the outside of the soil matrix (hence the low conductivity); their small dimension (on average) means that the capillary forces which hold the water are higher, making it more difficult for plants to extract water (hence the higher FC and, more importantly, WP).

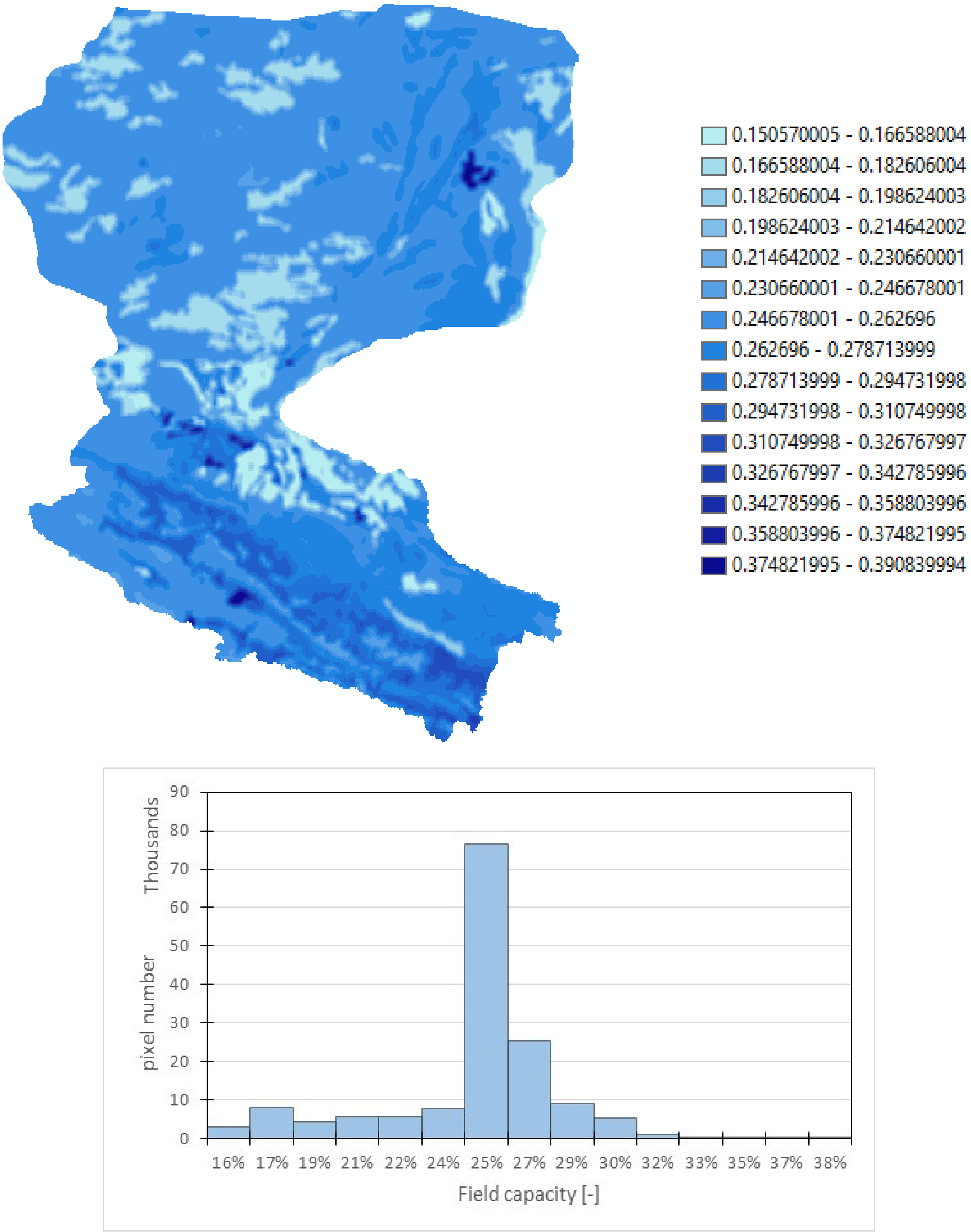

Figure 24 *- Field capacity map and histogram (legend in volume percentage [-])*

Field capacity (FC) is the maximum amount of moisture that the soil can withhold after any downward infiltration or superficial runoff has concluded. It depends mainly on the soil texture and composition, and thus can vary according to the way the river has deposited its sediment load over the years. Its strict definition is the amount of water retained by a 33 kPa suction.

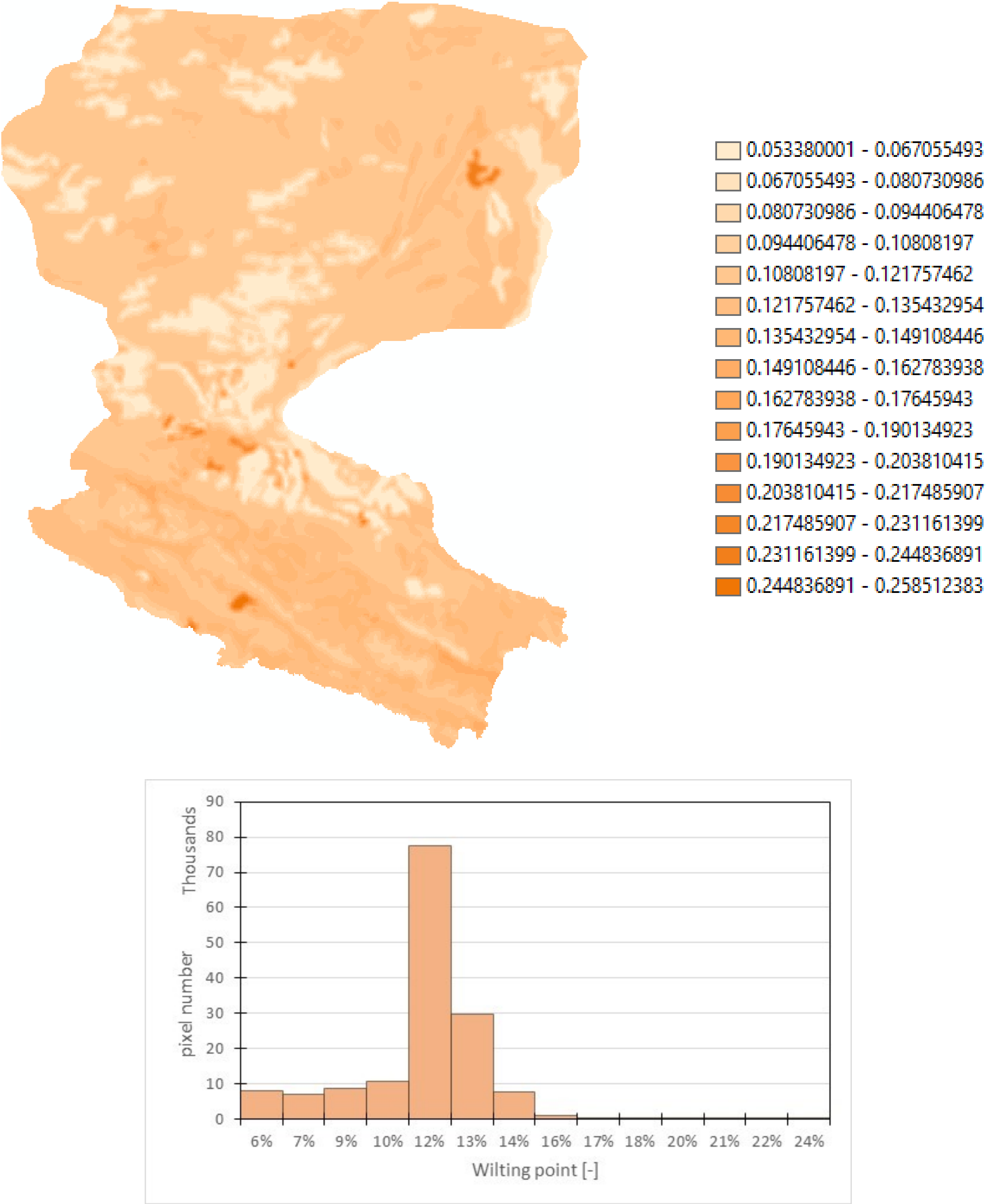

Figure 25 *- Wilting point map and histogram (legend in volume percentage [-])*

The wilting point (WP) parameter, as a sort of "counterpart" to the field capacity above, expresses the least amount of water in the soil capable of sustaining vegetation. Beneath this value, the only water left in the soil is so strongly held by the capillary forces between the soil particles, that the suction needed to extract it surpasses the maximum force that plants can apply. This suction limit is conventionally set to -1500 kPa, but depends on the cultivations and the radical apparatuses of the plants.

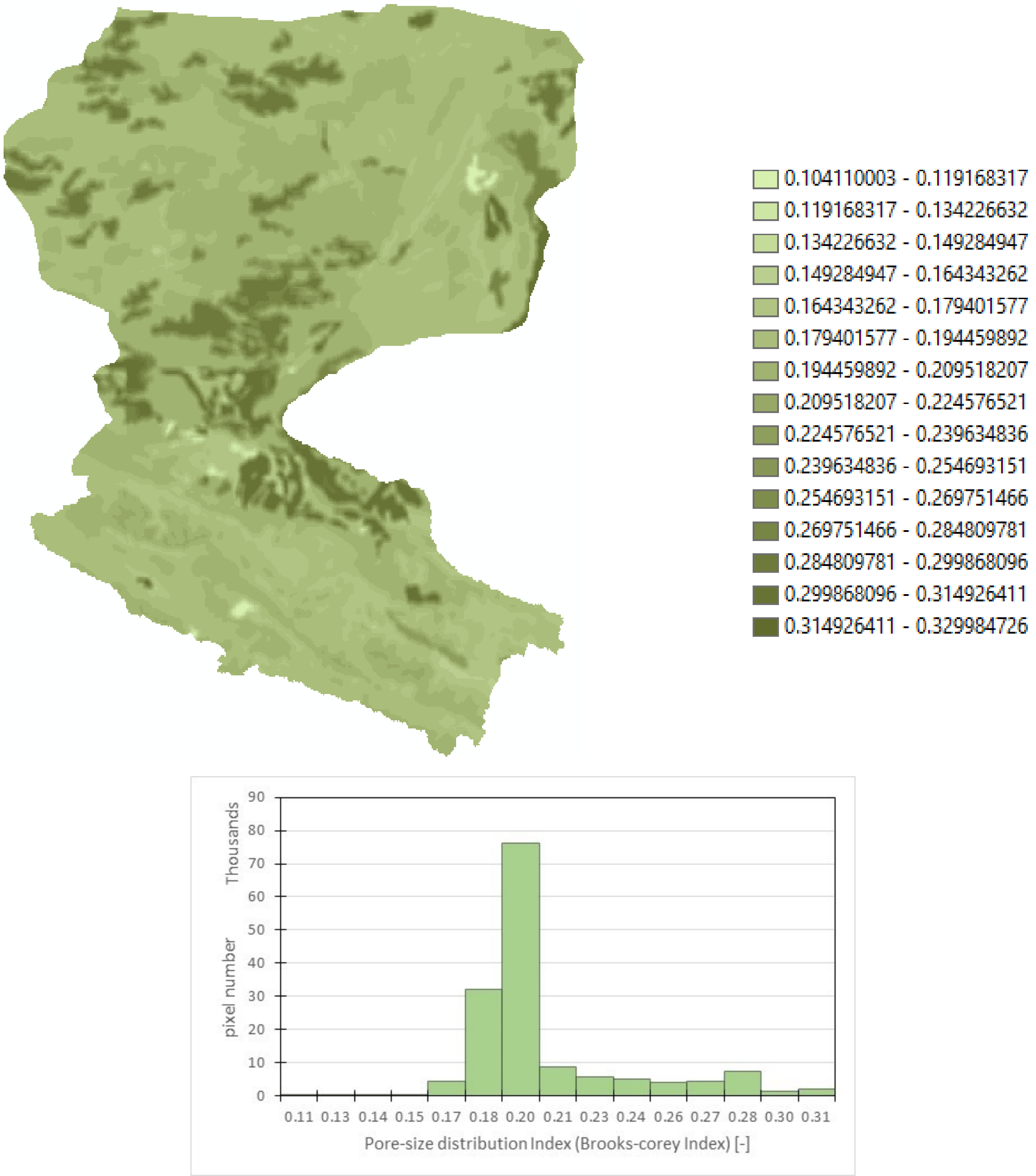

Figure 26 *- Pore-size distribution Index map and histogram (legend non-dimensional [-])*

The pore-size distribution index is an empirical parameter connected to the in-soil voids: the more homogeneous the pores, the lower the index. It is directly linked to the other hydraulic parameters, as more uniform pores favour deep percolation [Assouline, 2005]. It derives from a theory developed from Brooks and Corey, with the Bubbling Pressure (P_b):

$$S_e = \left(\frac{P_b}{P_c}\right)^{\lambda} \tag{37}$$

Where P_c is the capillary pressure (the pressure at the interface between two fluid phases coexisting in the soil) and S_e is the effective saturation, which corresponds to the actual saturation as relative to the residual saturation [Brooks-Corey, 1964].

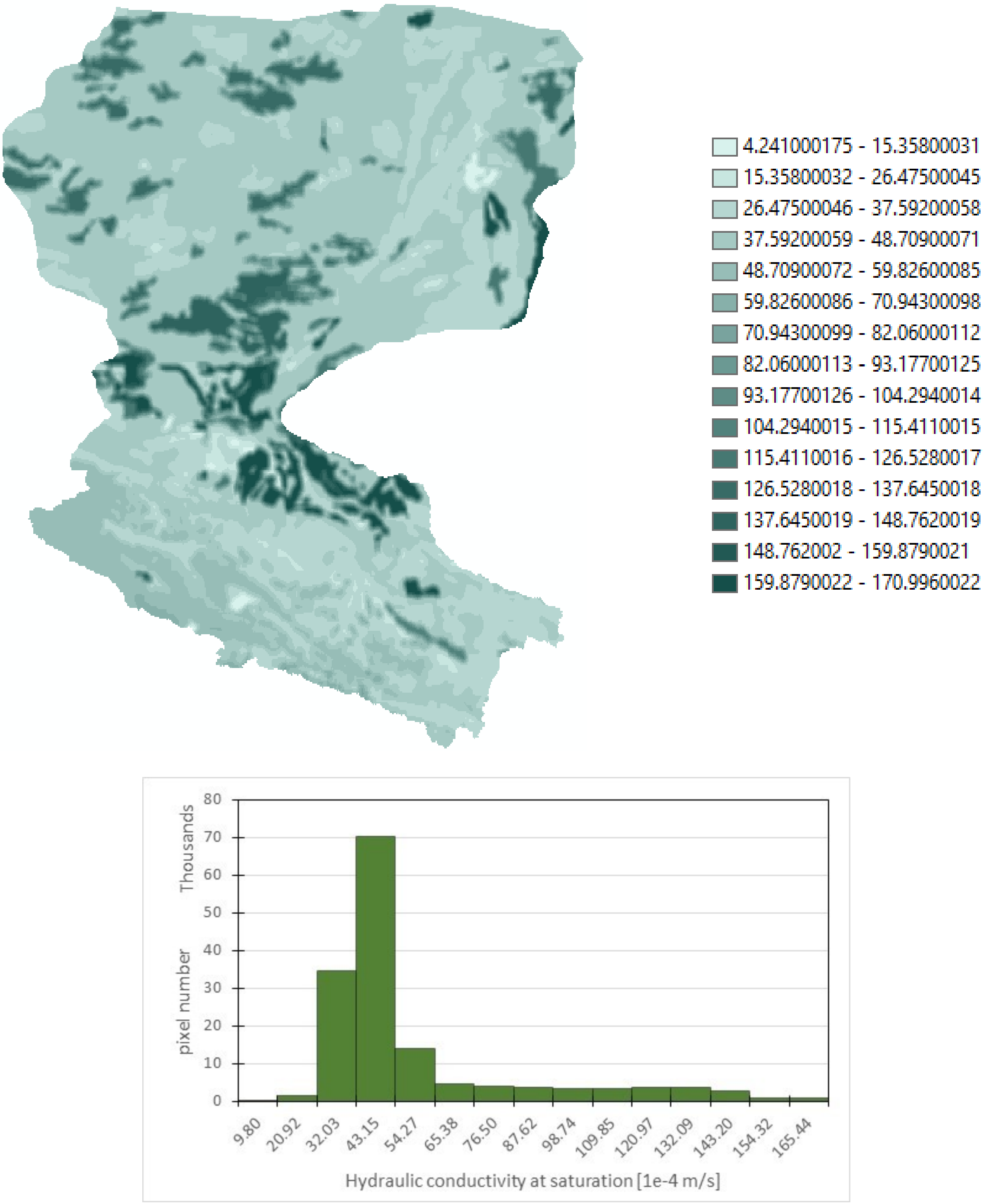

Figure 27 *- Hydraulic conductivity at saturation map and histogram (legend in [0.1 mm/s])*

The hydraulic conductivity parameter is linked to the soil's ability to convey water. It has its highest value in the saturation condition, and has lower values for intermediate soil moistures, following a power function of the SM/SM_{SAT} ratio.

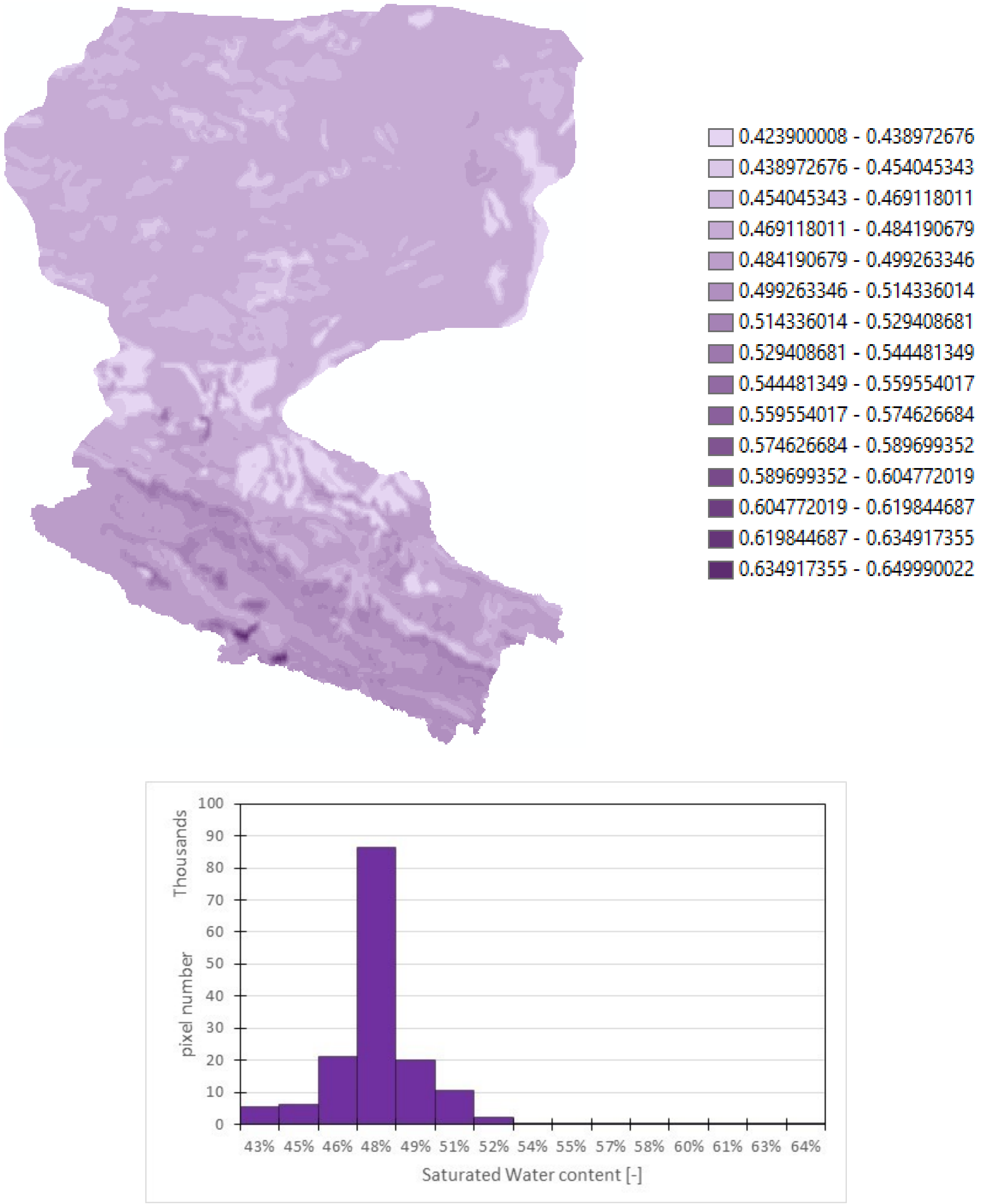

Figure 28 *- Saturated water content map and histogram (legend in volume percentage, [-])*

Saturated Water content is the maximum amount of moisture that the soil can store, expressed in volume of water per unit volume of soil. As is evident, it surpasses the field capacity because it accounts also for the water stored during rain or irrigation, which is lost by infiltration or superficial runoff in a short period of time (a couple of days at best). Looking at the unit volume of soil as a water tank, this parameter represents the maximum volume of water before the excess is expelled, mainly by superficial runoff or ponding.

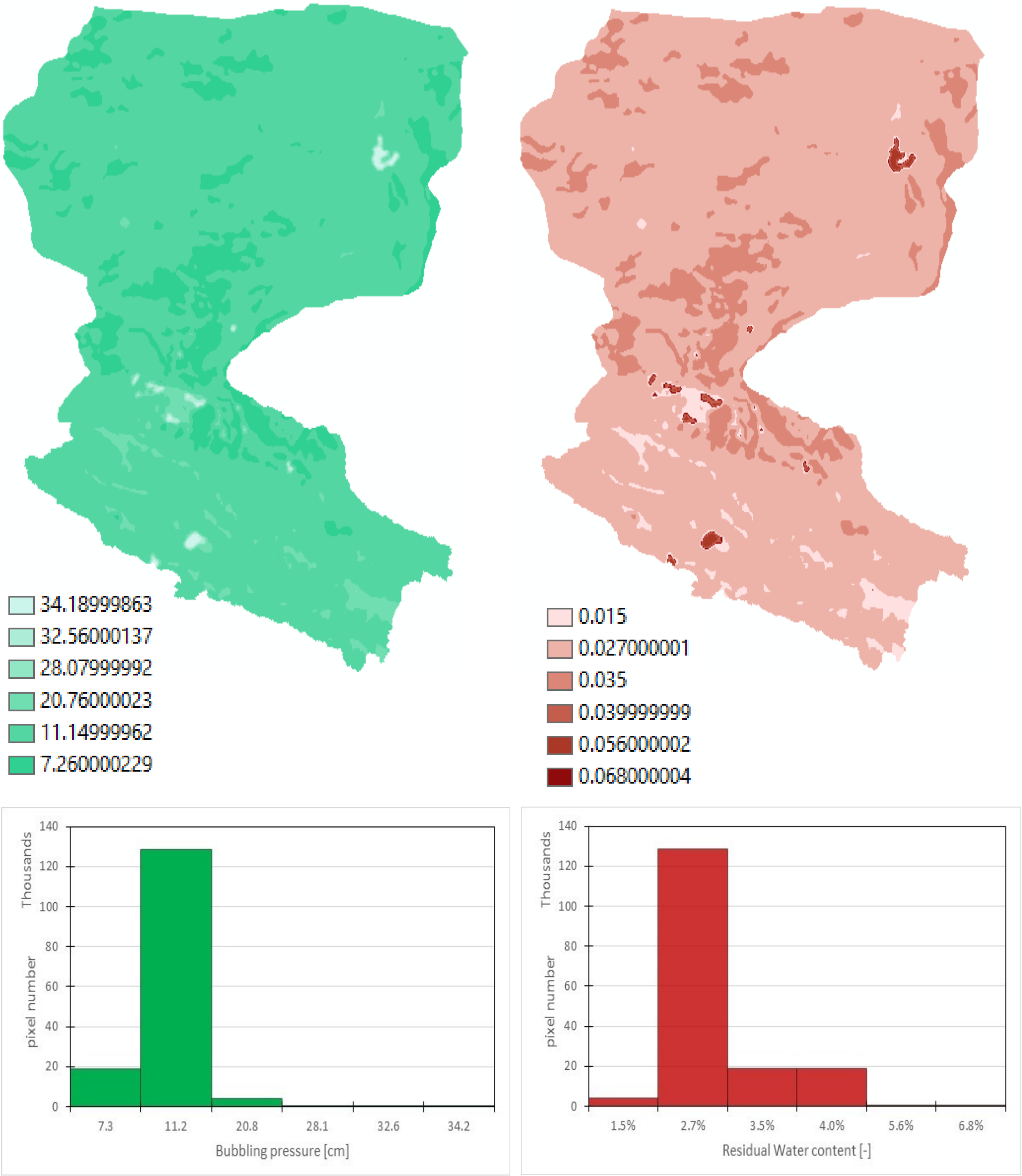

Figure 29 *- Bubbling pressure (left) and Residual water content (right) map and histogram (legends in [cm] and [-], respectively)*

These indexes have been obtained indirectly from available data, and this explains the little value range with respect to the parameters seen above. The bubbling pressure is part of Brooks-Corey model, and has the physical meaning of being the pressure value at which, for homogeneous and isotropic media, the first gas flow (hence, "bubbling") is observed. The residual water content has a similarly empirical meaning of being the water content retained for high suction. By "high", it is meant that only the forces present in the micropores are able to withhold this amount of water, and no mechanical action can extract it.

2.4 MODIS satellite data

The three plots in this section are obtained from MODIS. In fat, a number of different parameters are found within its produts. In particular, both albedo and LAI are present with higher resolution than MODIS' LST data (500 m instead of 1000 m). Furthermore, LAI data is sampled once every 4 days, and has been interpolated for the purpose of having values every day. All data can be found at the National Aeronautics and Space Administration website (www.ladsweb.modaps.eosdis.nasa.gov/).

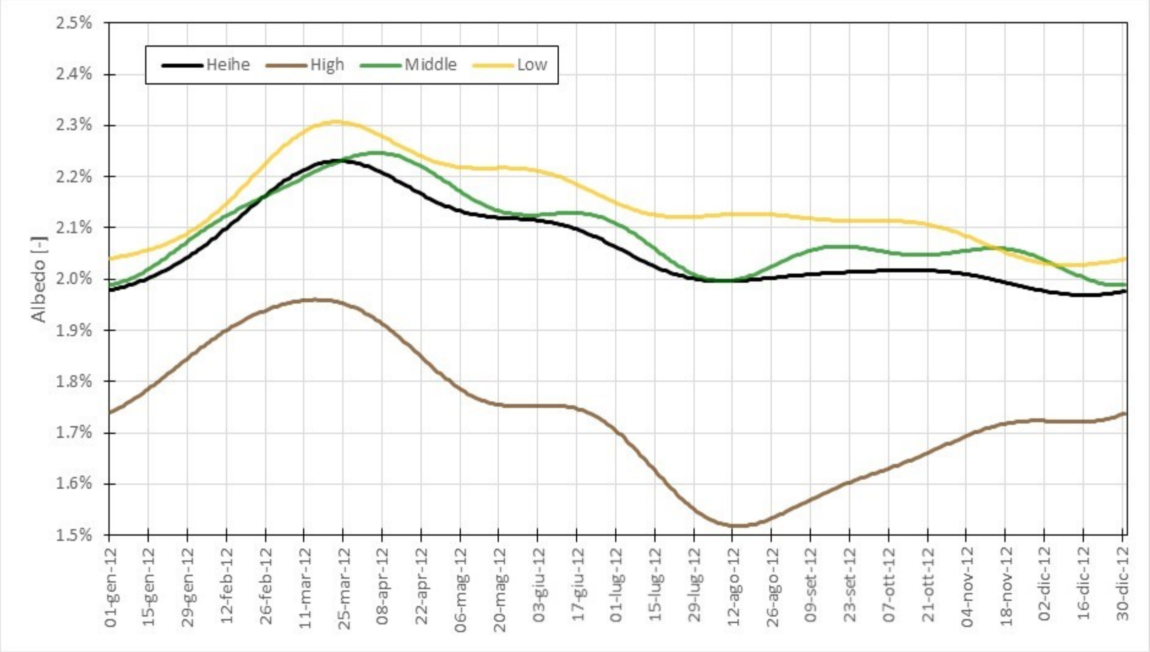

Figure 30 *- Albedo patterns for the whole basin (Heihe) and its sub-regions*

The albedo is the amount of energy (expressed as fraction of the total incoming one) which is reflected back from the given terrain pixel. This amount can change widely according to land cover types and can evolve through the year along with "coloration changes" of the pixel: snow cover can reflect more solar radiation (thus with a higher albedo), as plant withering can absorb more thermal infrared radiation, lowering the albedo.

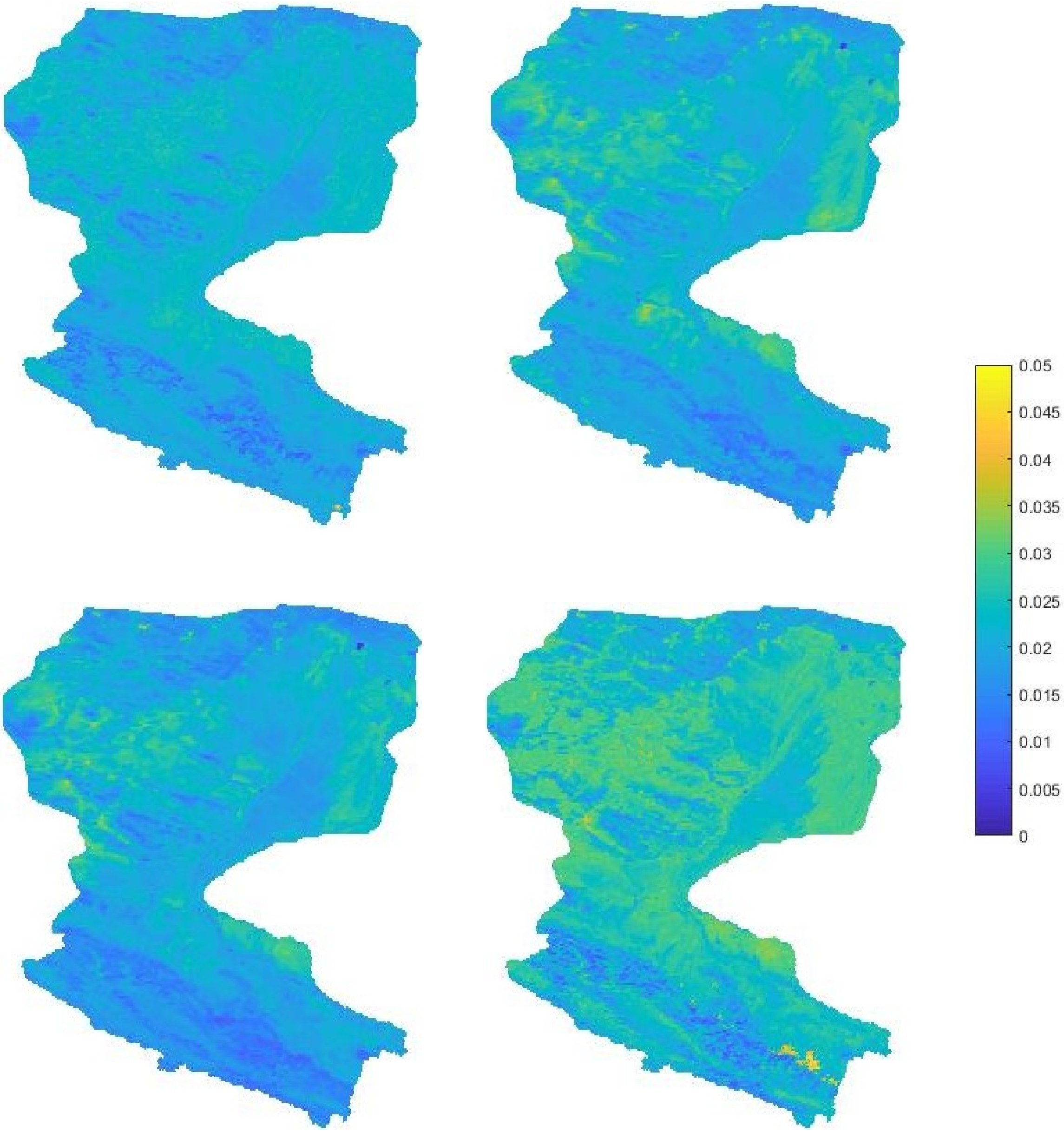

Figure 31 *- Average albedo value for winter (first row, left), spring (first row, right), summer (second row, left) and autumn (second row, right)*

As an example, these maps show the albedo average value for each season. The different growing patterns of the various kinds of vegetations could explain the higher albedo in the desert area for autumn. The mountain range, on other hand, shows similar values all year long.

This because albedo values depend on a lot of factors, ranging from snow cover to the vegetation’s growth stage, to the presence of irrigation systems and paved roads.

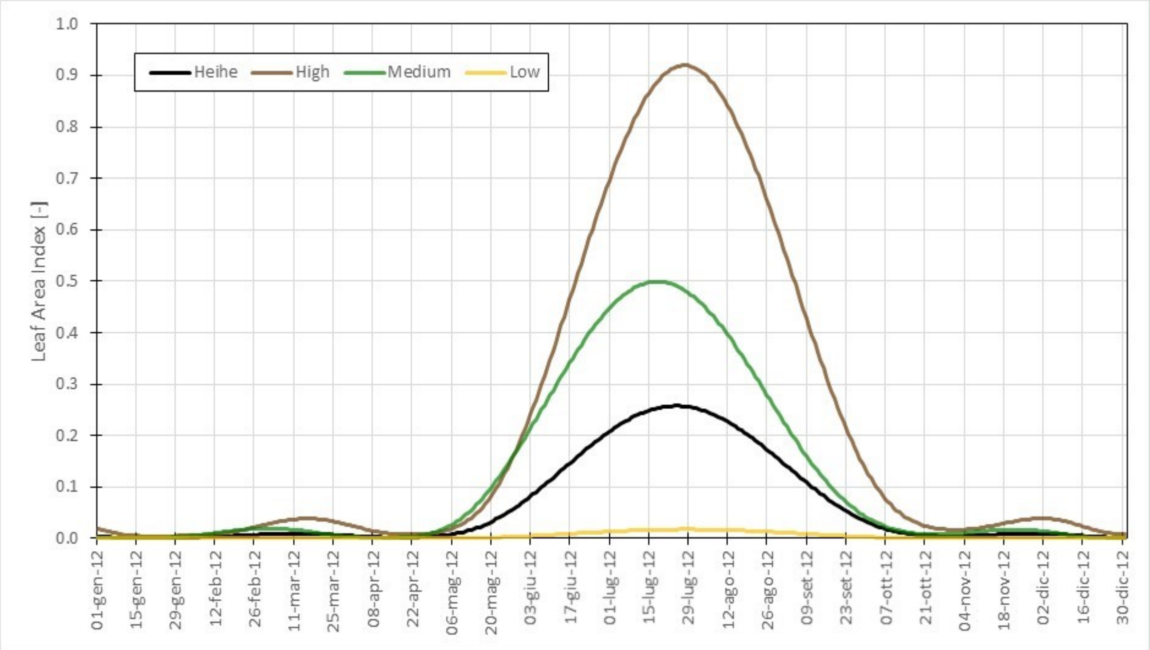

Figure 32 *- Leaf Area Index plot for the whole basin (Heihe) and its sub-regions*

The Leaf Area Index (LAI) is the ratio between the (one-side) leaf area and the total area of the pixel. Highly vegetated pixels can have LAI values bigger than the unit, but this happens only at pixel scale, as evident in the example map below. This index is fundamental in providing some estimate of the transpiration activity of the vegetation (which depends on the leaf surface available for the gaseous transfers with the atmosphere) and the amount of solar radiation that effectively reaches the ground (because of the shadowing mechanisms of a sufficiently dense canopy cover).

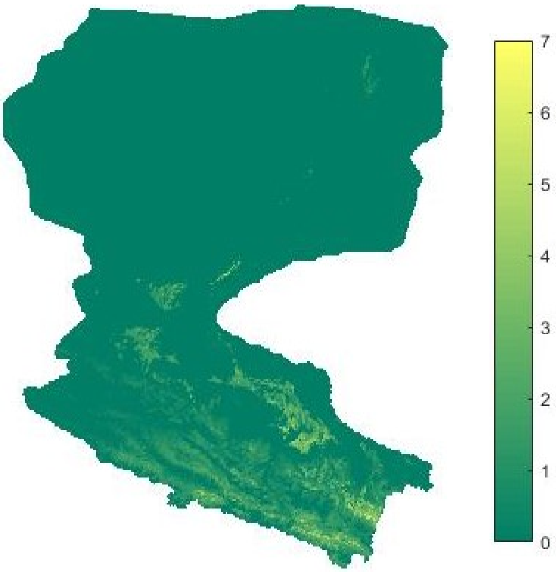

Figure 33 *- Average Leaf Area Index for the summer season*

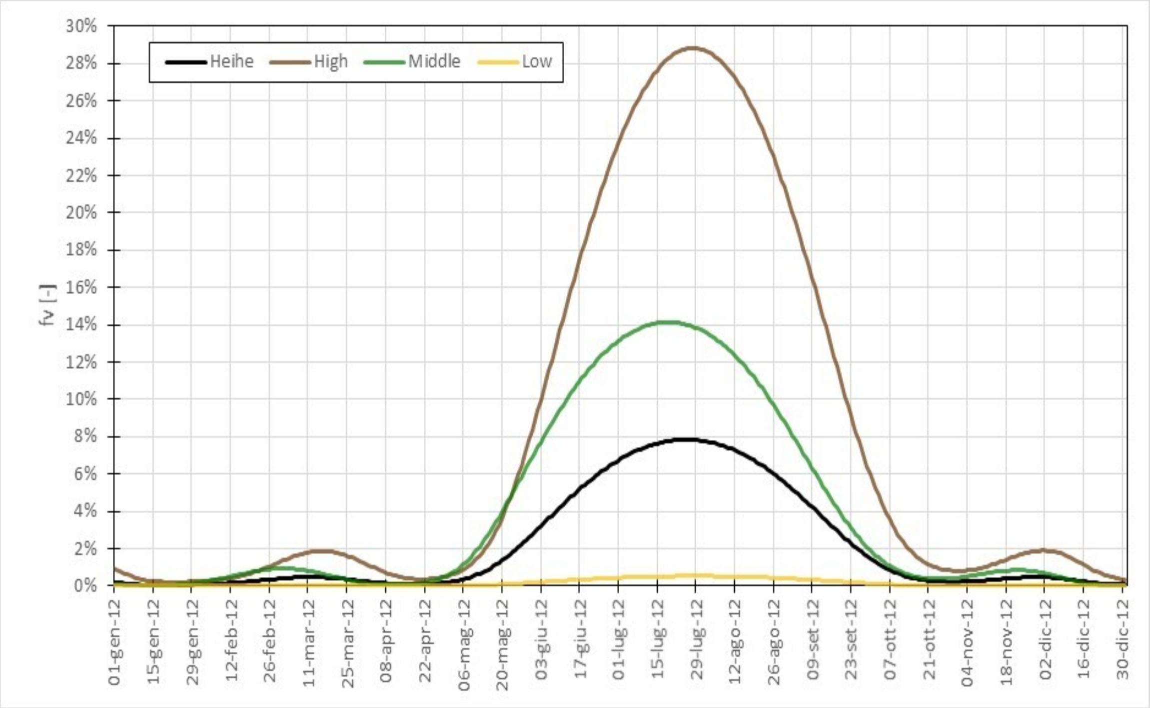

Figure 34 *- Vegetated Fraction plot for the whole basin (Heihe) and its sub-regions*

The vegetated fraction is the amount of basin area which is classified as "vegetated". Such an index can be easily obtained, for example, by analysing NDVI data for the basin, and it is useful to the FEST-EWB model to understand which evapotranspiration law to apply from the Penman-Monteith algorithm.

The almost complete bareness of the desert area is testified by low values all year long, while the mountainous area, which has cooler temperatures and higher precipitations, can sustain a moderate vegetation growth, with a peak of 28.8% of vegetated area.

For the purposes of this study, the index has been derived from the LAI index, employing a relation between the two [Timmermans, 2011]:

$$f_V = 1 - \exp(-0.5 \cdot LAI) \tag{38}$$

2.5 Land cover classes

Each pixel will be assigned to a specific land cover class, in order to establish an emissivity value suited to the characteristics of the emitting/reflecting surface. The European Space Agency (ESA) website hosts the Global Land cover Map, which distinguishes 22 classes.

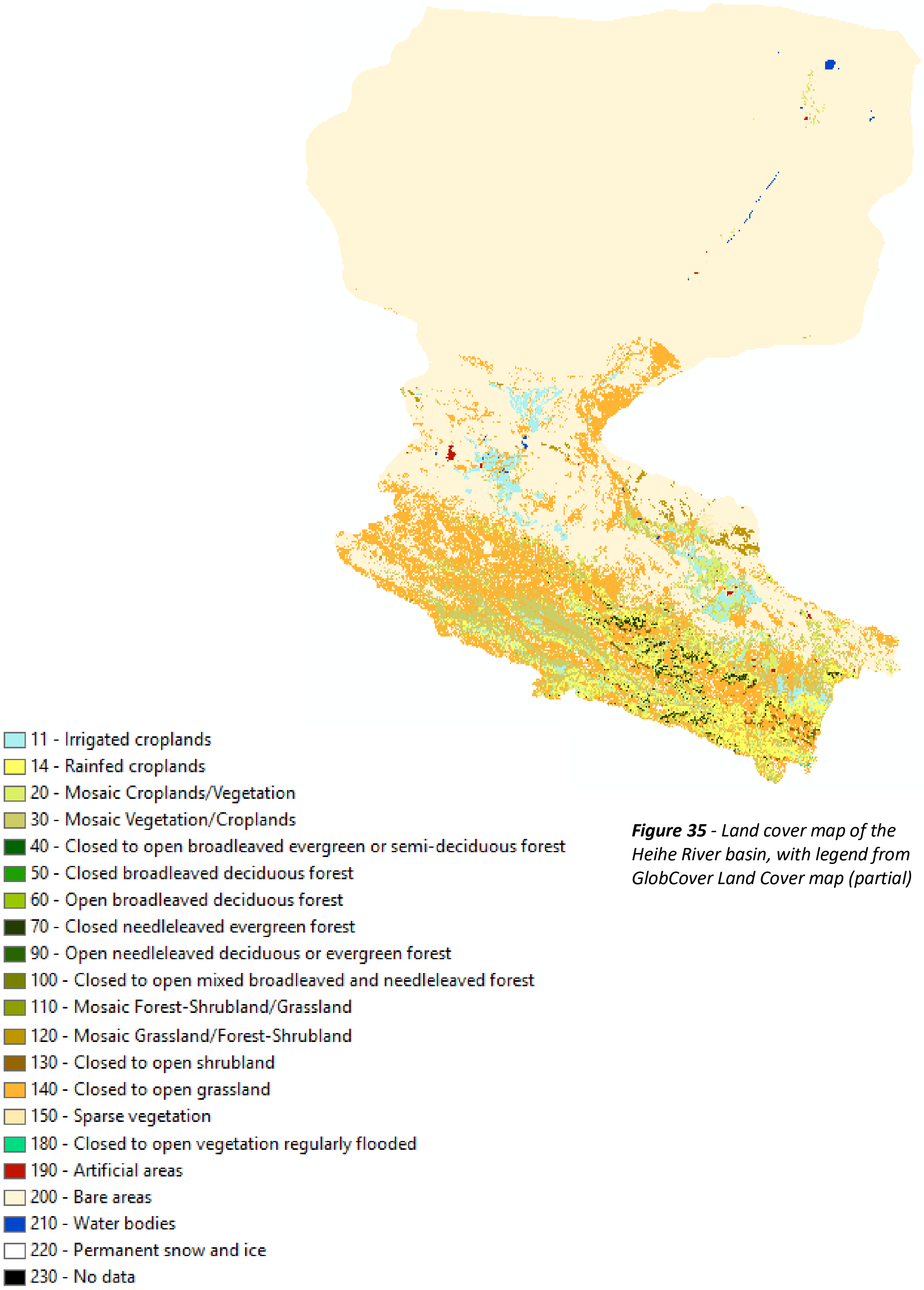

Figure 35 *- Land cover map of the Heihe River basin, with legend from GlobCover Land Cover map (partial)*

For the sake of a more straightforward analysis, these can be grouped together in six macro-categories: cultivated soil (croplands), high-stem vegetated soil (forests), low-stem vegetated soil (shrubs), artificially-covered soil (cities), bare soil (desert) and water/ice-covered soil (waters).

Code	Land cover type	Area	Macro
11	Post-flooding or irrigated croplands (or aquatic)	1.70%	**croplands**
14	Rainfed croplands	2.21%	**croplands**
20	Mosaic cropland (50-70%) / vegetation	2.05%	**croplands**
30	Mosaic vegetation (grassland/shrubland/forest)	4.17%	**shrubs**
40	Closed to open (>15%) broadleaved evergreen or semi-deciduous forest (>5m)	0.00%	**forests**
50	Closed (>40%) broadleaved deciduous forest (>5m)	0.00%	**forests**
60	Open (15-40%) broadleaved deciduous forest/woodland (>5m)	0.00%	**forests**
70	Closed (>40%) needleleaved evergreen forest (>5m)	0.33%	**forests**
90	Open (15-40%) needleleaved deciduous or evergreen forest (>5m)	0.00%	**forests**
100	Closed to open (>15%) mixed broadleaved and needleleaved forest (>5m)	0.12%	**forests**
110	Mosaic forest or shrubland (50-70%) / grassland (20-50%)	0.06%	**forests**
120	Mosaic grassland (50-70%) / forest or shrubland (20-50%)	0.33%	**shrubs**
130	Closed to open (>15%) (broadleaved or needleleaved, evergreen or deciduous) shrubland (<5m)	0.20%	**shrubs**
140	Closed to open (>15%) herbaceous vegetation (grassland, savannas or lichens/mosses)	11.08%	**shrubs**
150	Sparse (<15%) vegetation	0.16%	**shrubs**
160	Closed to open (>15%) broadleaved forest regularly flooded (semi-permanently or temporarily) - Fresh or brackish water	0.00%	**forests**
170	Closed (>40%) broadleaved forest or shrubland permanently flooded - Saline or brackish water	0.00%	**forests**
180	Closed to open (>15%) grassland or woody vegetation on regularly flooded or waterlogged soil - Fresh, brackish or saline water	0.01%	**shrubs**
190	Artificial surfaces and associated areas (Urban areas >50%)	0.07%	**cities**
200	Bare areas	77.12%	**deserts**
210	Water bodies	0.09%	**waters**
220	Permanent snow and ice	0.31%	**waters**

Table 5 *- Land cover re-classification for the Heihe River basin*

Three different categories have been highlighted for canopy-covered soil. The first one is set apart because the agriculture has well-defined seasonal growing patterns, and because the “structure” itself of a cultivated field is obviously quite different from the one of wild land, and as a consequence the water and energy transfer mechanisms can markedly differ. The wild vegetation has been distinguished in low-stem and high-stem for two main reasons: the transpiration mechanisms are different between the two types and the “terrain cover” they provide is different. Having the ground completely shadowed by tall forests changes the dynamics of the water balance, with increased interception (and thus more evaporation) and less solar radiation penetrating the canopy cover.

Cat. ID	Name	Area [km^2]	
1	Croplands	6616	5.95%
2	Forests	556	0.50%
3	Shrubs	17743	15.96%
4	Cities	77	0.07%
5	Deserts	85717	77.12%
6	Waters	437	0.39%

Table 6 *– New land cover classes and their incidence over the total basin area*

2.6 Climatic patterns and meteorological data

The Heihe River Basin qualifies as an area with an Arid cold Desert climate (BWk), according to Köppen climate classification. This tag is true for much of the area, except some parts of the Qilian mountains (cold/semi-arid climate, BSk). These climates see little precipitation, conventionally less than the potential evapotranspiration and usually between 25 mm/y and 200 mm/y. Dry summers and cold, dry winters are a common pattern. Cold/semi-arid climates are the typical transition between arid and Mediterranean/continental-humid areas; these areas show some snow during winter, and feature higher precipitations.

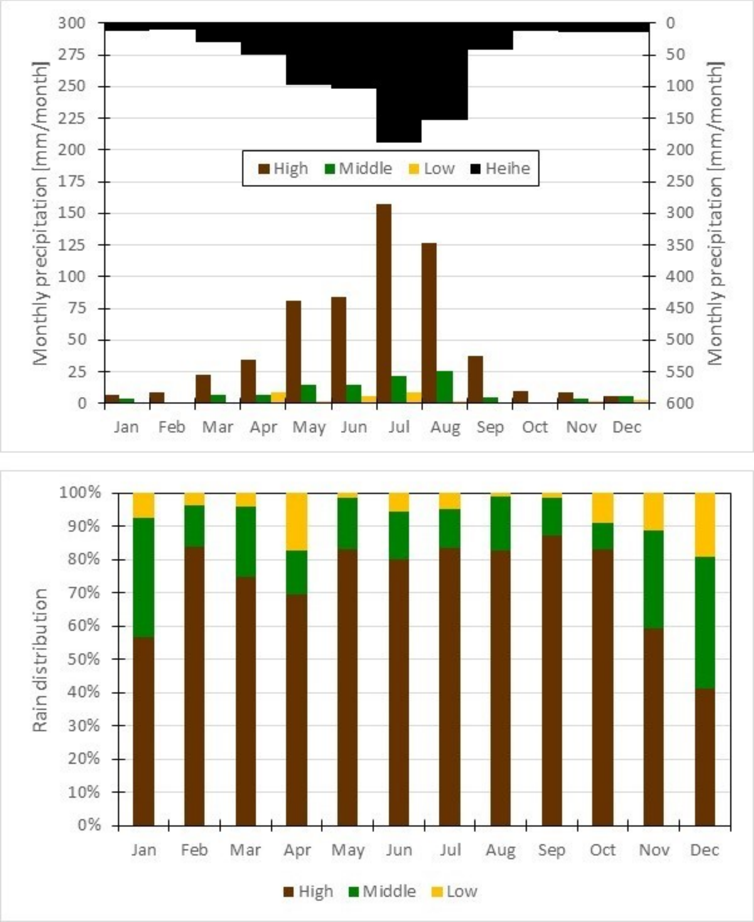

Figure 36 *- Monthly precipitation distribution between the sub-regions*

Meteorological data has been gathered for year 2012 at hourly time frequency with a coarser spatial resolution than the rest of the data (0.05° or *circa* 5000m), from the Chinese National Atmospheric Research centre. Looking into the monthly distribution of the rain patterns, it is evident how most rains are concentrated in late spring and early summer, in particular between May and July. In spite of the lower reaches being the largest by far (almost twice the size of the other two combined), they contribute for less than 5% to the total precipitation amount in the basin. The middle reaches contribute for the 15% while the remaining 80% of the total precipitations falls in the higher reaches.

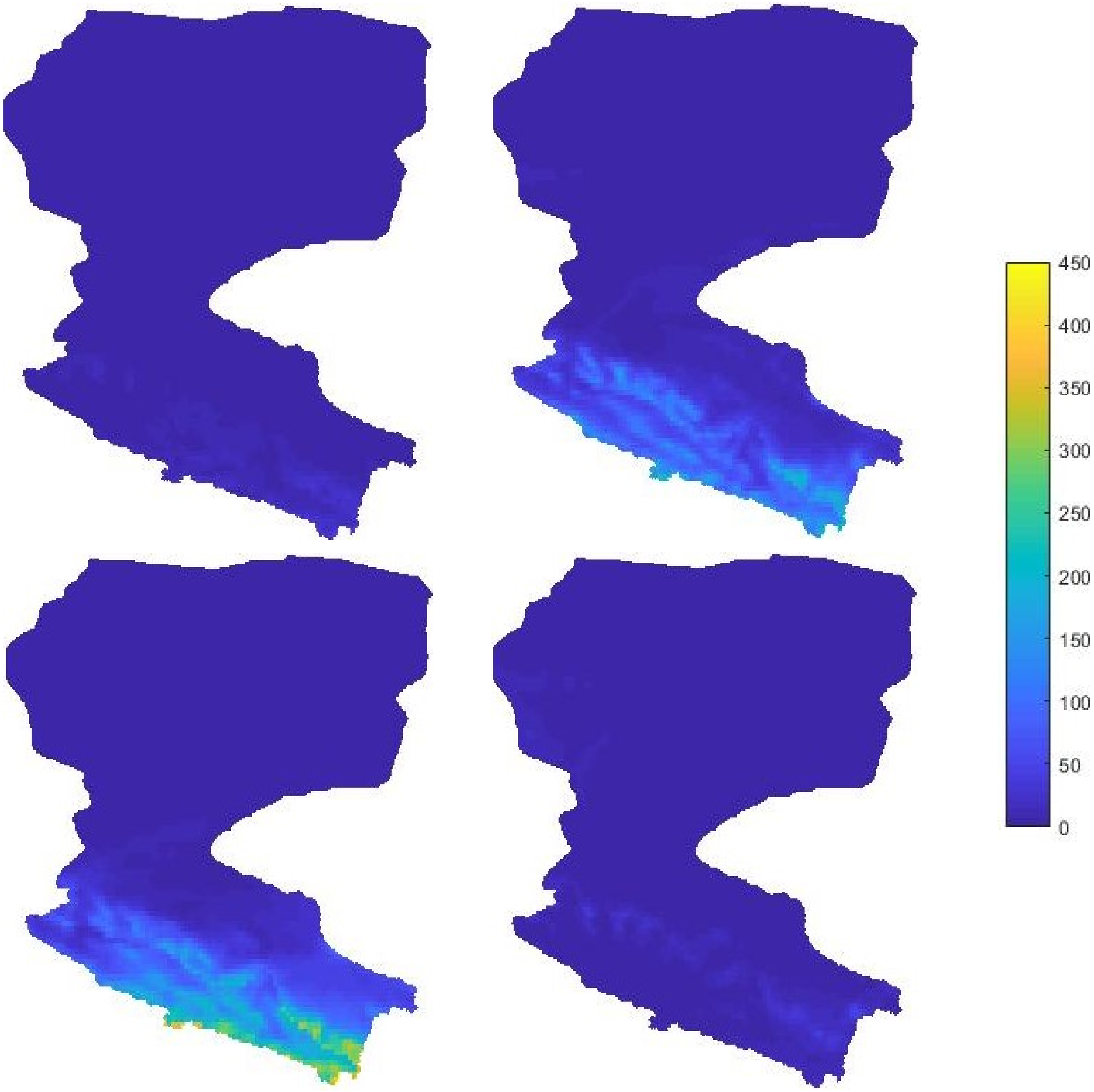

Figure 37 *- Total precipitations for the months of February (first row, left), May (first row, right), August (second row, left) and November (second row, right) 2012 in the Heihe River basin (legend in mm/month)*

Here four rain distribution maps are displayed: they show the total precipitations for February, May, August and November. While the central months of the year reach high values (peaks of 150 mm/month in May and 450 mm/month in August), the autumn-to-winter season has barely visible patterns. Most precipitation is concentrated in the mountainous area: this creates a "rain shadow" effect towards the region immediately northward, contributing to its aridity.

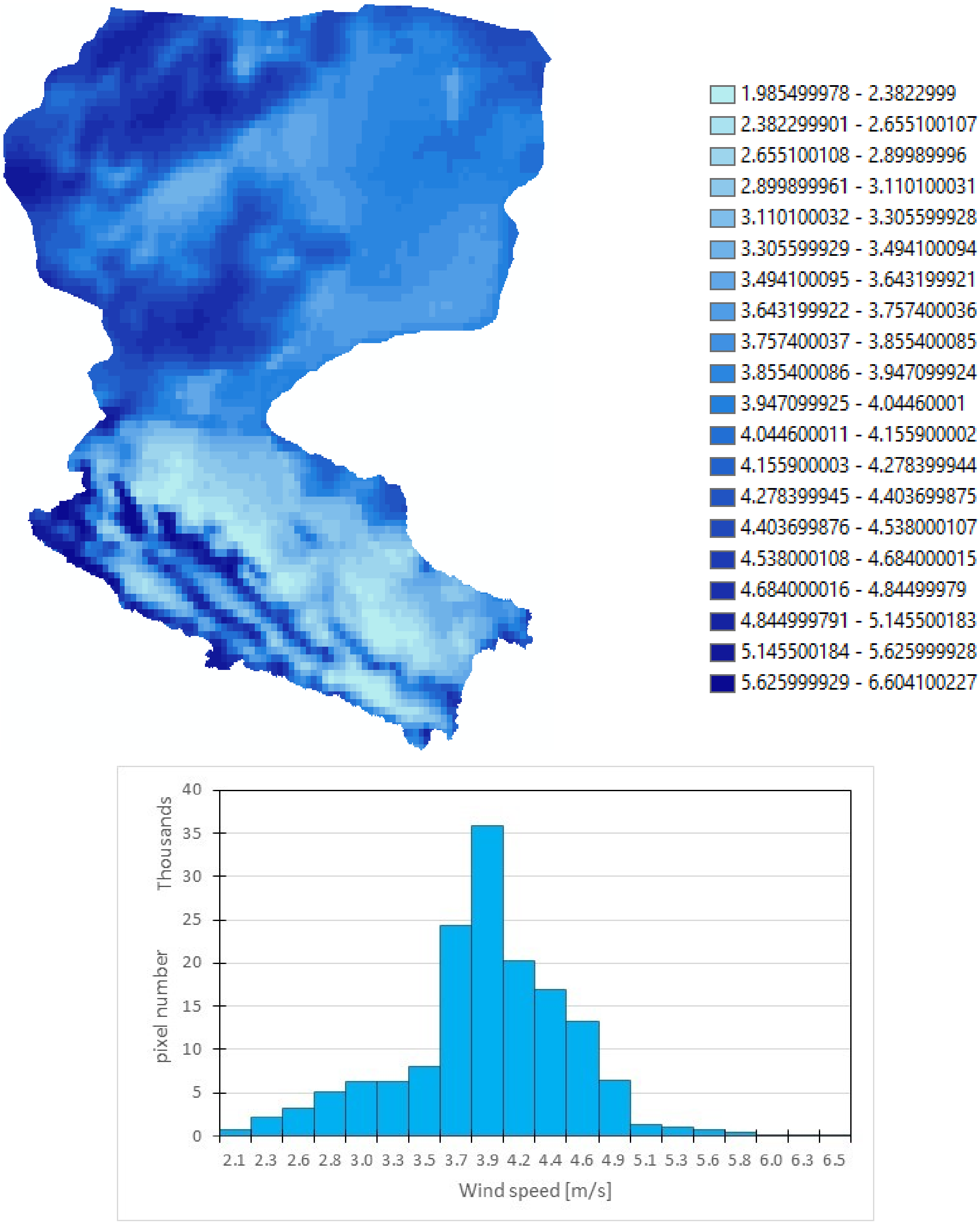

Figure 38 *- Wind speed map and histogram (legend in [m/s])*

Wind conditions are quite influenced by the narrow spaces in the mountain valleys, with the highest registered daily mean values in that area. The desert plain, instead, is less windy. Wind is an important factor for evaporation and transpiration and affects how the theoretical evapotranspiration is effectively converted in actual evapotranspiration as it influences the local humidity above the soil.

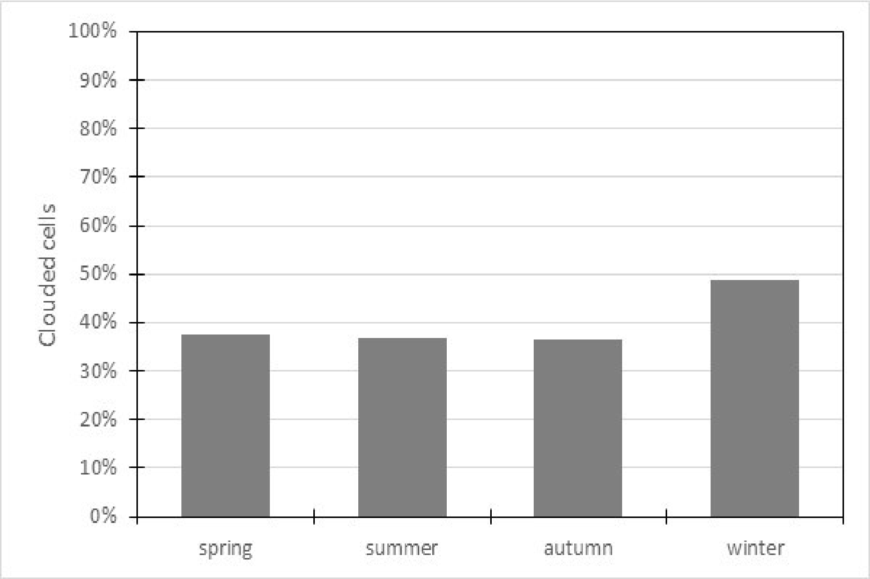

Figure 40 *- Average seasonal values for cloud cover*

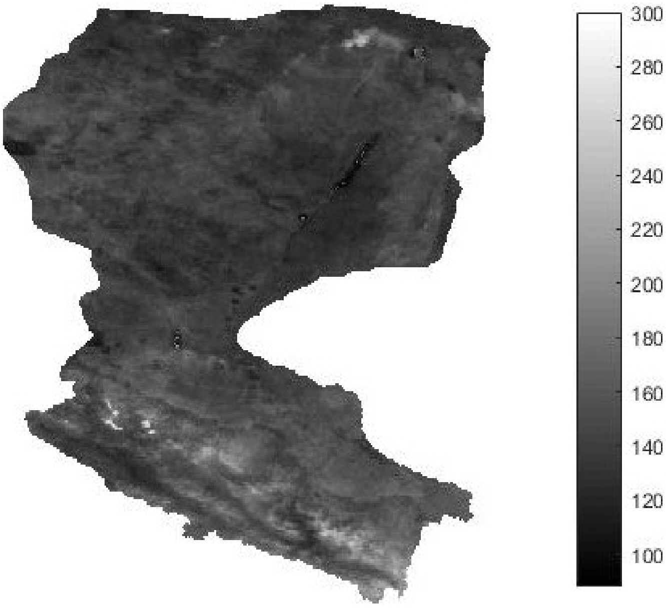

Figure 39 *- Number of clouded days*

Cloud cover is easily retrieved from MODIS' LST product: each clouded pixel is flagged with a "0" value. This has allowed a full reconstruction of the cloud patterns in the basin. No clear trend was found, with a seasonal average cloud cover of 42%; winter was found to be slightly cloudier, but no important difference between the seasons arose. The map above shows the number of days in 2012 in which each pixel was classified as "clouded". As expected, the higher precipitations on the mountain area correspond to a heavier cloud presence, with some pixels which have been clouded 300 days out of 366 in 2012.

Chapter 3

LST downscaling

A performance analysis

Section 1 deals with a methodology overview of the analysis that will be performed. In Section 2 the comparison between MODIS and StarFM is developed, while Section 3 relates the comparison between MODIS and Kustas. Sections 4 and 5 recap the conclusions of the analysis, with some clarifying images from exemplar test dates.

3.1 Methodology

In order to assess the best candidate method to obtain the LST data needed for calibration, a procedure of validation will be performed. The three different sources (MODIS, StarFM algorithm and Kustas algorithm) will be compared with LANDSAT's own data (the highest spatial resolution LST data available but with a temporal resolution of only 16 days).

The performance of each source will be evaluated with common statistical indexes (mean error, RMSE). In order to have more insight, the number of cells (normalized over the whole 'data' cell pool) whose error is located within a given tolerance will be taken into account; tolerances of ±1 K, ±2 K, ±3 K and ±4 K have been selected for this purpose. These quantities will be referred to as "inclusion rates" ρ ($\rho_{\pm1K}$, $\rho_{\pm2K}$, $\rho_{\pm3K}$ and $\rho_{\pm4K}$, respectively).

Furthermore, the comparison will be performed by grouping the pixels according to their land cover and their lighting conditions (light/shadow).

3.2 MODIS v. StarFM algorithm

3.2.1 Choice of the area of interest

Of the 4 LANDSAT paths which cover the Heihe River Basin, the scenes from path 134, rows 31-32-33 have been selected for validation, because of two main qualities:

- they are completely framed within the basin;
- they cover a wide variety of landscapes, from the highest peaks of the Qilian mountains to the southern fringe of the Gobi Desert, just upriver of the Eijna Oasis area, also comprising the urban areas of Zhangye and the cultivated fields nearby.

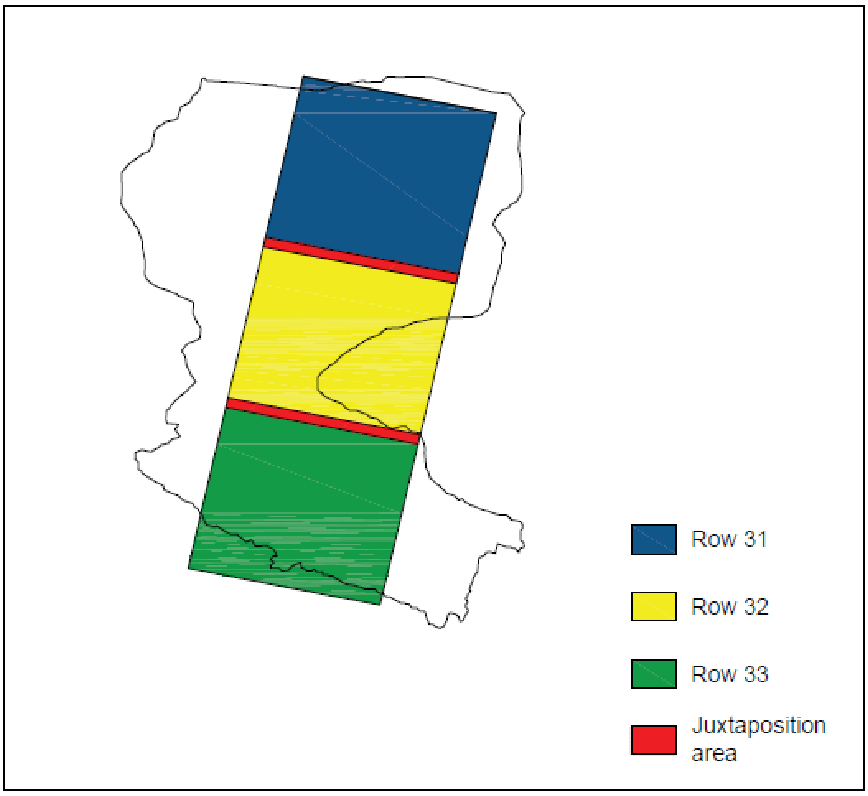

Figure 41 - *Test-area within Heihe River basin*

Due to LANDSAT's 16-days revisit time, the interest area has been sampled 23 times in 2012. However, 9 of these dates (red tag) lack at least one of the three required scenes. Of the 14 remaining images, only 7 have LANDSAT images available 16 days before and after (green tag). StarFM algorithm does not recognize time shifts between the images it is employing, so there would be no differences in using two image couples "close" in time to the target date instead of more distant images; however, the higher-quality results would require the closest available images.

In 4 of the remaining 7 dates, one of the couples was, at best, 32 days distant in time (yellow tag). Although their elaboration will necessarily have a higher degree of uncertainty than the others', they'll be included in the validation as well, enlarging the test-dates pool to 11. The remaining three dates are too far-off from the others, and so will be neglected (blue tag). This reasoning yields 11 test-dates, unevenly distributed through the year. Spring and Summer are represented by 4 dates each, while autumn features 2 dates and winter only 1.

DOY	**Date**	**Notes**	
7	7th January 2012	Data available	🟩
23	23rd January 2012	Data available	🟦
39	8th February 2012	Incomplete data	🟥
55	24th February 2012	Incomplete data	🟥
71	11th March 2012	Incomplete data	🟥
87	27th March 2012	Incomplete data	🟥
103	12th April 2012	Data available	🟦
119	28th April 2012	Data available	🟩
135	14th May 2012	Data available	🟩
151	30th May 2012	Data available	🟩
167	15th June 2012	Data available	🟨
183	1st July 2012	Incomplete data	🟥
199	17th July 2012	Data available	🟨
215	2nd August 2012	Data available	🟩
231	18th August 2012	Data available	🟩
247	3rd September 2012	Data available	🟨
263	19th September 2012	Incomplete data	🟥
279	5th October 2012	Data available	🟨
295	21st October 2012	Data available	🟩
311	6th November 2012	Data available	🟦
327	22nd November 2012	Incomplete data	🟥
343	8th December 2012	Incomplete data	🟥
359	24th December 2012	Incomplete data	🟥

Table 7 *- LANDSAT 7 passages on the test area in 2012 on the respective data availability*

3.2.2 General comparison

Before actually comparing the results, the possible dependency of estimation errors on the cloud cover will be investigated. The following plots feature the error means and RMSE of MODIS and StarFM with respect to the "reference" LANDSAT data.

The chosen dates have a variety of cloud cover values, all below 30%, but that does not seem to influence either RMSE or error mean. An example of that is the difference in the error between 2nd August and 21st October, dates that both share a similar value for cloud cover (16.3% and 15.1%, respectively), but have quite different errors ($RMSE_{2ago}$=14.8 K, $RMSE_{21ott}$=4.47 K for MODIS, while $RMSE_{2ago}$=20 K, $RMSE_{21ott}$=9.15 K for StarFM).

Figure 42 *- Mean error and RMSE for MODIS and StarFM*

Assessed that cloud cover does not play a part in the sources' performances, the mean error and RMSE are looked into. Error means seem to be biased by a systematic error for the MODIS data, as they are all positive (meaning that MODIS overestimates the actual temperature); this does not happen for the StarFM, which shows cases of lower mean errors (in 3 days the error is lower than 2.23 K, the lowest mean error for MODIS), some of which are negative (the StarFM meanly underestimates the temperature). Although MODIS data seem to be somewhat biased, their RMSE are, overall, lower than the StarFM's:

$$\overline{RMSE}_{MODIS} = 6.73\ K < 15.65\ K = \overline{RMSE}_{StarFM}$$

The inclusion rates (relative number of cells whose error falls within a given tolerance) show how MODIS' work is more effective: 9 out of 11 test-dates show an inclusion rate higher than 50% at the highest tolerance (±4 K). This means that, 9 times out of 11, more than half of the MODIS temperatures do not mistake the actual value for more than 4 K. In most of these cases (6 out of 9) the inclusion rate is higher than 60%, surpassing 70% on 21st October.

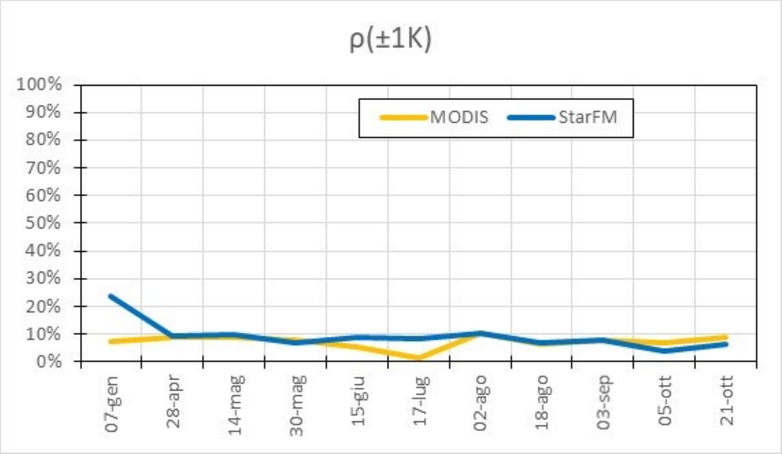

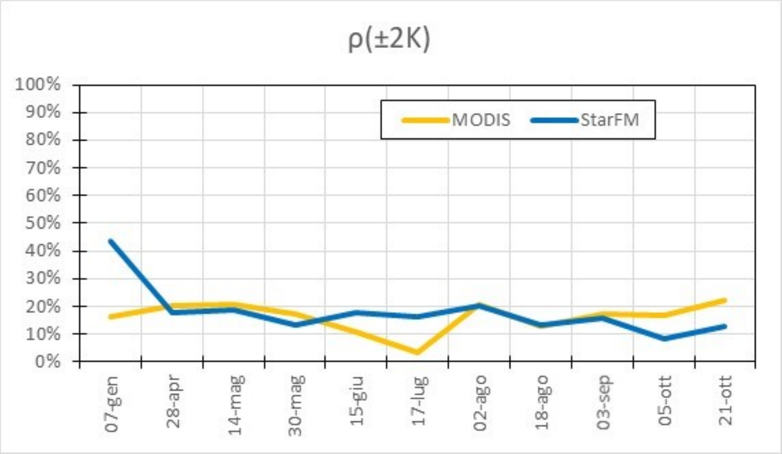

Figure 43 *- Inclusion rates for MODIS and StarFM*

Aggregating the data by season, MODIS keeps outperforming the StarFM. For MODIS, the "weakest"-performing season seems to be summer (highest errors and lowest inclusion rates), while StarFM works the worst in autumn.

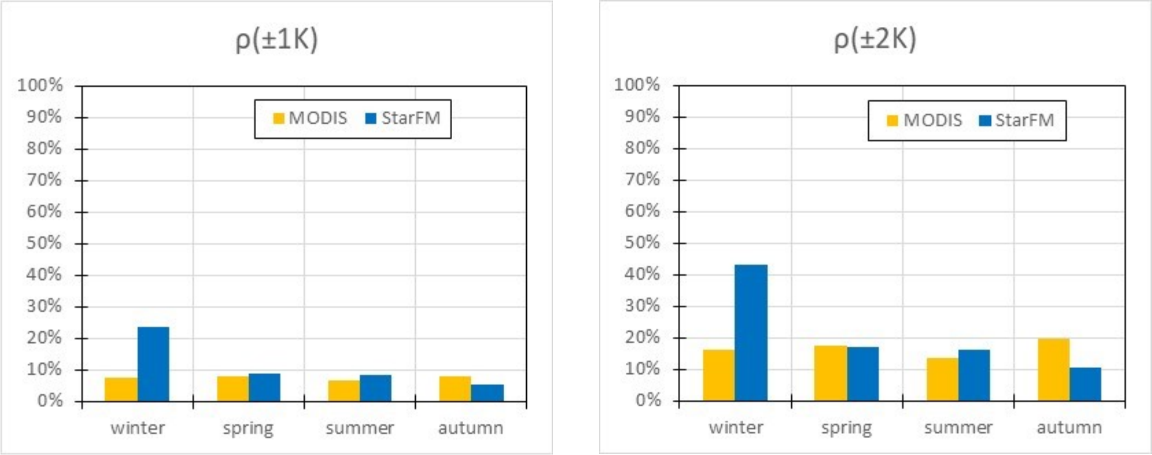

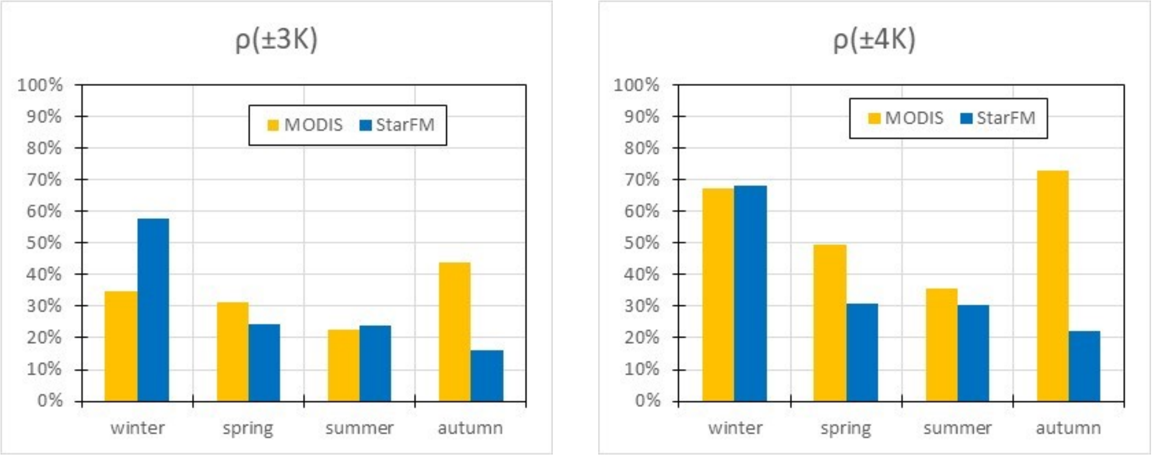

Figure 44 *- Seasonally grouped Inclusion rates for MODIS and StarFM*

At season level, an interesting statistic is the spread between MODIS' inclusion rate and StarFM's. The most important thing to notice is that, while both MODIS' and the StarFM's performance grow with the tolerance, MODIS' inclusion rates grow faster, as witnessed by their spreads, which grow with tolerance too. Even though neither method reaches an optimal (>90%) inclusion rate within acceptable tolerances, MODIS errors are more densely concentrated around the (optimal) zero-error: the gain obtained in adding ±1K to the tolerance is far better when using MODIS data than StarFM algorithm.

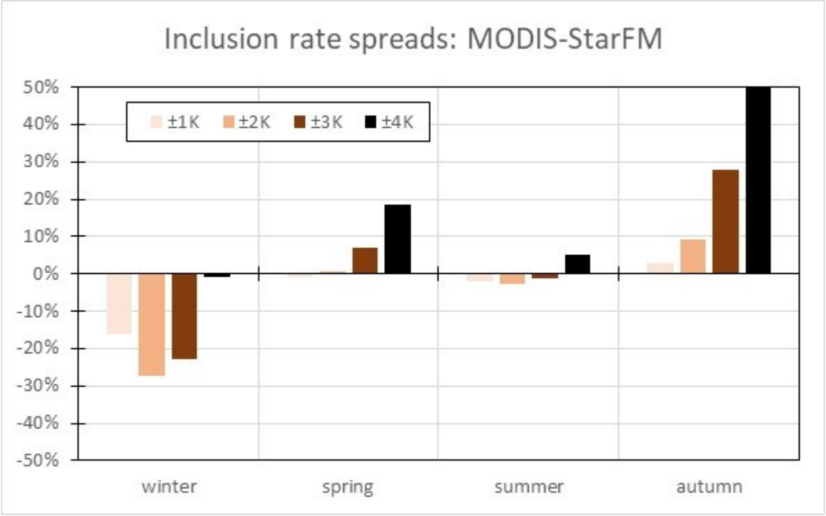

Figure 45 *- Inclusion rate spreads between MODIS and StarFM for different tolerances*

Data from 7th January seems to stand out as quite different from the rest: StarFM performs very well, far better than the rest of the year. Unfortunately, every consideration that could be inferred from such behaviour about the sources' performances during winter would be quite weak, because of the lack of other winter data. Data from 7th Jan is reported in the rest of the study for the sake of completeness, but without indulging too much on any analysis.

3.2.3 Analysis by land cover

Of the 6 macro-categories detected in the basin, water and artificial surfaces are the least important. Firstly, because together they account for <0.50% of the whole basin; secondly, because the data involving them has some inaccuracies, which will be discussed in the proper sections.

3.2.3.1 Croplands

Main cultivations in the region are developed in the middle reaches of the river and consist of maize and wheat [Wang et al, 2011]. The growing season reaches its apex between July and August, but there seems to be no clear pattern visible in the data for that period.

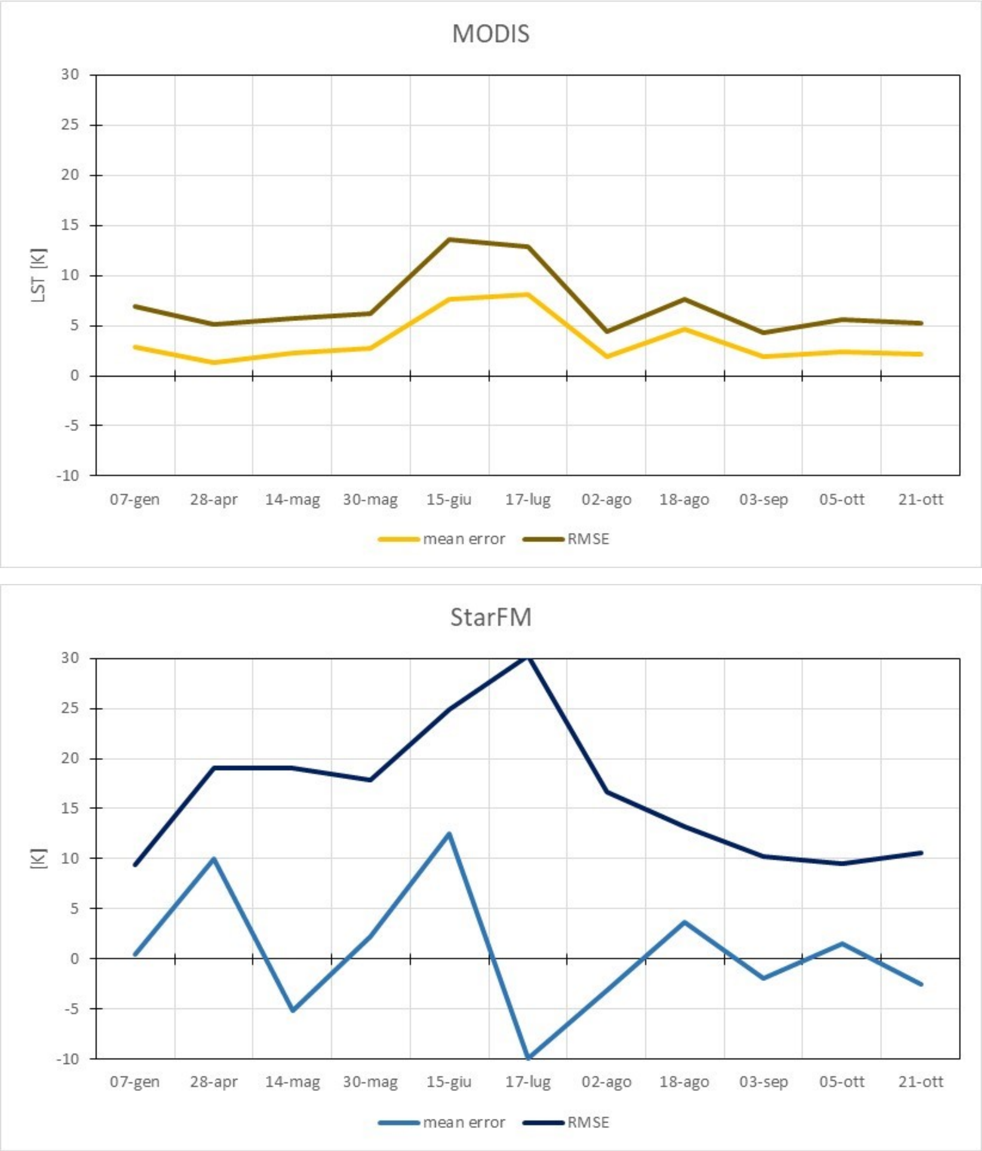

Figure 46 *- Mean error and RMSE for MODIS and StarFM (croplands)*

MODIS, in particular, has too low a resolution to distinguish the single crop fields, and shows an overall increase in RMSE (+8.3% on average) over the whole basin. StarFM algorithm underperforms as well (on average +9.2% in RMSE), in particular in the June-July period, a little "out-of-phase" with MODIS.

The inclusion rates show some "seasonality" in MODIS' behaviour, with a steady decline in performances until the end of July, before recovering the values of the start of the year. This can be a result of MODIS' inability to appreciate what happens at crop field scale during the growing period. StarFM algorithm displays a similar pattern, with the best results in late summer and autumn, after the growing season.

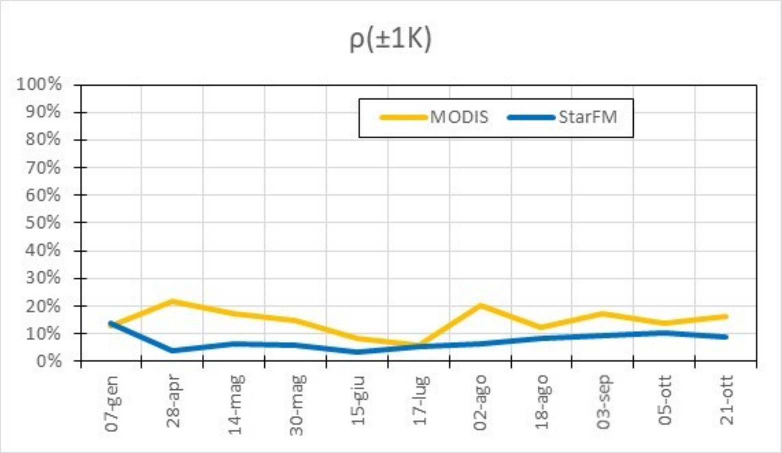

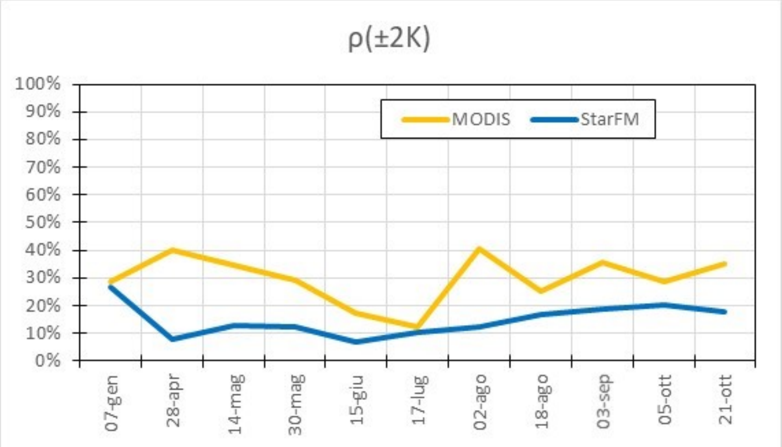

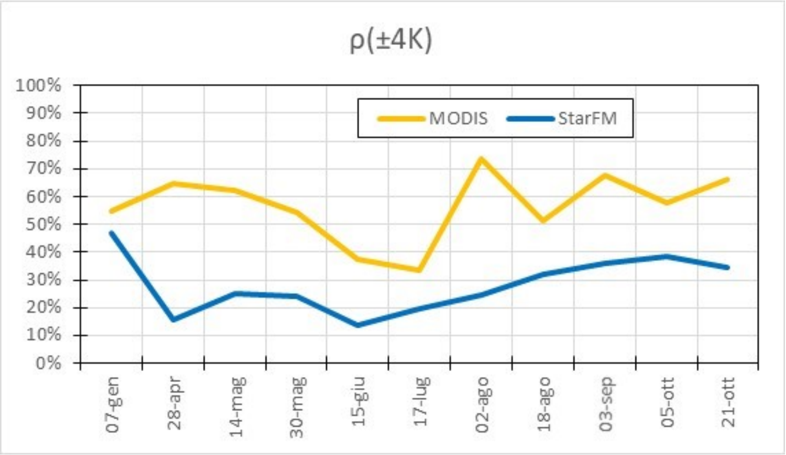

Figure 47 *- Inclusion rates for MODIS and StarFM (croplands)*

In spite of these underperformances, MODIS keeps working better, as shown by the spreads, always above +20% in the medium-high tolerances.

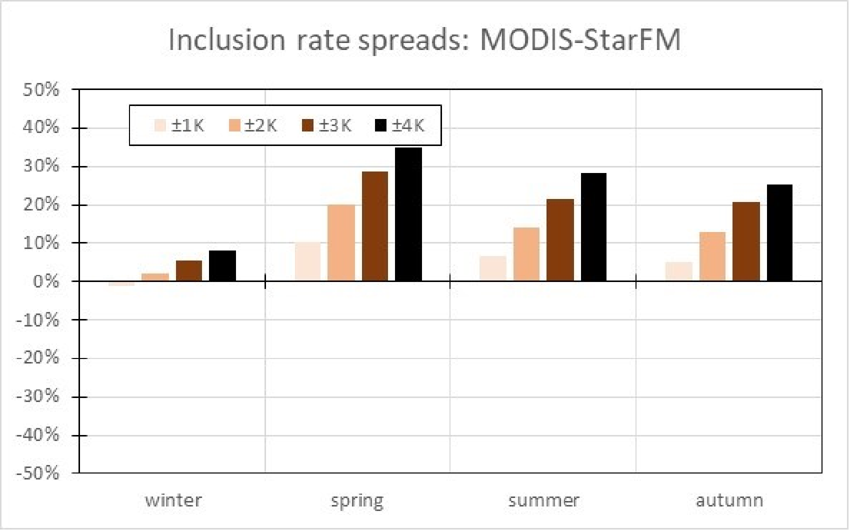

Figure 48 *- Inclusion rate spreads between MODIS and StarFM for different tolerances*

3.2.3.2 Forests

Tall vegetation show patterns not too different from the croplands. Higher errors are featured in the spring-summer period than in the post-flowering season, between late summer and the end of the year.

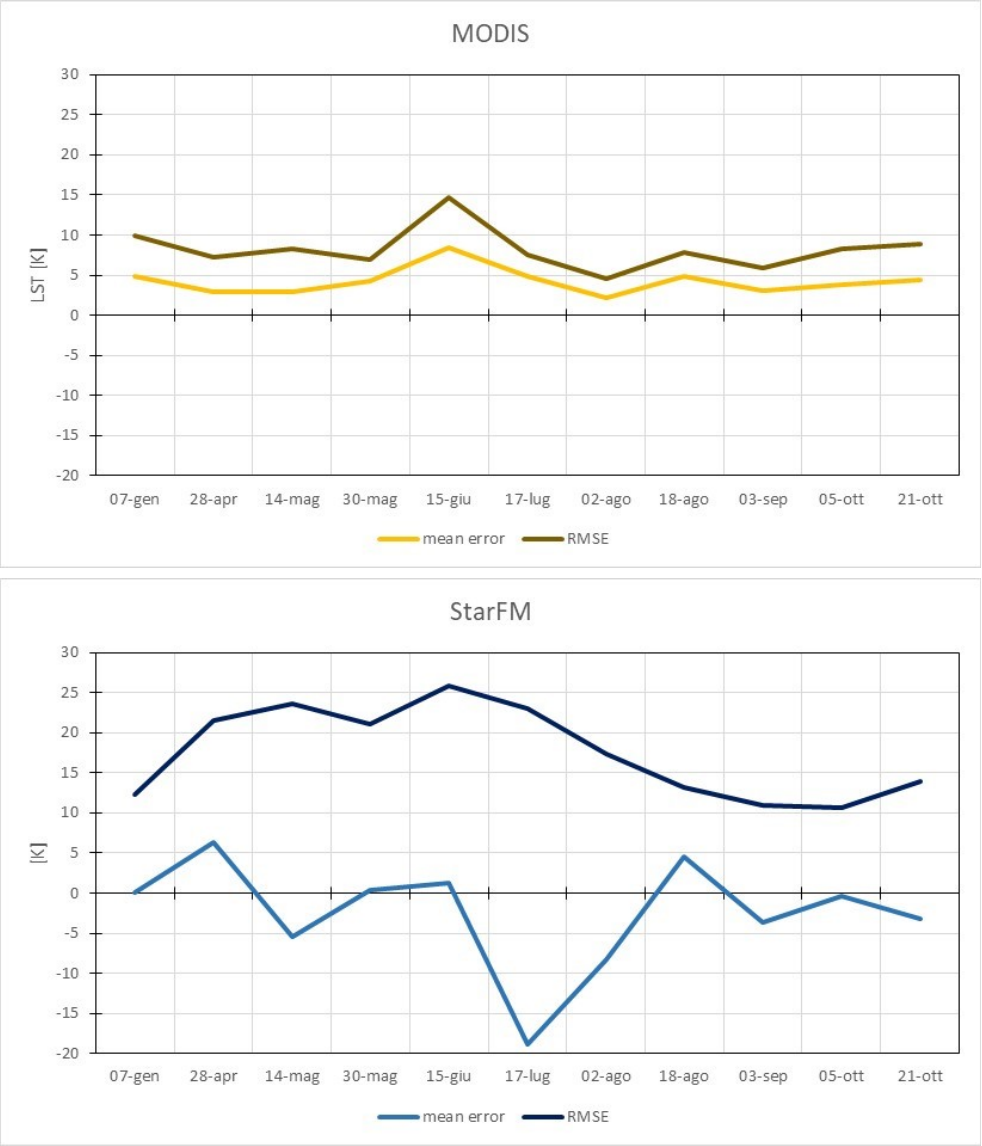

Figure 49 *- Mean error and RMSE for MODIS and StarFM (forests)*

However similar as the behaviours may be, in this case the RMSE increases markedly: StarFM's surges +20.9% on average, while MODIS' exceeds the 30% mark (+35.1%).

This general pattern can be explained by the intermixing between different pixel types: "forest" pixels are few (~430'000 pixels, that is ~387km^2 or the 0.43% of the whole basin) and often next to "cropland" pixels. Thus, the distinction can be ambiguous between the two (each pixel is assigned to one category, even if part of it would have belonged to another, had a finer resolution been used), and the behaviours do not differ much.

3.2.3.3 Shrubs

Shrubs and low-lying vegetation cover the middle-to-high reaches of the river, around the highest mountain peaks.

Figure 50 *- Mean error and RMSE for MODIS and StarFM (shrubs)*

MODIS error means seem to lose their systematisms with 9 days out of 11 showing negative values. Overall the RMSE has again surged (+10.4%), but not because of a consistent overestimation (as testified by the signs of the error means). The StarFM, however less performing (the RMSE grows), shows a slightly better performance than for cultivated lands or high trees: the average increase in RMSE for StarFM is +8.0% for the “shrubs” category, against the +20.9% seen for forests.

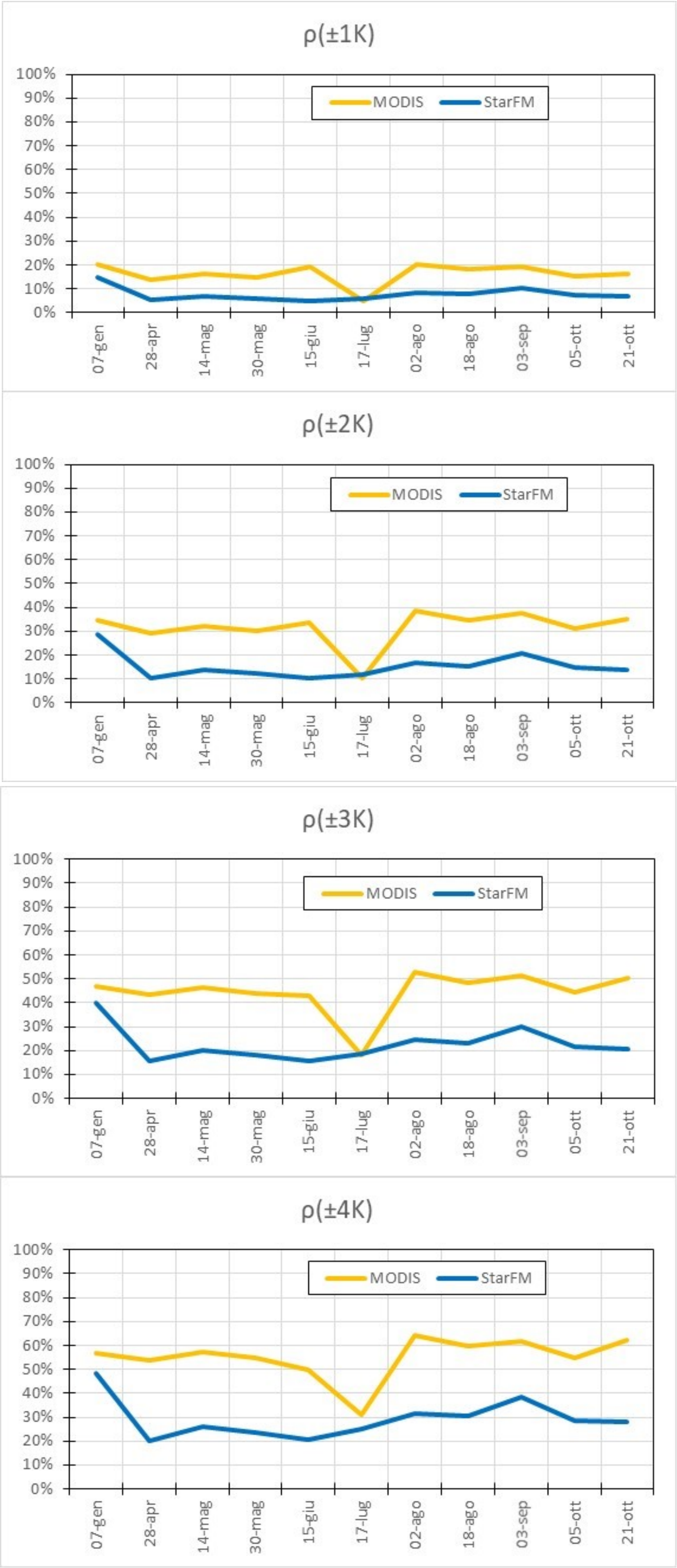

Figure 51 *- Inclusion rates for MODIS and StarFM (shrubs)*

No major seasonal pattern is detected; in fact, inclusion rates for MODIS seem to stabilize independently of the sampling date: at ±4 K tolerance, ρ values are all found within ±10%, and almost all stand above 50% (with the exception of 17th July, with a uniquely low performance).

A little more variety ($\sigma_{RMSE}^{(StarFM)} = 7.7\% > 3.9\% = \sigma_{RMSE}^{(modis)}$) is found in the StarFM performance, but the overall "a-seasonal" behaviour is found also in this source. All this is reflected in the spreads, which have comparable patterns all year long.

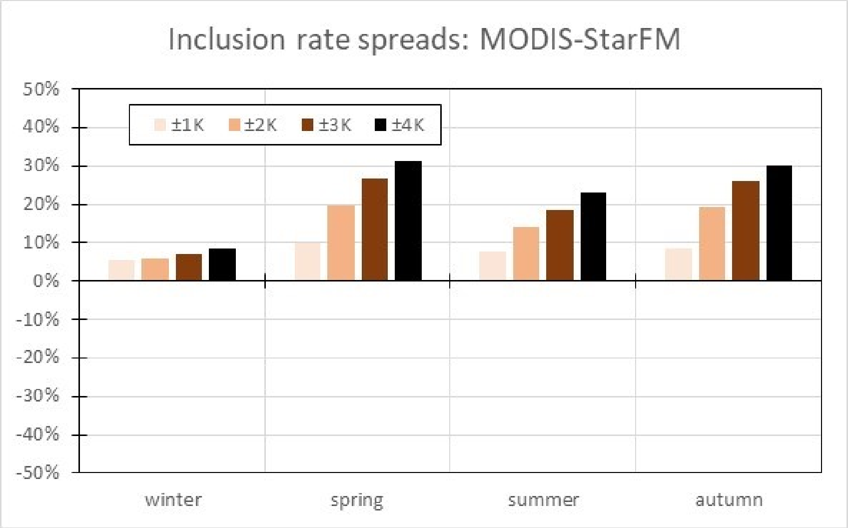

***Figure 52** - Inclusion rate spreads between MODIS and StarFM for different tolerances (shrubs)*

This category seems to feature the most "stable" data, time-wise. Such a result is coherent with the nature of the pixels themselves: wild vegetation is far more diverse than cultivations, both in growing patterns and heat emission mechanisms. Such a variety cannot result in clear patterns, being the superposition of many different timings and mechanisms.

3.2.3.4 Artificial

Artificial covers constitute quite a negligible part of the basin (~0.04%) and thus have little to no importance in this model's calibration. However, a little information can be gathered by looking at these data. MODIS performs surprisingly well, with a lowering of the average RMSE (-5.0%); the performances seem to be particularly good in the winter-autumn dates. The StarFM, on the other hand, has a consistent increase in RMSE (the average value surges +17.3%), reaching the highest value for the whole study on 17th July: 35.5 K.

These considerations, however, have less “value”, as no thorough analysis on the materials used for the artificial covers has been conducted. A representative value for emissivity has been used, but a higher level of detail would be required to perform a “scientifically orthodox” study. This exceeding the goals of this study, the topic will not be developed further.

3.2.3.5 Desert

The most consistently present category in the basin (~72% of the test area), it has been further characterized with different values for the emissivity to account for the diverse composition of the soil.

Figure 53 *- Mean error and RMSE for MODIS and StarFM (desert)*

MODIS data feature a "biased" error mean, characteristic of the whole test area, showing a -6.2% average decrease in RMSE. The absence of vegetation is evidently a better setup for the instrument's low resolution, as the area to be sampled has higher homogeneity. StarFM too performs well, being this the only land cover type for which its average variation of RMSE is a decrease (-4.9%). Generally speaking, the homogeneity of this land cover type is simpler to interpret for both MODIS' 1000m spatial resolution and StarFM's processing algorithm.

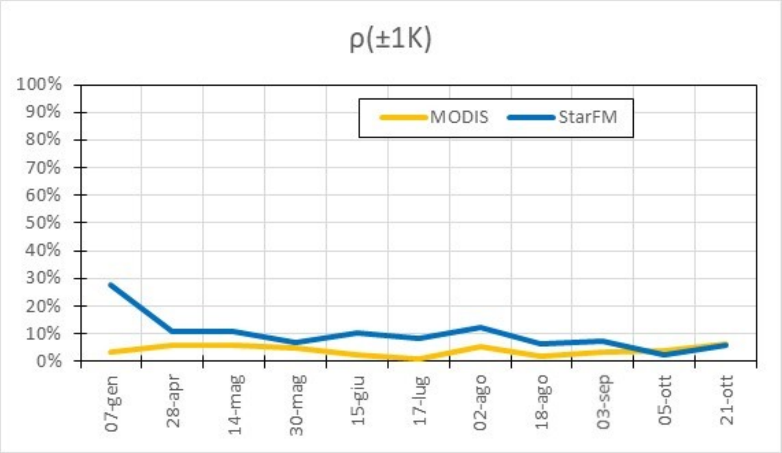

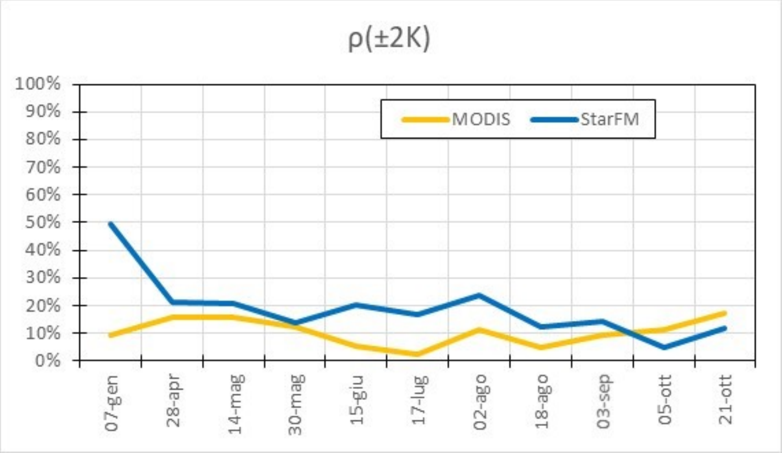

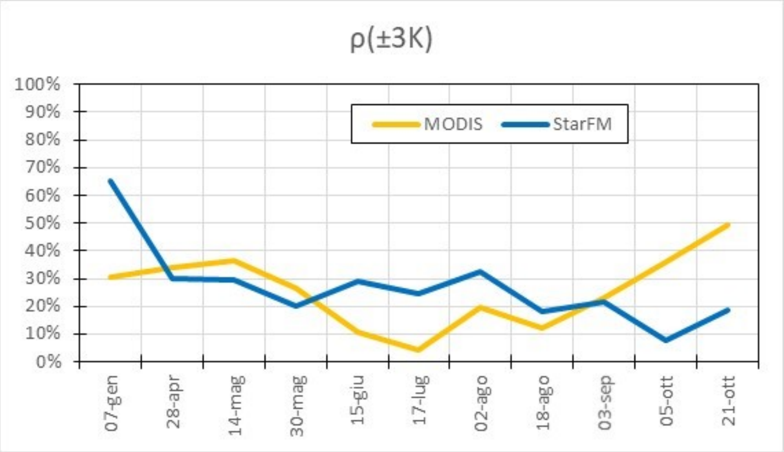

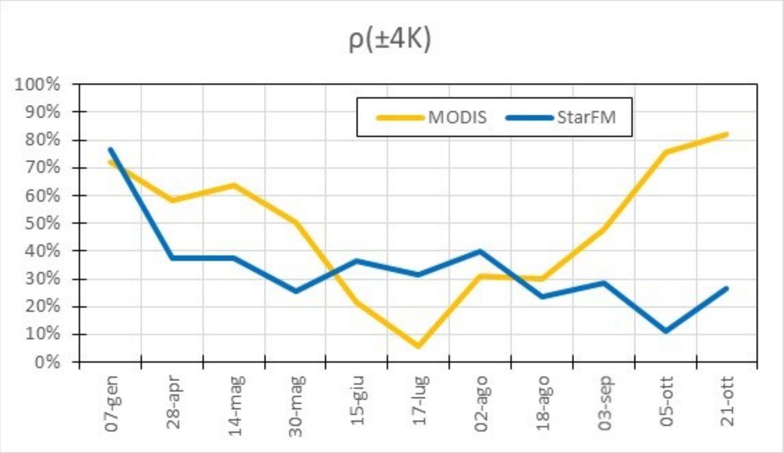

Figure 54 *- Inclusion rates for MODIS and StarFM (desert)*

Inclusion rates seem to be quite stable (except a slight decrease in the end of the year) for StarFM, while have an underperformance dip around mid-summer for MODIS. In this category, StarFM outperforms MODIS more than in any other: 8 dates out of 11 at ±1K tolerance, 7/11 at ±2K, 4/11 at 3K and 2/11 at 4K. This fact is quite strong also at seasonal level, as shown by the spreads.

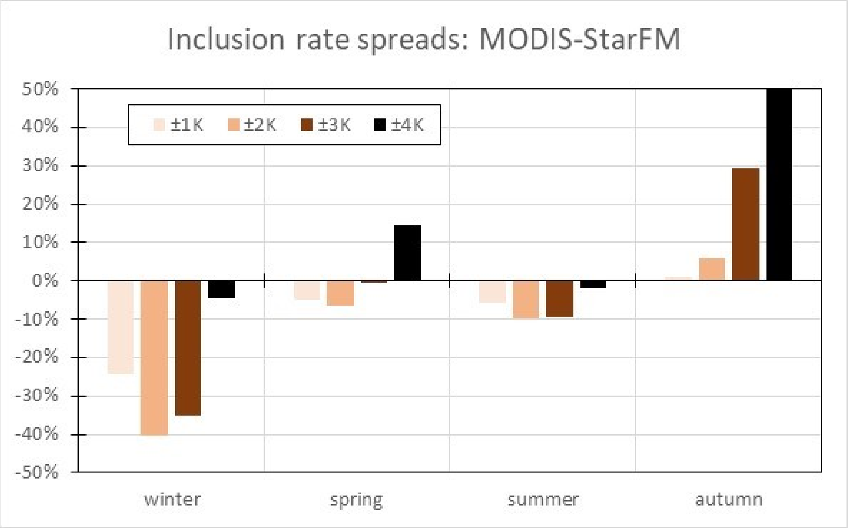

Figure 55 *- Inclusion rate spreads between MODIS and StarFM for different tolerances (desert)*

3.2.3.6 Water

Lastly, the category classified as "water" is discussed. This includes any water status, like snow or ice. The lowest inclusion rates (scarcely reaching 50% at ±4K tolerance) are obtained for this category, for which both MODIS and the StarFM show an important average increase in their RMSE (+48.0% and +32.7%, respectively). This data, however, is originally flawed because water-pixel detection has been conducted using a stationary mask, which does not account for the extension-retreat of the snow cover or of the two terminal lakes in the Ejina Oasis area. In both cases, considering as "water" areas that in fact are dry wasteland or rocky and vegetated mountain strongly affects data quality.

3.2.4 Analysis by illumination degree

Mountainous regions often offer the most difficult challenges to Remote Sensing applications.

- The highly changeable terrain can display features hard to recognize for (relatively) low-resolution instruments (like MODIS)
- The importance of radiance reflected from neighbouring pixels increases, adding to the uncertainty already present in the model or instrument
- Planck's Law requires Lambertian emitting surfaces, that is isotropic radiation; such a hypothesis is actually almost never satisfied, but the error thus generated is usually negligible. However, the more rugged the terrain is, the higher the error

In order to try and "isolate" the more "problematic" pixels, an algorithm (developed by [Corbari et al, 2011]) has been employed to detect "shadowed" pixels. This computes the position of the sun, expressed through its azimuth and elevation angles, using the reference latitude/longitude of each pixel and knowing the exact moment of the satellite sampling during the year. The Solar Elevation is then compared with the so-called Topographic Angle, which is the angle, with respect to the horizontal, at which the nearest obstacle in the Solar Azimuth direction is seen from the observation point.

Each date shows an almost negligible presence of shadowed pixels, reaching, at best, the 3.50% of the total area. The light-pixels/shadow-pixels ratio goes as high as 4541, on 17th July, when only 0.022% of the area is "in shadow".

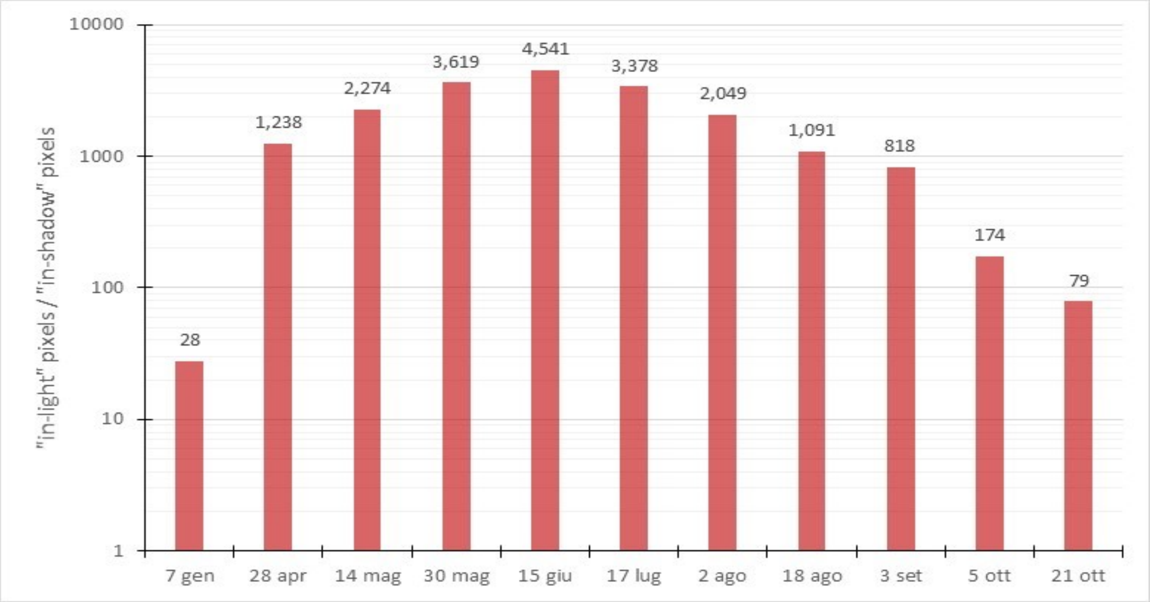

Figure 56 *- Light/Shadow ratio for each test date*

3.2.4.1 "In-light" pixels

At global level, both MODIS and StarFM benefit from the exclusion of shadowed pixels. Looking at average RMSE variations, both cases show barely noticeable decreases (-0.85% and -0.93%, respectively). The magnitude of such decreases can be explained with the little amount of pixels removed.

Such a (practically negligible) variation does not affect much the inclusion rate patterns, date-to-date or at seasonal level, as can be confirmed by the similarity between the error plots of the "in light" pixels (in the images below) and the ones of the whole basin seen before.

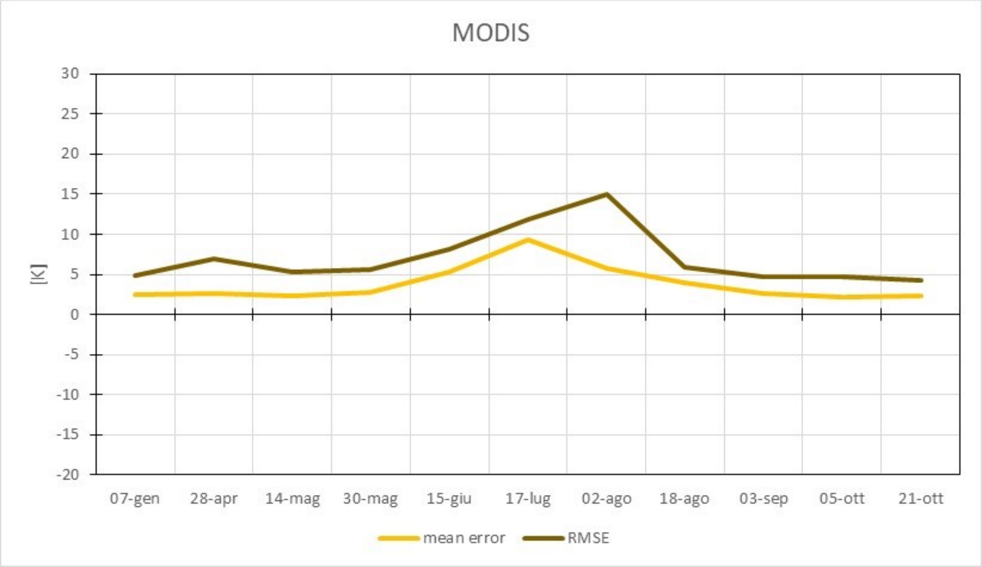

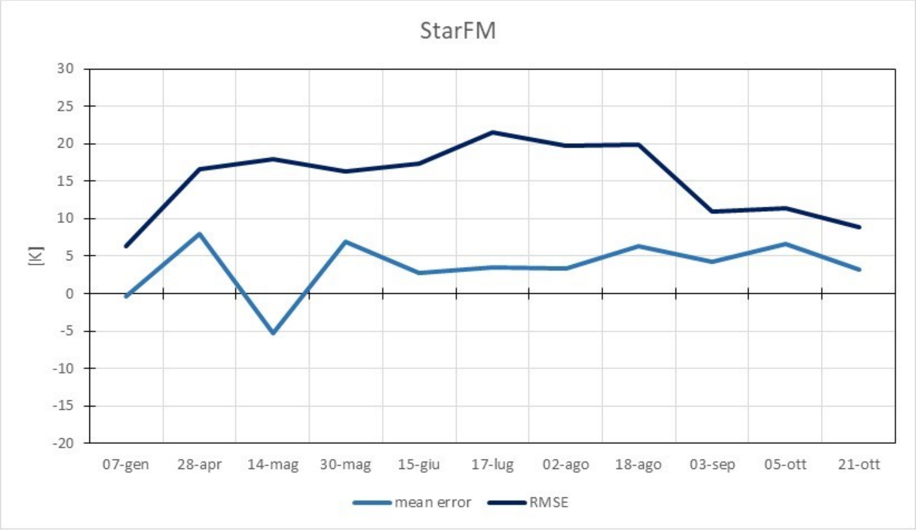

Figure 57 *- Mean error and RMSE for MODIS and StarFM ("in-light" pixels)*

3.2.4.2 "In-shadow" pixels

Even if the exclusion of "in-shadow" pixels does not seem to improve effectively the results, it can be useful to understand whether the low impact of such exclusion is due only to the pixels' little number, or to an actual low quality.

In fact, "in-shadow" pixels show a much lower quality, with important average increases in RMSE (+24.8% for StarFM, +40% for MODIS). Looking at seasonal data, a different pattern than usual is found for the spreads. In summer and autumn they do not reach 10%: this means that, when dealing with "problematic" pixels, StarFM "suffers" the poor quality of the data less than MODIS. The latter still outperforms the former, but with a minor margin than usual. This suggests that, when using MODIS data, excluding shadowed pixels can be a useful decision, as their quality is usually far inferior than the others'. Such a problem is not so heavy for the StarFM, for which shadowed data cause less trouble.

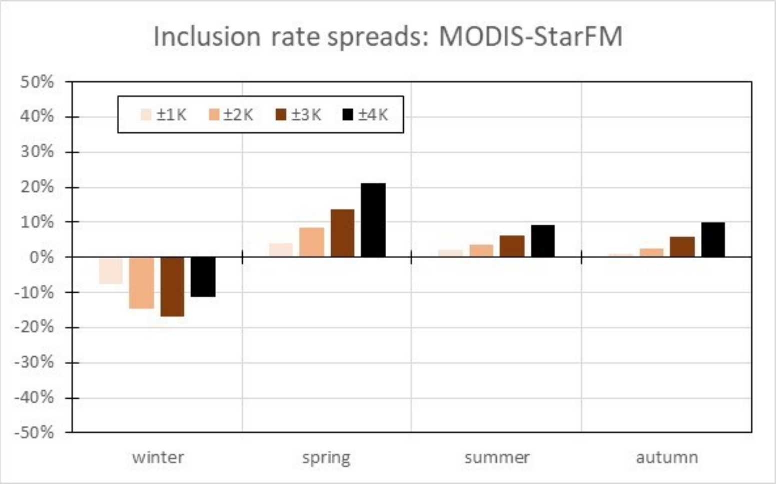

Figure 58 *- Inclusion rate spreads between MODIS and StarFM for different tolerances ("In shadow" pixels)*

3.3 MODIS v. Kustas algorithm

Before looking at the results, an observation of the starting conditions should be conducted. Kustas algorithm works on a linear or parabolic fitting of LST-to-NDVI data, and the goodness of these fittings can be important for the efficiency of the whole algorithm. For each test date, the values of two fitting statistics, R^2 and RMSE/σ, are plotted, together with a reference value for each statistic gathered by [Kustas et al, 2003] in the last column. While the former is most optimal the closer it is to 1 (by its own definition), the other is considered favourably if lower than 0.5.

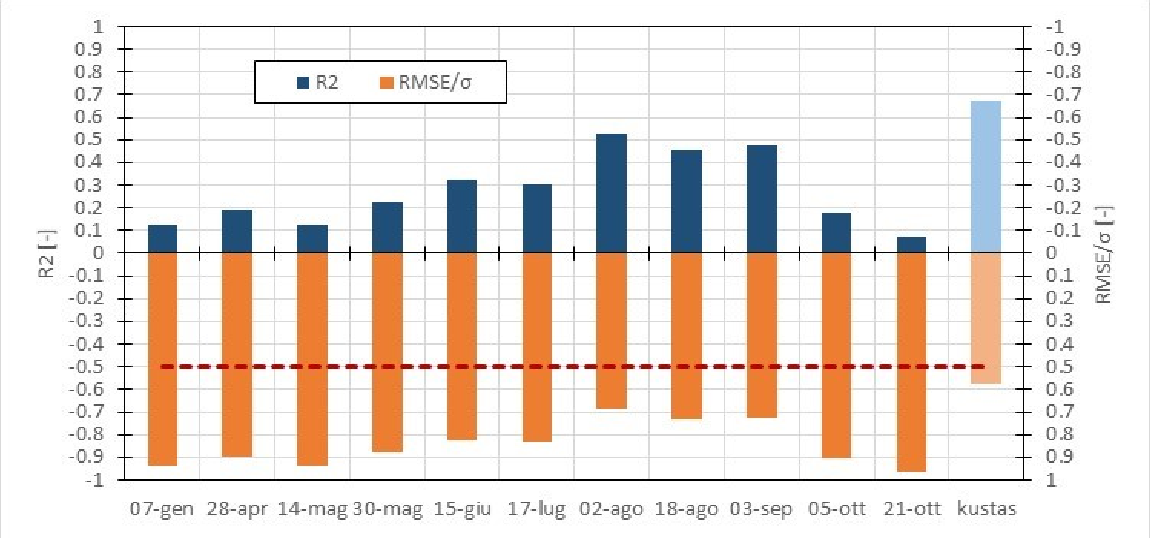

Figure 59 *- Comparison between the fitting statistics of the test dates and an average values for the ones found in Kustas et al, 2003*

Unfortunately, the fittings do not seem too close to the actual values: only August to September data pass the (R^2=0.3) value; these dates are of course also the ones with the lowest RMSE/σ value (0.68 at best, on 2nd Aug). Obviously, these numbers do not say anything final about the application of this method, but any bad result could be partly traced back to them.

The particular structure of LANDSAT 7 data (with the data gaps caused by the SLC failure) creates some problems during re-sampling. Many a cell is lost in the process, and the data sample on which every statistical analysis in this study is performed is less numerous than the ones for MODIS and StarFM. In particular, on average, "data" cells in these sources are 1.5 times more than for Kustas. A particularly "poor" date, due to an unfortunate combination of cells already missing in the LANDSAT image and cloud cover, is 3rd Sep, for which the difference between the data samples almost reaches one full order of magnitude.

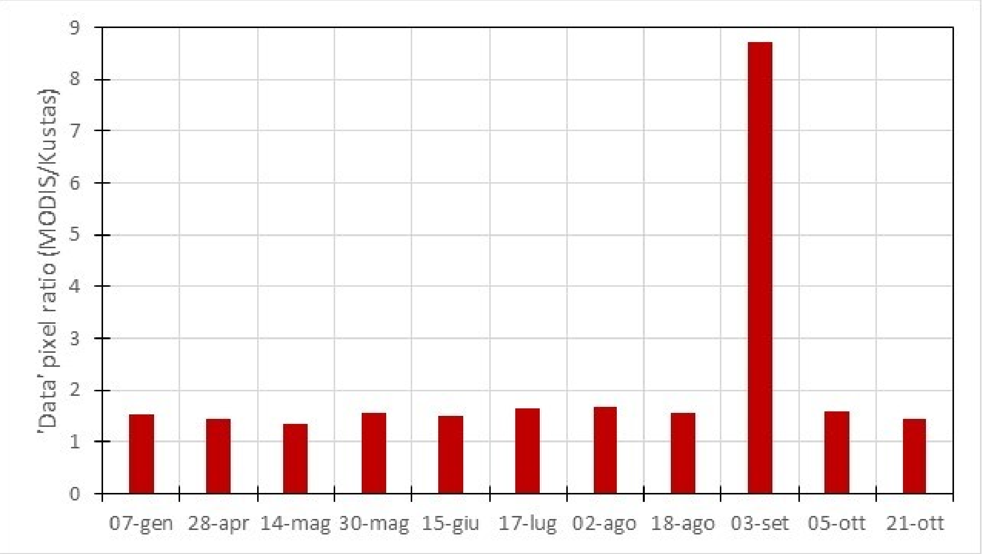

Figure 60 *- Ratios between the number of "Data" pixels in MODIS and the one in Kustas for each test date*

3.3.1 General comparison

Looking at the actual results (in the form of the usual mean error and RMSE statistics), they seem quite similar to MODIS', with a systematically positive mean error and RMSE at its worst between July and August. The former means that also Kustas' algorithm overestimates, on average, the temperatures, while once again no connection to cloud cover can be traced, with the same principles applied for MODIS.

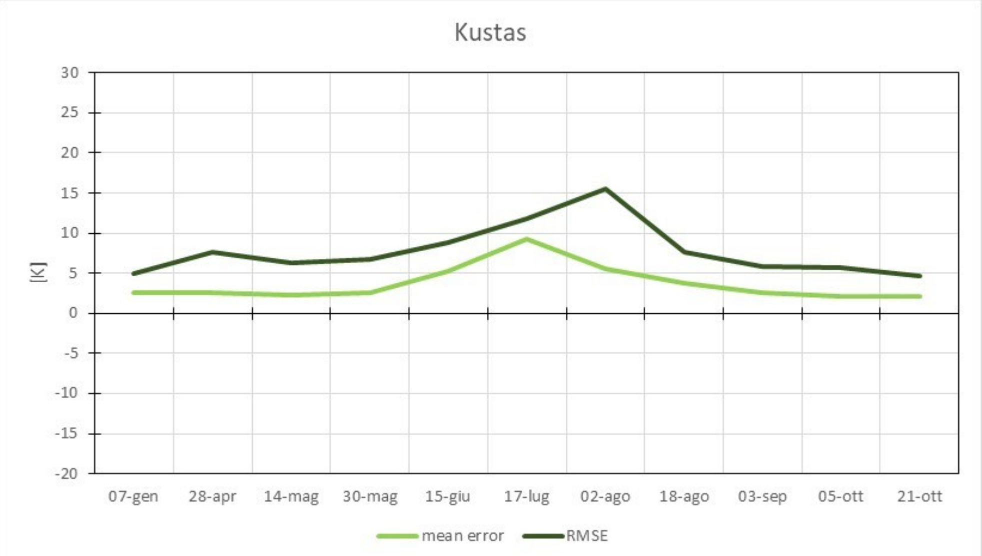

Figure 61 *- Mean error and RMSE for Kustas*

The parallel with MODIS' result is quite striking: the results are similar in numbers (the average RMSE of Kustas' algorithm is 3.26 K, compared with 3.37 K from MODIS' data) but not in trends. Indeed, looking at inclusion rates (of MODIS and Kustas), a particularly low performance is registered on 17th Jul; this is surrounded by relatively poor performances, with $\rho_{4K}<50\%$ from 30th May to 3rd Sep. This period is coarsely coincident with the flowering and growth of the vegetation, to which Kustas' algorithm is strongly linked (through the NDVI). The fitting parameters had foreshadowed a poor interpretation of the growth patterns by the algorithm; at a first guess, this could be one cause for such a pattern in the inclusion rates. The land cover analyses could provide more critical information in this sense.

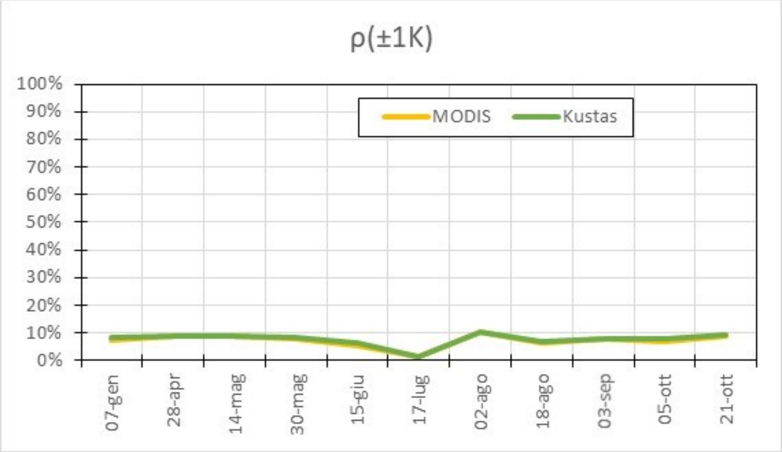

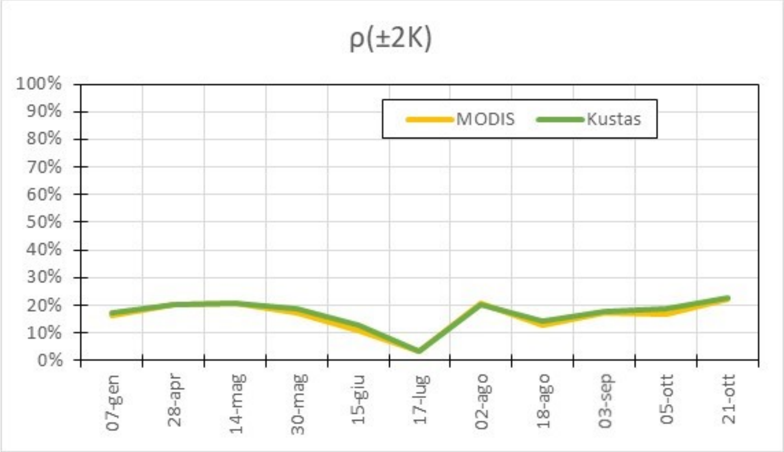

Figure 62 *- Inclusion rates for MODIS and Kustas*

Aggregating the data seasonally, the periods with the most vegetation presence (spring and summer) show the worst performance for the algorithm, similarly to MODIS. The seasonal inclusion rate show a quite consistent similarity between the two sources, with practically identical behaviours and spreads that, in the "worst" case, do not reach even +5%.

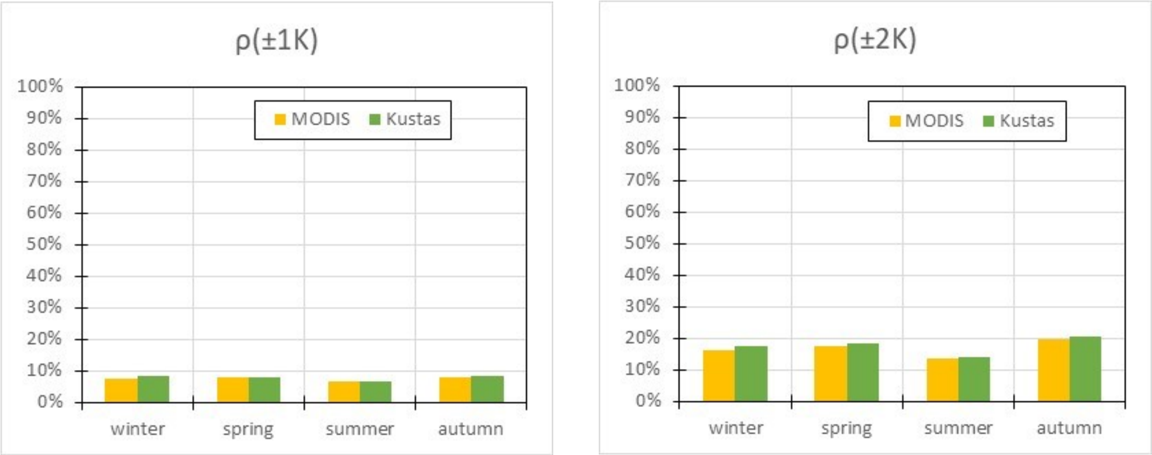

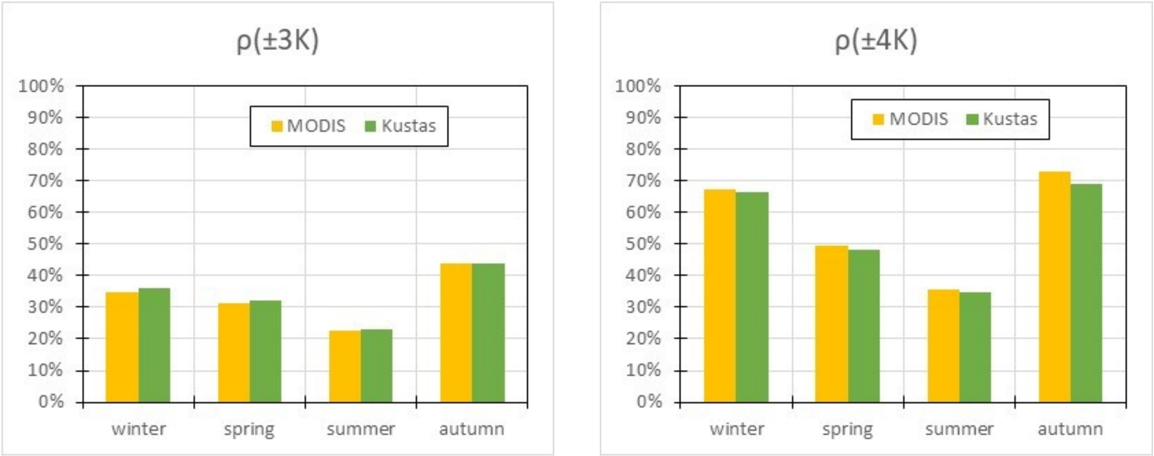

Figure 63 *- Seasonally grouped Inclusion rates for MODIS and Kustas*

3.3.2 Analysis by land cover

3.3.2.1 Croplands

Looking at the inclusion rates, they show the same general trend of the global basin, with both MODIS and Kustas underperforming in the central months of the year.

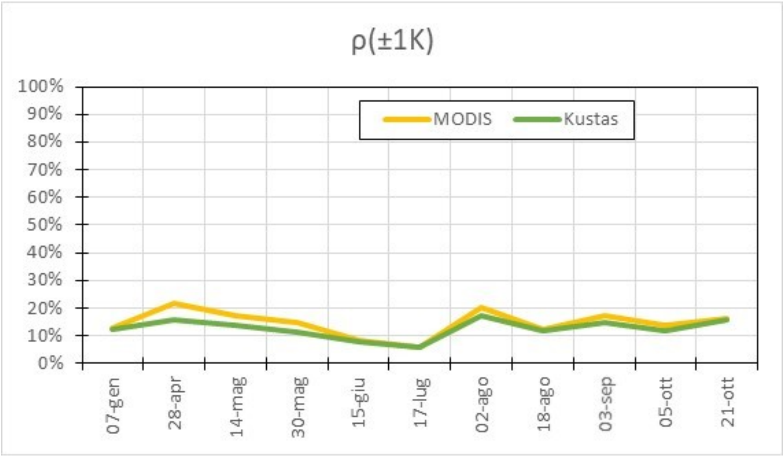

Figure 64 *- Inclusion rates for MODIS and Kustas (croplands)*

Grouping the data seasonally, the slight underperformance of Kustas' algorithm with respect to MODIS is clear and quite constant throughout the year, growing with respect to the whole-basin comparison.

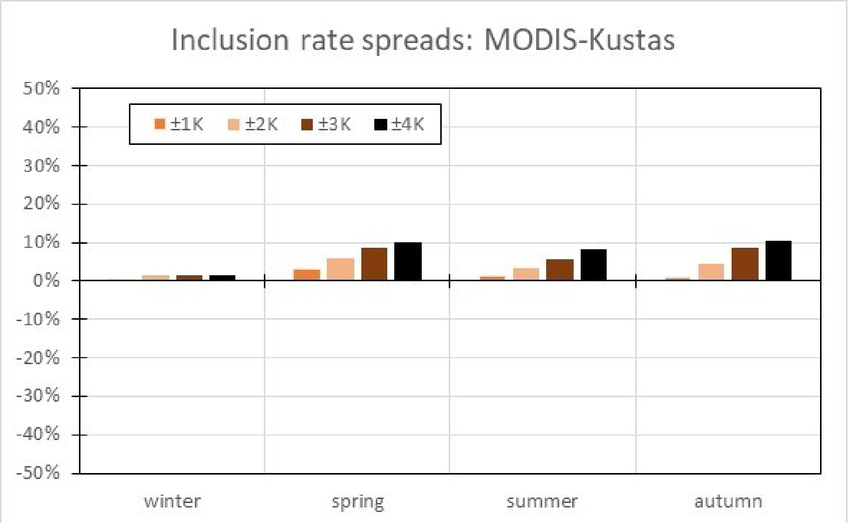

Figure 65 *- Inclusion rate spreads between MODIS and Kustas for different tolerances*

This consistent pattern means that Kustas' underperformance is not linked to the growing patterns of the vegetation; in particular, this means that both Kustas and MODIS seem to structure their work on the same mechanisms: maybe, Kustas' "less populous" data pool allows low-quality data to have a bigger influence on the overall RMSE and inclusion rates.

This is also consistent with Kustas' own average increase in RMSE when extracting crop-fields data from the whole basin, which is far higher (+21.1%) than MODIS' (+8.3%) but also of StarFM (+9.2%); this could mean that numerosity of the sample is quite important.

3.3.2.2 Forests

The close link with the preceding category can be easily seen in the inclusion rates: the inclusion rate plots are quite alike, even though the differences between MODIS and Kustas are less evident than it was for the croplands category.

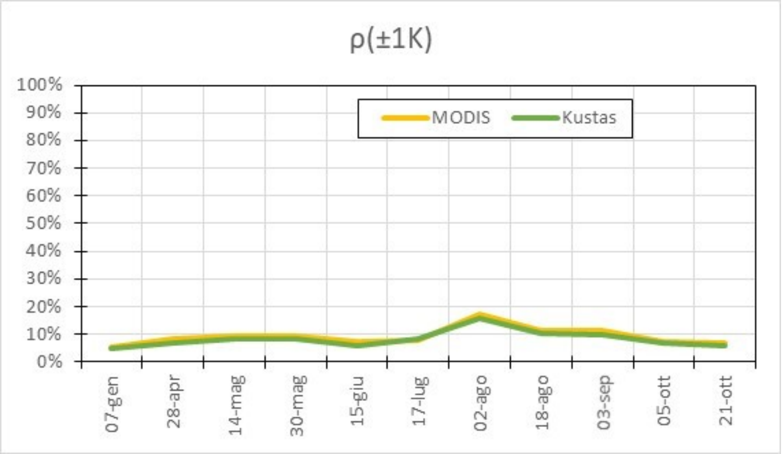

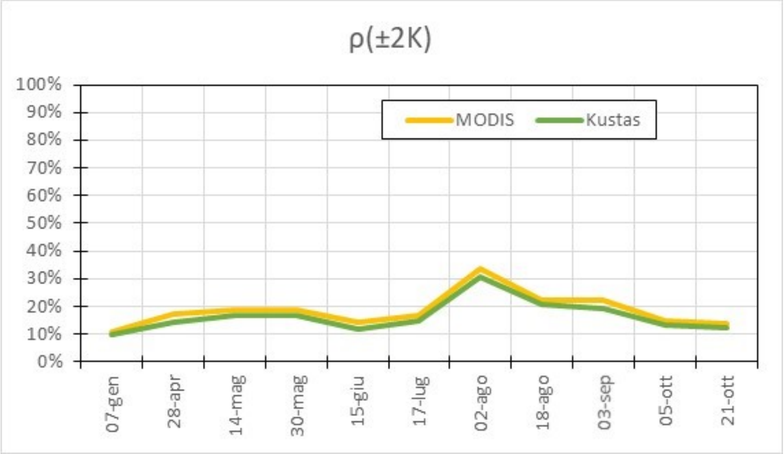

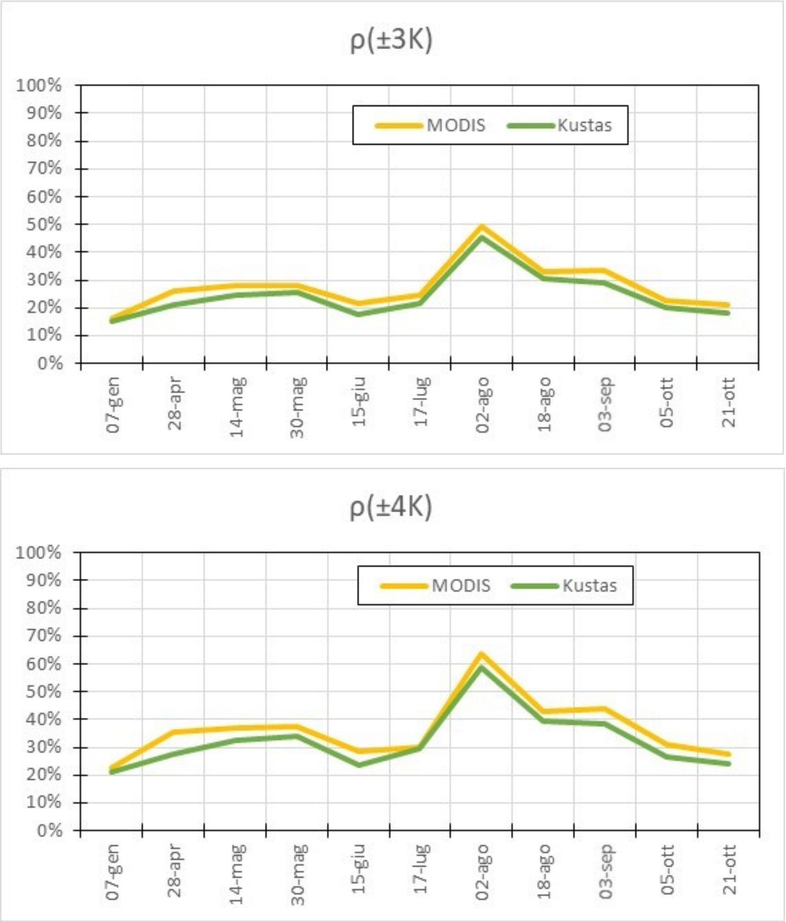

Figure 66 *- Inclusion rate patterns for MODIS and Kustas (forests)*

Looking at seasonal values, the similarity is evident: the inclusion rate spreads do not overcome the 5% threshold, meaning a closer result than for the croplands category.

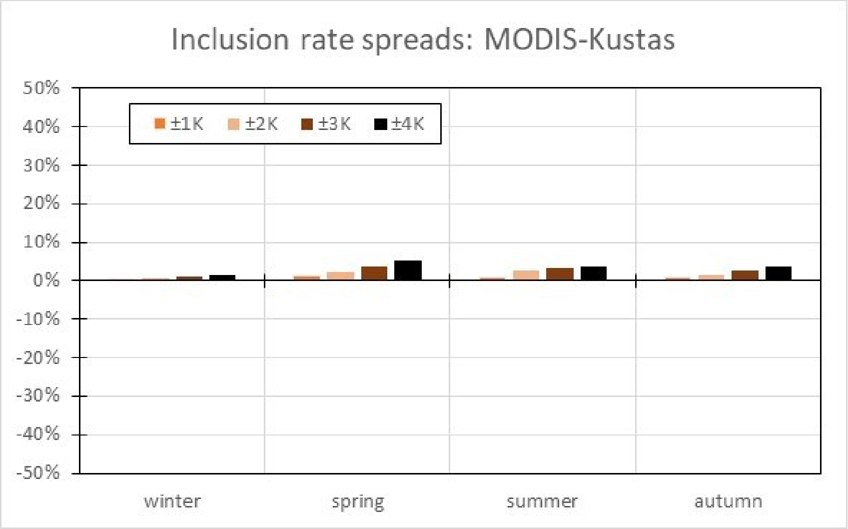

Figure 67 *- Inclusion rate spreads between MODIS and Kustas for different tolerances (forests)*

3.3.2.3 Shrubs

Inclusion rates patterns for Kustas' algorithm follow MODIS' once again, although for both the performance dip on 17th July seems a more isolated episode, as the inclusion rates ρ_{4K} for the other dates all gravitate around 50%.

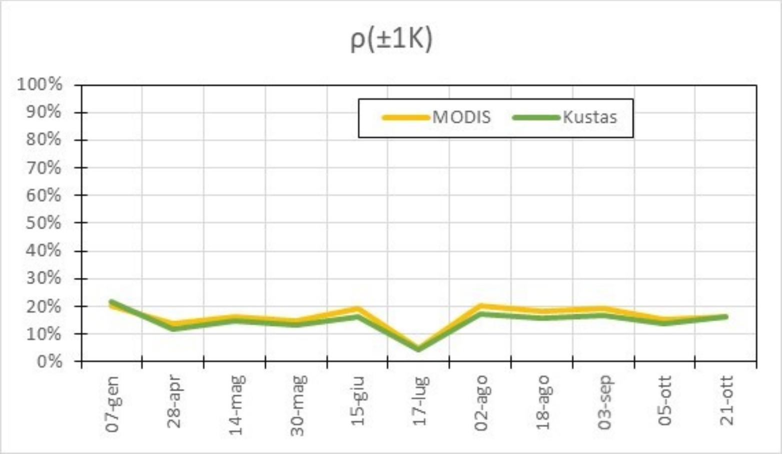

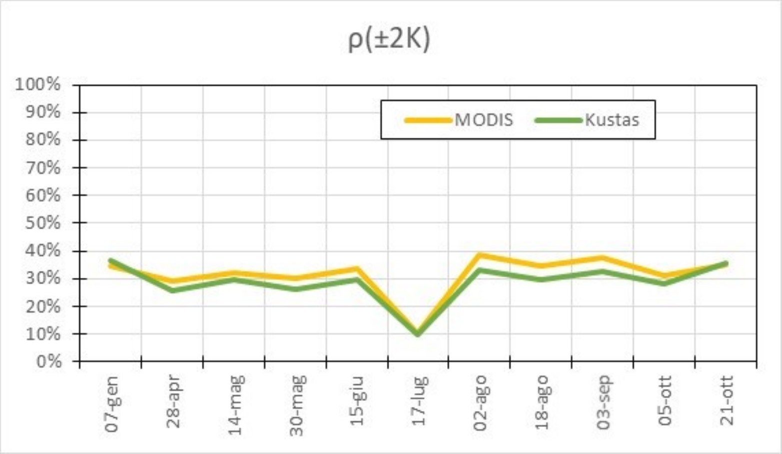

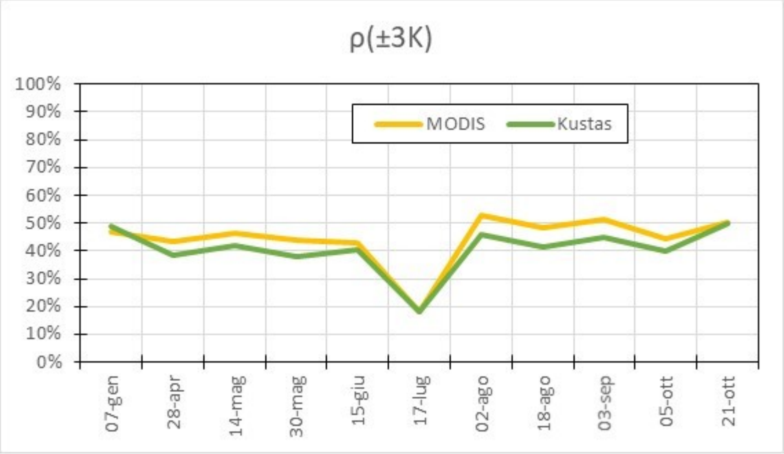

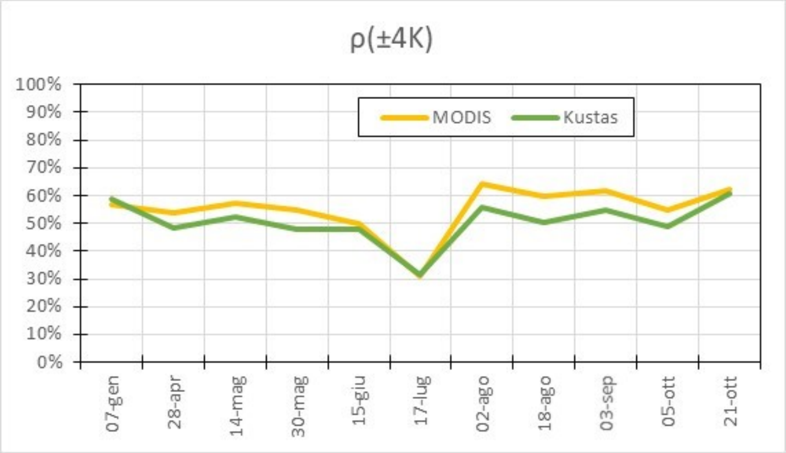

Figure 68 *- Inclusion rates for MODIS and Kustas (shrubs)*

The underperformance of Kustas, once again, is quite little (always less than 5% difference in the inclusion rate), meaning that vegetated areas, as a whole (the first three categories) are better interpreted by MODIS than Kustas, but only by a slight margin.

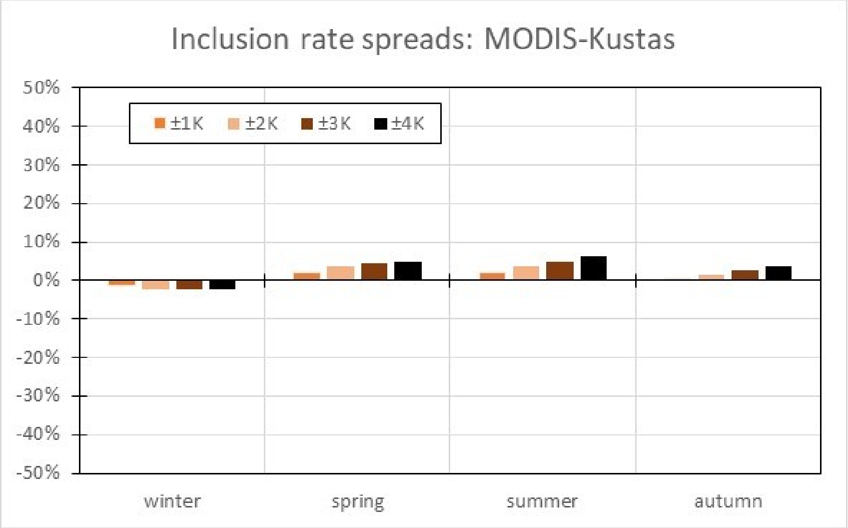

Figure 69 *- Inclusion rate spreads between MODIS and Kustas for different tolerances (shrubs)*

3.3.2.4 Deserts

Inclusion rates show the dominant trend of the basin: low values for the middle of the year (June to August period), higher values at the start and the end of the year.

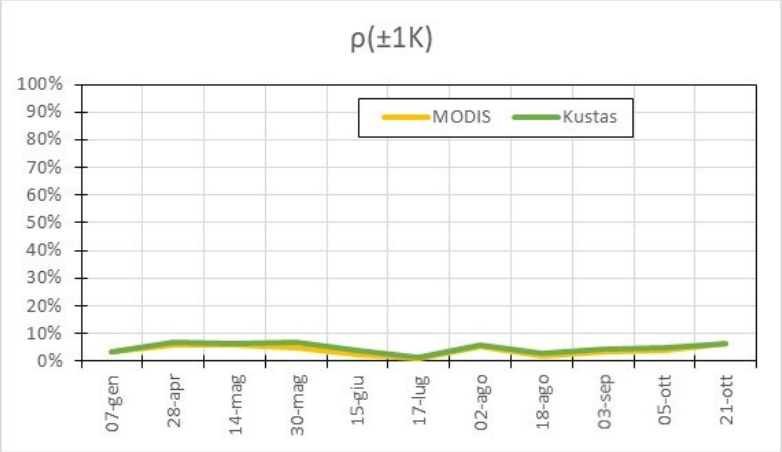

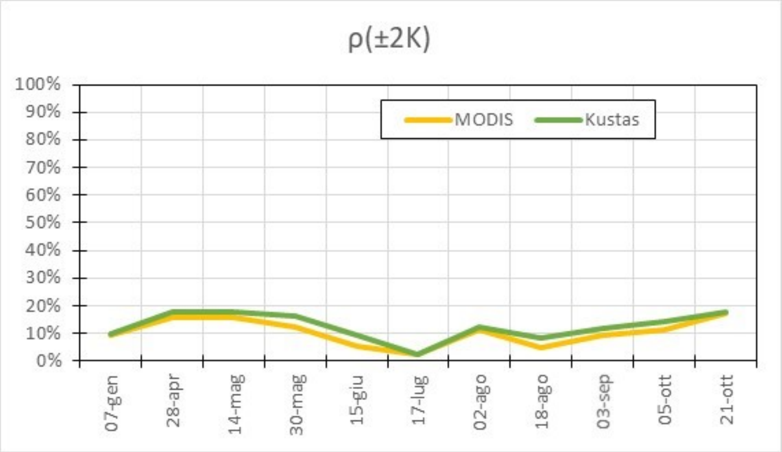

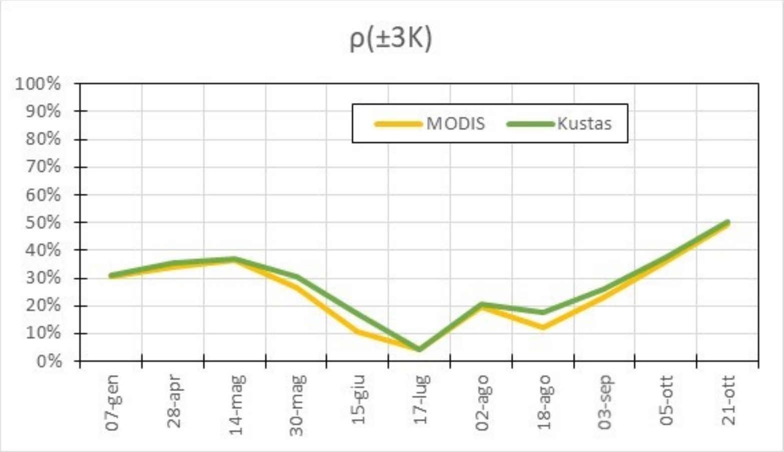

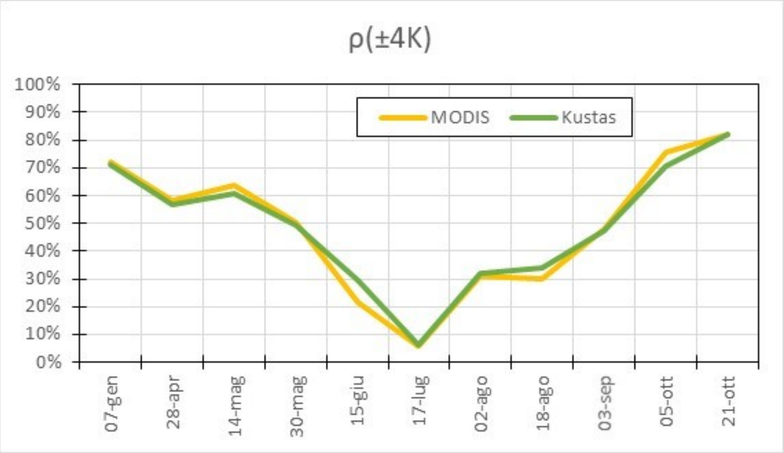

Figure 70 *- Inclusion rates for MODIS and Kustas (desert)*

Furthermore, the spreads are even smaller than for other categories. The (quasi-)absence of vegetation reduces the differences between the two methods, almost nullifying them. In some cases Kustas even outperforms MODIS, as their difference is so small that any little detail can shift the balance of the single inclusion rate spread in favour of MODIS or Kustas.

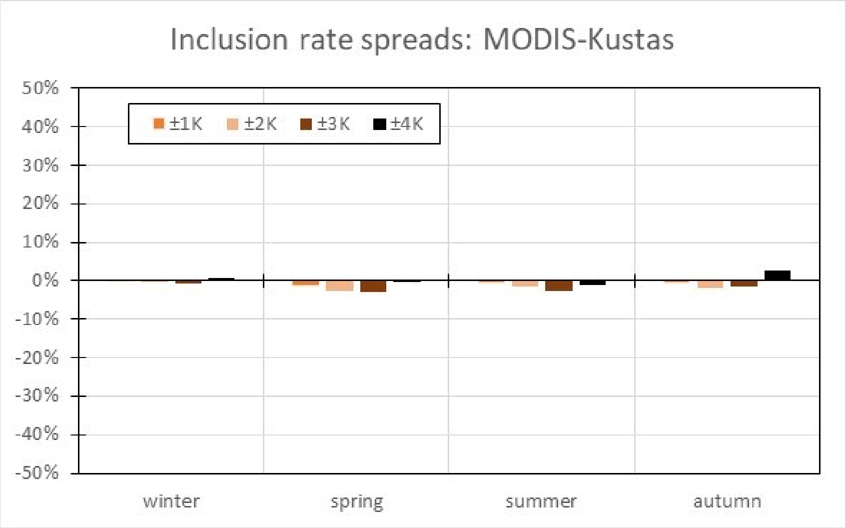

Figure 71 *- Inclusion rate spreads between MODIS and Kustas for different tolerances (desert)*

3.3.3 Analysis by illumination degree

For Kustas, just as for MODIS, shadowed pixels show worse quality, with far higher errors (-0.85% decrease in RMSE for “in-light” pixels and +49.1% increase for “in-shadow”). Removing them, a decrease of the total RMSE is obtained, but because of the “light” pixels outnumbering the “dark” ones, this benefit is rarely valuable. All things said about MODIS’ data characteristics in Section 3.3.4 is fully applicable to Kustas’ data, with no actual difference.

3.4 Conclusions on the comparison

As a result of this analysis, MODIS data have been chosen for the calibration process. The StarFM algorithm is fairly outperformed by MODIS, and Kustas offers little advantages, given that the procedure to obtain first the NDVI and then the fitting parameters is far more time-consuming than obtaining the LST data from MODIS. Land cover results suggest that the vegetated areas will be represented less accurately than the desert areas, and lighting-degree analysis yields that no useful advantage can come in excluding shadowed pixels.

3.5 LSTs image comparison

In this section LST maps are compared for three example dates (30th May, 18th August and 5th October 2012). Each date will feature the four scenes (Landsat, MODIS, Kustas and StarFM) and a frequency plot.

3.5.1 30th May 2012

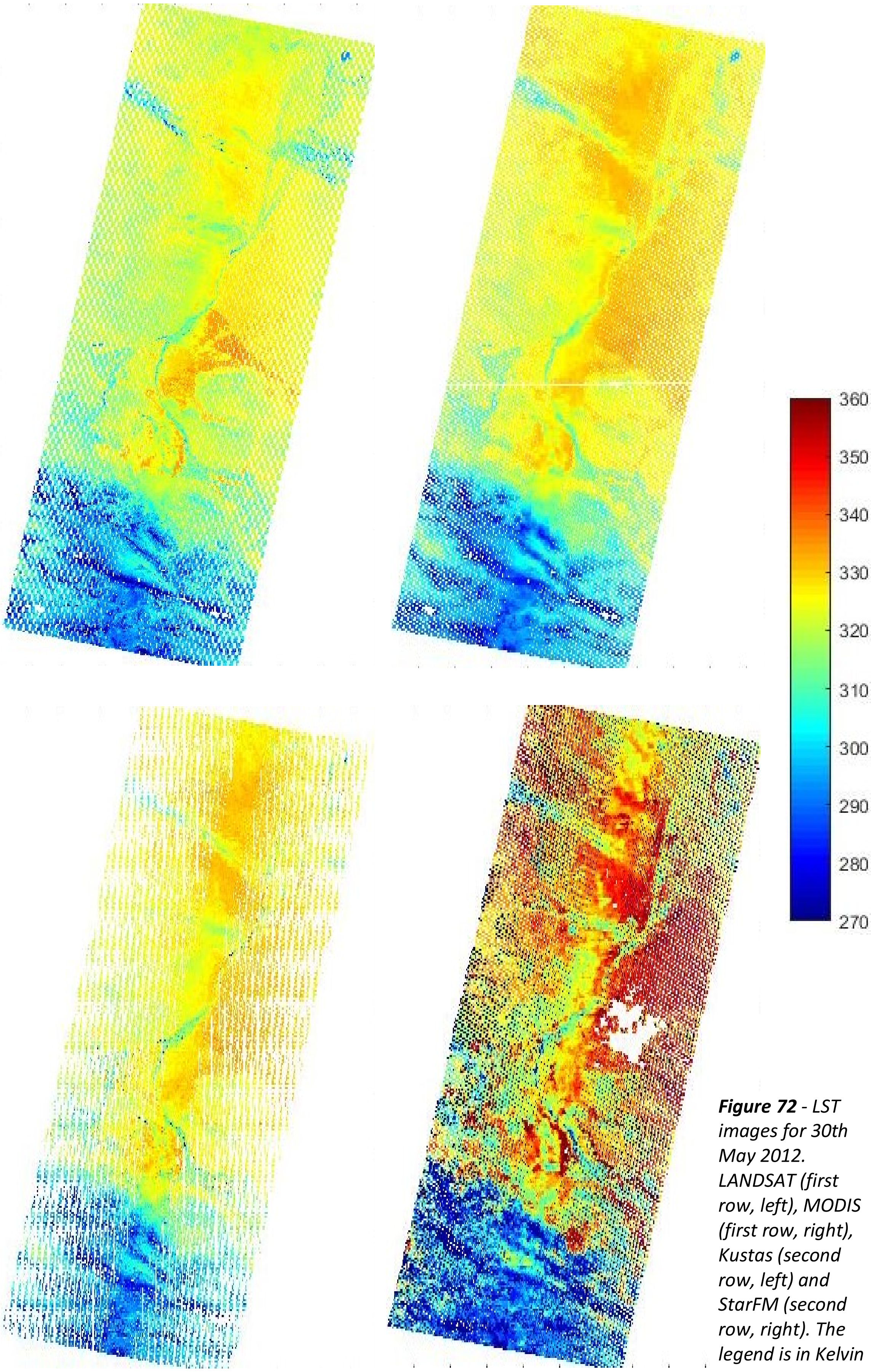

Figure 72 *- LST images for 30th May 2012. LANDSAT (first row, left), MODIS (first row, right), Kustas (second row, left) and StarFM (second row, right). The legend is in Kelvin*

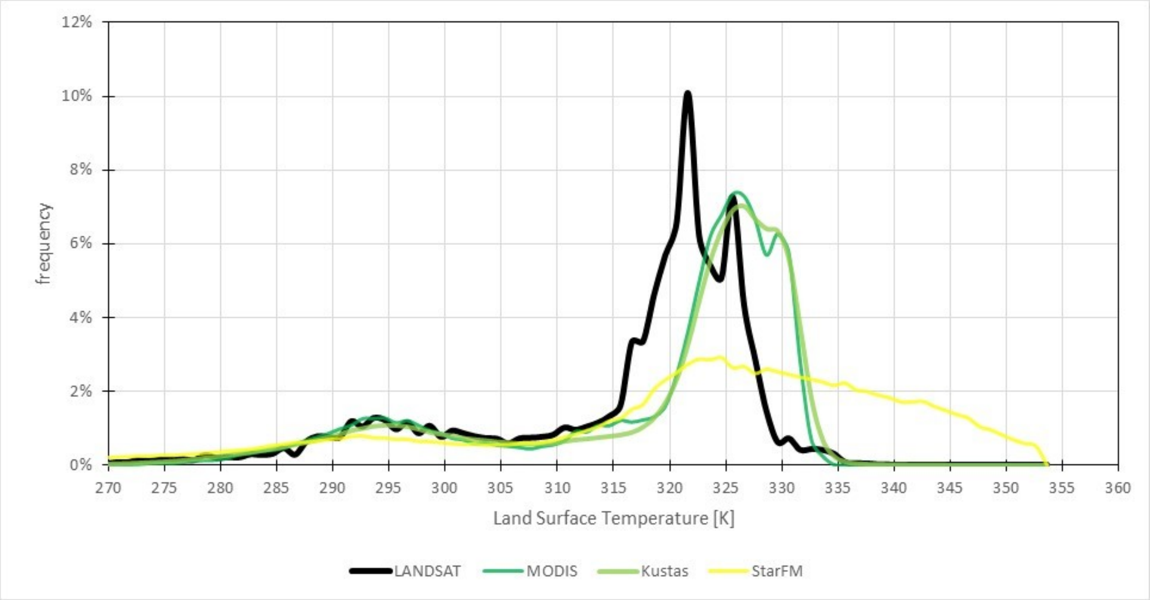

Figure 73 *- Frequency plot for LANDSAT, MODIS, Kustas and StarFM on 30th May*

For this date, all sources overestimate LANDSAT's temperature. MODIS, for example, has a good interpretation of the cold mountain areas, but "sees" higher temperatures in the desert area. Although less visible because of the numerous 'NoData' cells, Kustas follows in this path, as witnessed by the frequency plot: the bias between MODIS/Kustas and LANDSAT is quite clear. MODIS, however, manages to interpret, in part, the shape of LANDSAT's frequency plot. StarFM has a wider range of temperatures, adapting well to the "tail" of the plot in the colder temperatures but coarsely overestimating the desert zone.

3.5.2 18th August 2012

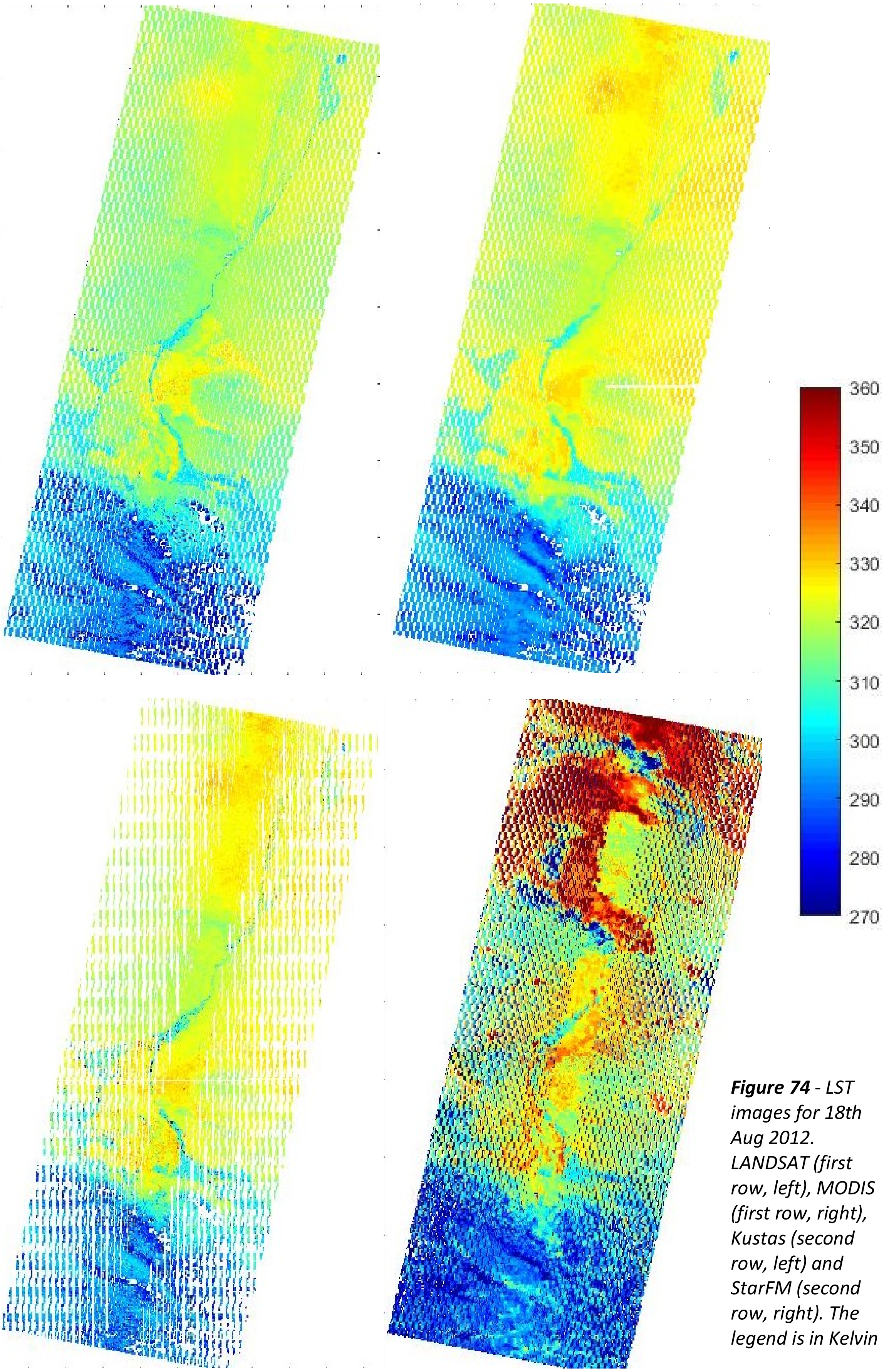

Figure 74 *- LST images for 18th Aug 2012. LANDSAT (first row, left), MODIS (first row, right), Kustas (second row, left) and StarFM (second row, right). The legend is in Kelvin*

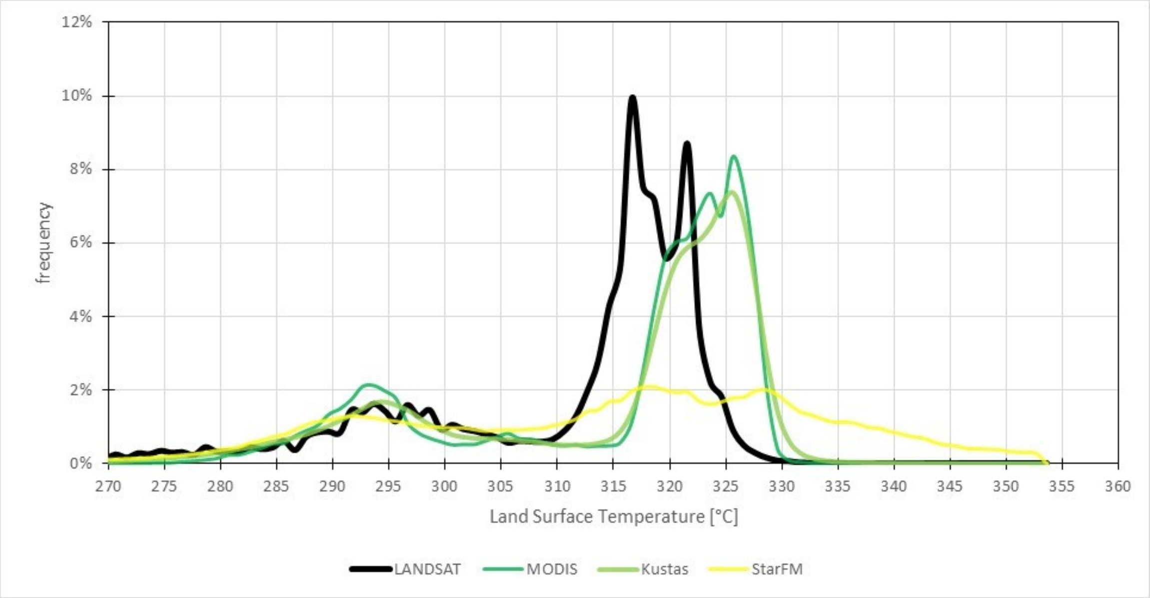

Figure 75 *- Frequency plot for LANDSAT, MODIS, Kustas and StarFM on 18th Aug*

Both the response from the temperature maps and the frequency plot are not much different from the ones of the preceding date. MODIS results the best interpretation of the temperature, with Kustas a close second. StarFM behaves well for the low temperatures but markedly misses the temperature pattern in the warmer areas.

3.5.3 5th October 2012

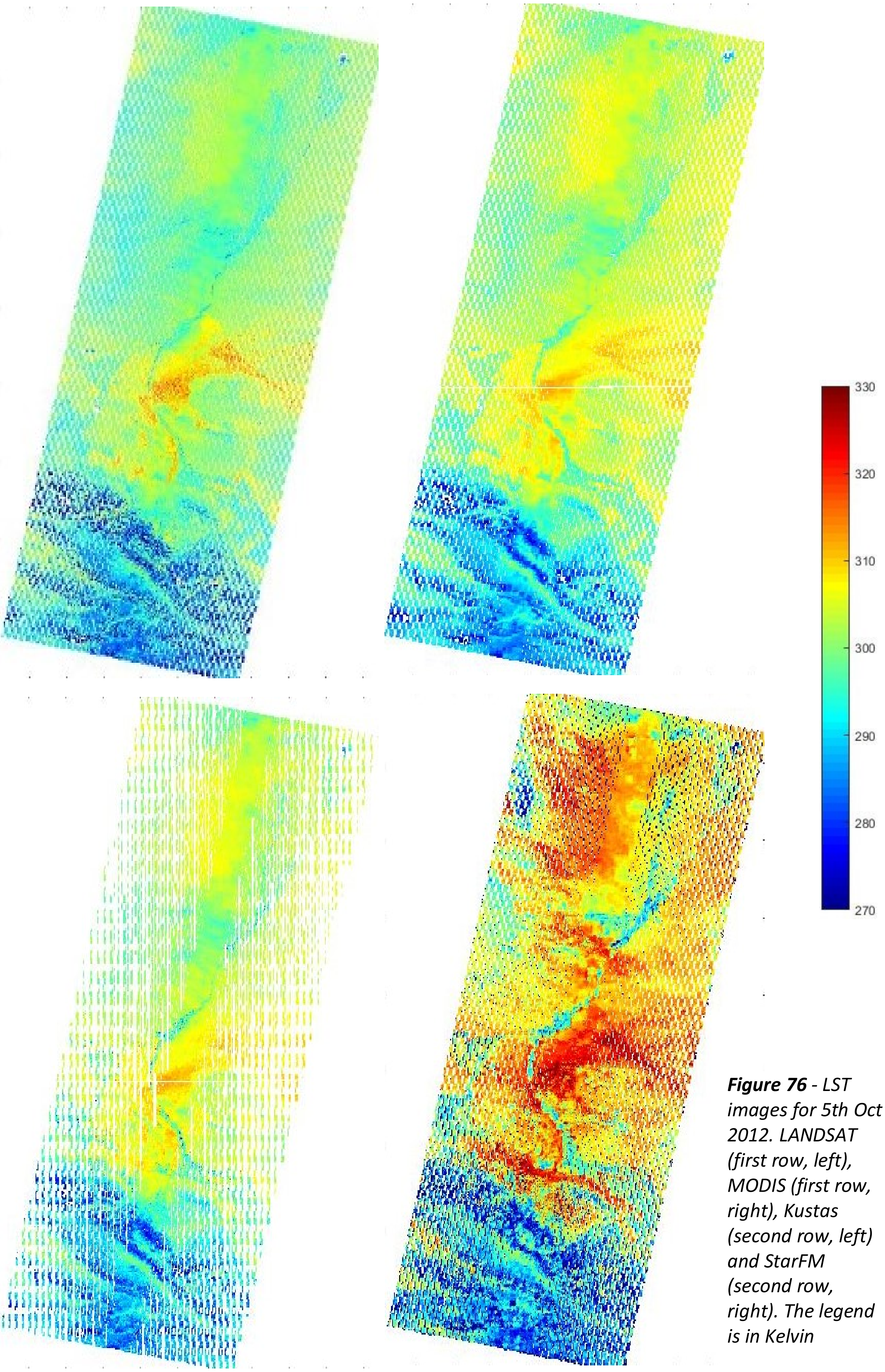

Figure 76 *- LST images for 5th Oct 2012. LANDSAT (first row, left), MODIS (first row, right), Kustas (second row, left) and StarFM (second row, right). The legend is in Kelvin*

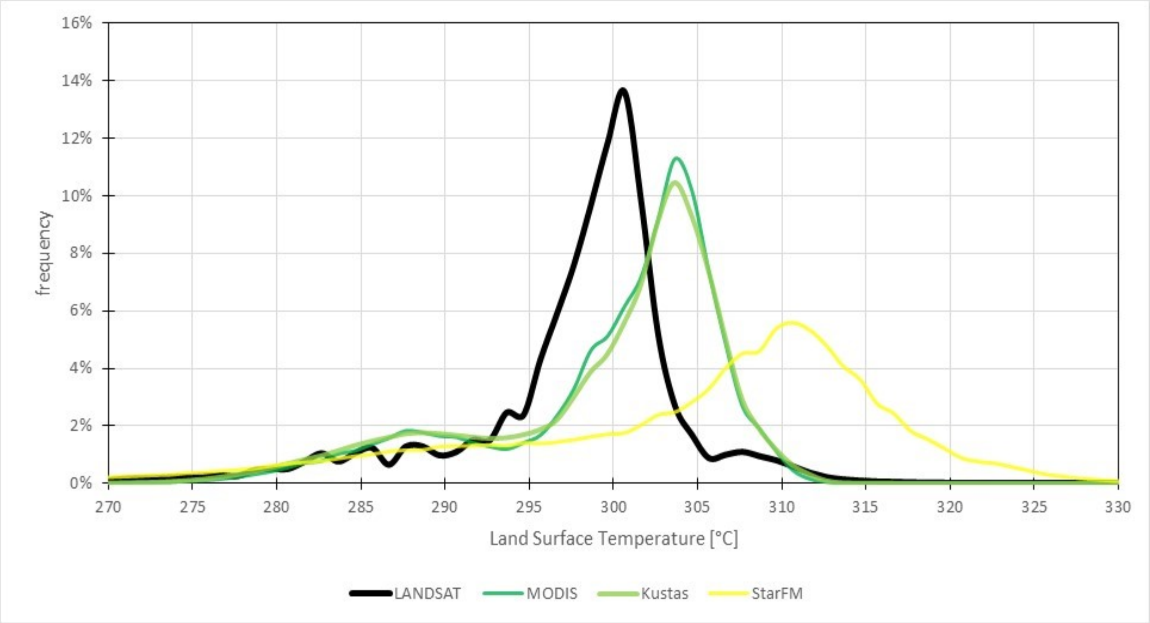

Figure 77 *- Frequency plots for LANDSAT, MODIS, Kustas and StarFM on 5th Oct 2012*

In this last date the plot is simpler, with only one peak. Both MODIS and Kustas do a good job, probably with the lowest bias of these three examples dates (more or less a couple of °C). StarFM displays a good plot shape, but still has too much variety (with a resulting "low" peak) and a more important bias (around 10°C).

Chapter 4

Model calibration

In Section 1, the calibration methodology is stated. The results are then listed in Sections 2-5: Section 2 reports the general results; Section 3 delves into the actual calibration statistics; Section 4 displays some temperature maps before and after calibration; finally, Section 5 relates the "evolution" of the calibration parameters throughout the different simulations.

4.1 Methodology

Calibration is a process in which a model is adapted to the particular characteristics of the situation of interest. The so called "calibration variable" is an output of the model in question, which is compared to actually measured values. The calibration consists in modifying progressively a number of input parameters so that the output of the model resembles the measured values more and more at each run of the model. For this purpose, 67 measurements of LST in year 2012 have been selected, choosing the dates with the least cloud cover (less than 5%) in order to have the best data quality of the whole year.

Each new simulation features a new set of values. For the first stage of calibration, four parameters have been selected: Brooks-Corey Index ("bc"), soil depth ("depth"), hydraulic conductivity at saturation ("ksat") and minimum stomatal resistance ("rsmin"). While the first three parameters directly influence the amount of water in soil, the last one is more directly linked to the transpiration process and the heat absorption by the vegetation and thus can influence only areas with a consistent vegetation presence. These four parameters have been selected based on sensitivity studies performed in the past on the model [Corbari-Mancini et al, 2015] [Corbari-Mancini, 2014].

The calibration method follows these steps:

(1) From Simulation-0, RET values are gathered for the whole basin for the 67 selected dates and at a time as close as possible to MODIS' sampling time (*circa* midday local time)
(2) For each pixel of the basin, the average temperature difference between modelled and measured data is stored in one single matrix
(3) According to the error measured for each pixel, some or all of the four calibration parameters are modified
(4) A new simulation is performed, and the cycle starts again

The main advantage of this type of calibration is its spatial variability: most calibration procedures apply the same variation to the whole basin, while in this case the variation of the single parameter depends on the local difference between estimated and measured temperature. In such a case, pixels already well-interpreting the LST will not be changed much in their soil and vegetation parameters, and the "arbitrary" change in the parameter will be performed only where required.

This procedure cannot go on indefinitely, but requires the calibration variables to stay within physically-justified extremes. This, for example, means that the hydraulic conductivity at saturation could never reach values as high as 1 m/s (highly-loose gravel) or as low as 10^{-12} m/s (concrete, [Schneider et al, 2012]).

Another constraint to the process is the coherence of the hydrological balance of the model: the possible imbalance between inputs and outputs needs to be within acceptable values. In particular, two mass balances will be checked:

$$\begin{cases} Weather\ input = Net\ prec. + Absorption - Net\ Dunnian\ prec. + Snowstored\ water \\ Absoprtion = Deep\ perolation + Evapotranspiration + \Delta W \end{cases}$$

The first equation ("at-surface" mass balance) checks the balance between the cumulated results of the model: looking at ground level, the weather inputs can either be absorbed by the soil or stored as snow, according to the air and surface temperatures. The amount of water that does not fit in these categories is the actual net precipitation. The last contribution is the "dunnian" net precipitation: according to Dunn's model [Dunn, 1999], it is the amount of water that resurfaces from the ground once the soil is saturated.

The second equation ("in-soil" mass balance) checks the water mass balance within the soil itself: what in the first equation was generally called "absorption" is characterized as an actual enrichment of the in-soil water (ΔW), which is the net amount once the water lost to evapotranspiration and deep percolation is removed. The actual increase/decrease in soil moisture can be found by calculating the difference between the final and initial soil moistures, actualized over the average soil depth of the basin.

Finally, in order to check whether the calibration process is going in the right "direction", at the end of every simulation a number of statistics will be gathered about the final LST output of the model (FEST) against the calibration data (MODIS):

- Absolute average error (err_{abs}) $err_{abs} = \frac{\sum_{i=1}^{n_{basin}} |MODIS_i - FEST_i|}{n_{basin}}$
- Average error (err) $err = \frac{\sum_{i=1}^{n_{basin}} (MODIS_i - FEST_i)}{n_{basin}}$
- Root Mean Square Error (RMSE) $RMSE = \sqrt{\frac{\sum_{i=1}^{n_{basin}} |MODIS_i - FEST_i|^2}{n_{basin}}}$
- Average relative error (ε) $\varepsilon = \left(\sum_{i=1}^{n_{basin}} \frac{MODIS_i - FEST_i}{MODIS_i}\right) / n_{basin}$
- Nash-Sutcliffe Efficiency (NSE) $NSE = 1 - \frac{\sum_{i=1}^{n_{basin}} (MODIS_i - FEST_i)^2}{\sum_{i=1}^{n_{basin}} (MODIS_i - Tmedia_{MODIS})^2}$
- Average bias $bias = Tmedia_{MODIS} - Tmedia_{FEST}$

These are just some of a wide range of statistical indexes to describe the results. Of these, the RMSE, the NSE and the average bias are the most helpful to understand if the calibration has increased in any way the accuracy of the results.

4.2 Calibration scheme and first results

The first calibration stage has required 3 renewals of the parameters, and the following table recaps the terminology for the following sub-sections.

Simulation	Parameters change	RMSE		NSE		Bias	
Sim-0	Starting parameters	7.67°C	-	0.067	-	-2.88°C	-
Sim-1	Higher depth, lower ksat bc rsmin	7.18°C	-6.3%	0.167	+12.1%	-2.38°C	-0.44°C
Sim-2	Lowered rsmin	7.15°C	-0.5%	0.171	+0.9%	-2.35°C	-0.47°C
Sim-3	Increased depth	6.94°C	-2.5%	0.215	+4.7%	-1.81°C	-0.95°C

Each parameter change is referred to the previous simulation, and thus means a further alteration. The displayed statistics are averages for the 67 selected dates.

The table shows how, at first, the model (on average) overestimates the measured data, thus requiring calibration procedures that would decrease the forecast temperature. The mass balance check is described in the plots below. First, the at-surface mass balance, then the in-soil one.

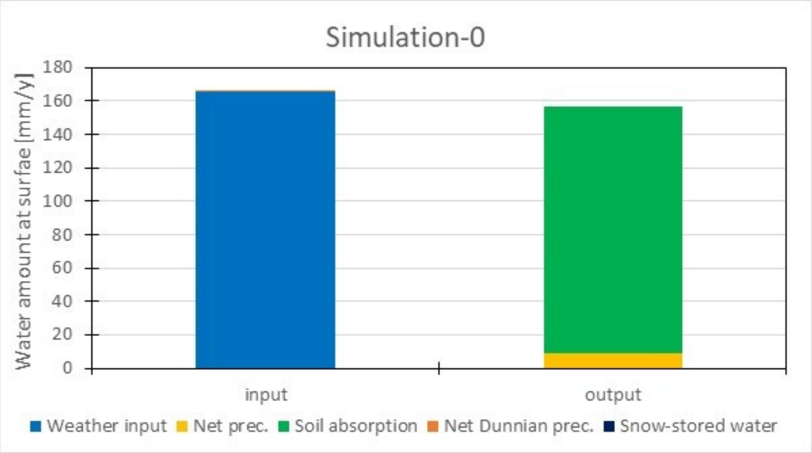

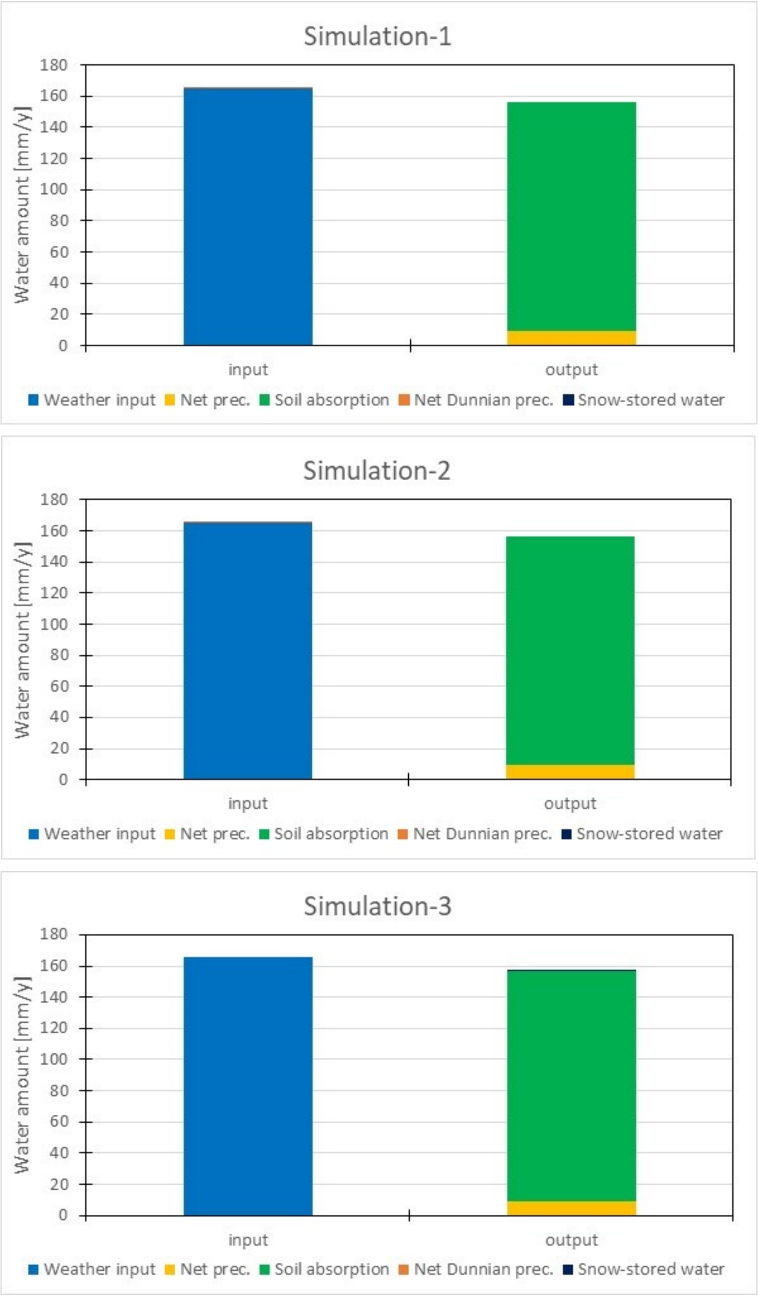

Figure 78 *- Water balances at ground level for the 4 simulations*

contributions	**Sim-0**	**Sim-1**	**Sim-2**	**Sim-3**
Weather inputs	165.42 mm	165.50 mm	165.50 mm	165.50 mm
Net precipitation	9.00 mm	9.39 mm	9.38 mm	8.98 mm
Soil absorption	147.35 mm	147.04 mm	147.05 mm	147.44 mm
Net Dunnian prec.	0.0247 mm	0.0033 mm	0.0029 mm	0.00 mm
Snow-stored water	$7.25\ 10^{-6}$ mm	$7.25\ 10^{-6}$ mm	$7.25\ 10^{-6}$ mm	$7.25\ 10^{-6}$ mm
Net balance	9.10 mm	9.08 mm	9.08 mm	9.08 mm

Table 8 *- All the elements in the water mass balance for the 4 simulations*

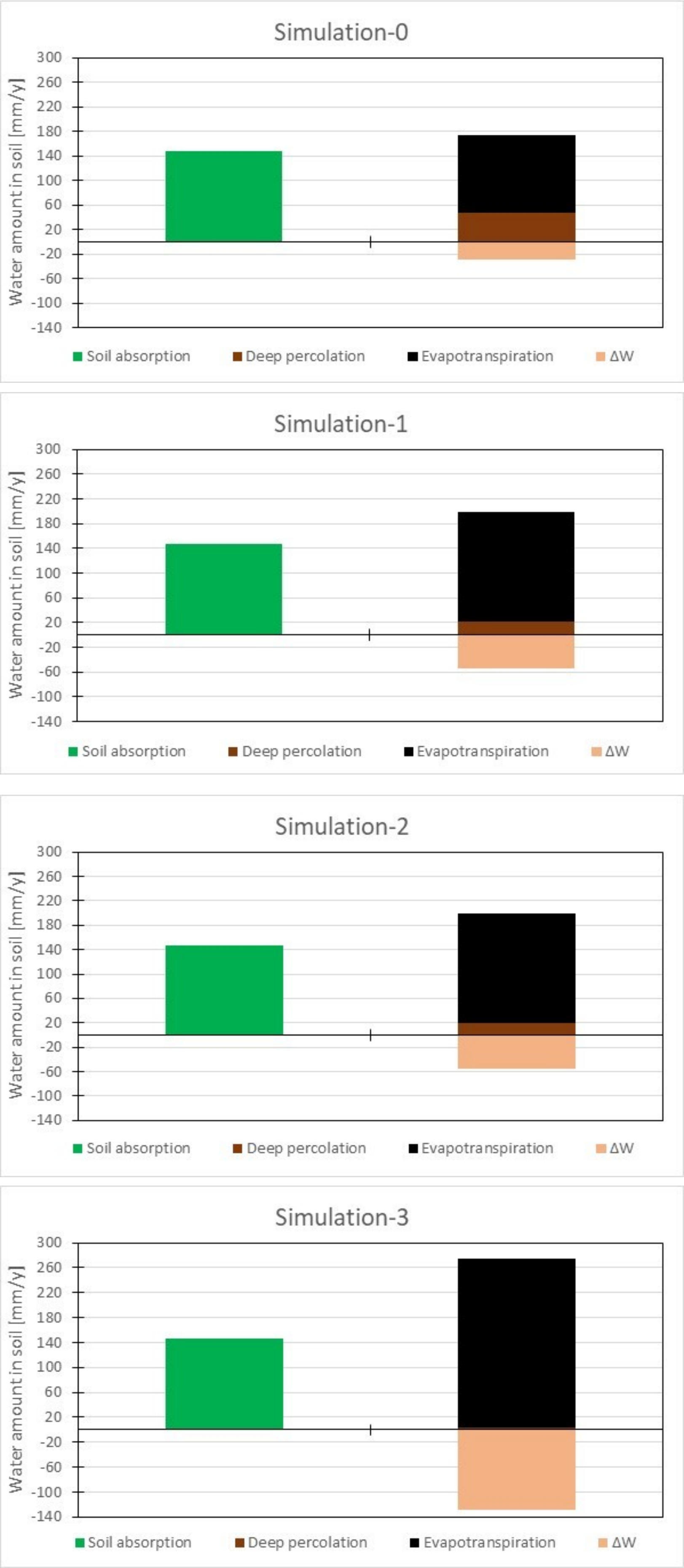

Figure 79 *- Water mass balance "below-surface", with the relative amounts for each simulation*

contributions	Sim-0	Sim-1	Sim-2	Sim-3
Soil absorption	147.35 mm	147.04 mm	147.05 mm	147.44 mm
Deep percolation	48.41 mm	21.20 mm	20.15 mm	3.81 mm
Evapotranspiration	125.54 mm	177.17 mm	179.38 mm	271.17 mm
ΔW	-28.74 mm	-53.69 mm	-54.86 mm	-127.72 mm
Net balance	2.15 mm	2.36 mm	2.38 mm	0.18 mm

Table 9 *- "Below-surface" water mass balance with its detailed amounts*

From the first plots it can be gathered that, on a basin sale, most of the meteoric water is absorbed by the soil. The effects of calibration, however, are more evident looking into the “in-soil” balance equation: most of the water is lost to evapotranspiration (as expected for a desert basin) and the net water amount is always negative, as a proof that 2012 was a warmer-than-usual year (the soil moisture at the end of the year was found lower than the value at the start).

The first calibration markedly increased evapotranspiration: the changes in *ksat*, *bc* and *depth* meant that more water was retained in the ground (and thus less was lost to deep percolation) and so was available for the evaporation process; the lowering of *rsmin* meant that water transfers between vegetation and the atmosphere (and so, transpiration) and heat absorption by the plants were increased.

The second calibration intervened on *rsmin* only, thus affecting just the vegetated part of the basin. Evapotranspiration grew even more, surely thanks to the transpiration component due to the vegetation.

The third calibration acted on the soil depth, and thus the amount of water in soil available to evaporation. The important and further increase in evapotranspiration means that in the basin potential evapotranspiration is quite high, as having more water available immediately results in more evaporation.

4.3 Statistics

The three main monitored statistics are RMSE, NSE and temperature bias at basin scale.

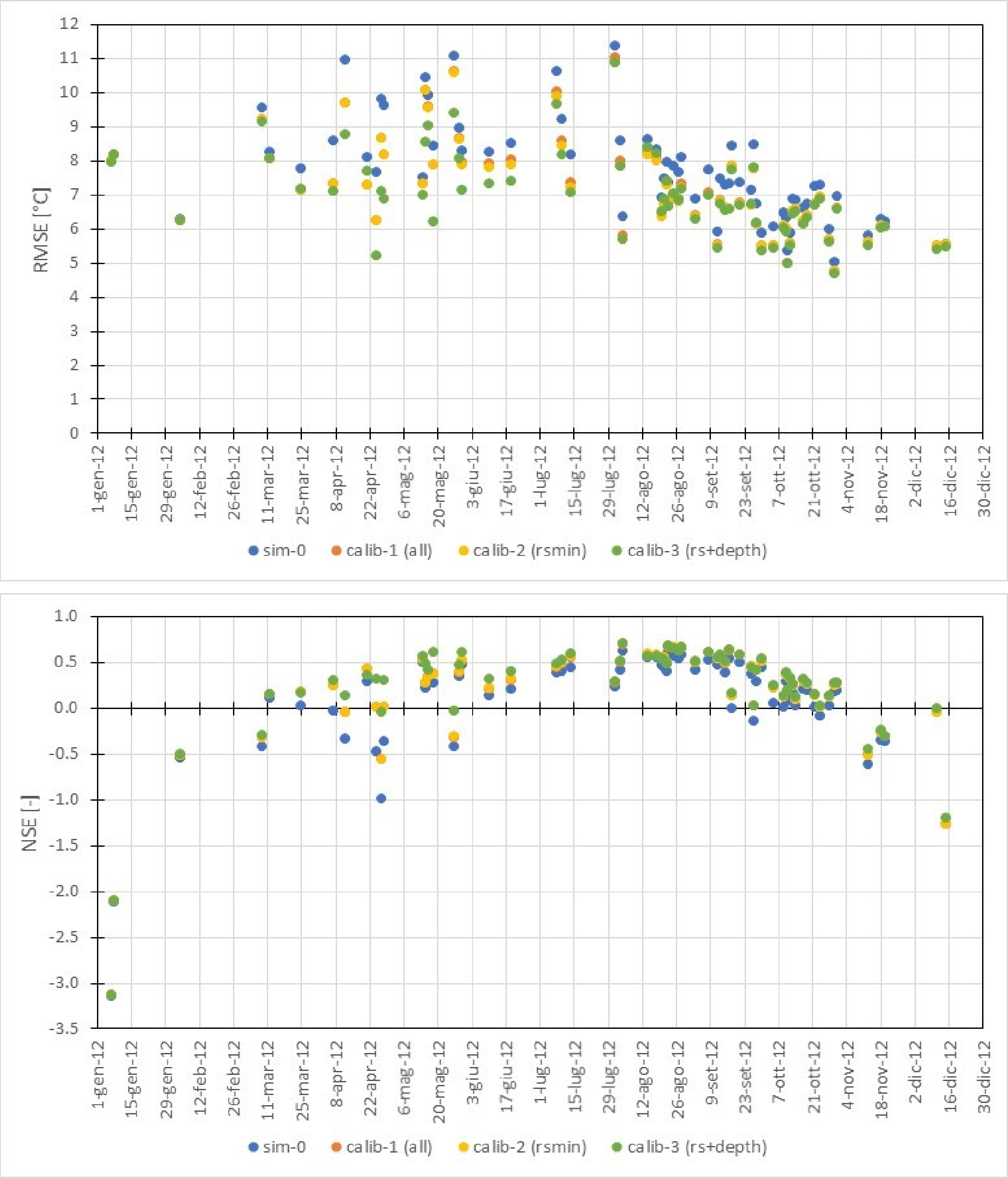

Figure 80 *- RMSE and NSE values of the model results for the different simulations*

For both parameters, the central part of the first half of the year is the one with the highest benefits from calibration. While the RMSE seems to follow a decreasing trend with the passing of the days (generally lower at the end of the year than at the start), the NSE shows a different behaviour, with higher values (quite close to the optimal +1) in the central part of the year and worse performances in the winter period. This last behaviour could be justified with the influence of snow in the water and energy transfers.

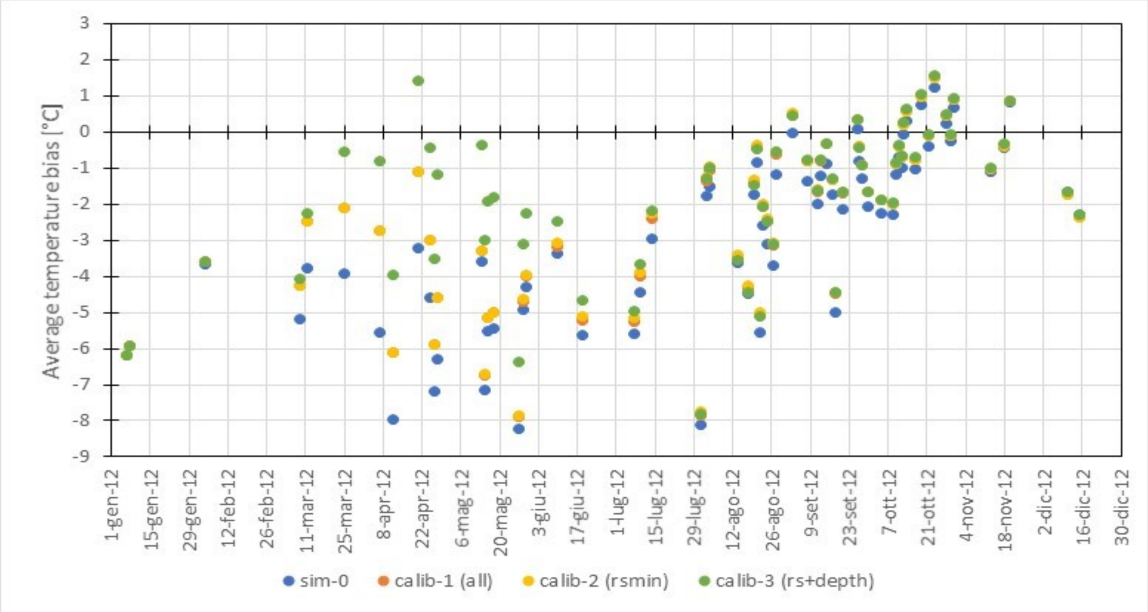

Figure 81 *- Difference between the average basin temperatures measured by MODIS and estimated by FEST-EWB*

Looking into the temperature biases at basin scale, once again the best gains can be found between March and May. Furthermore, the general trend of FEST overestimating the temperatures (reflected in the negative values of the bias), is clear and visible here.

4.4 Images

LST values are mapped for three test-dates: 7th April 2012, 14th July 2012 and 5th October 2012. For each date, MODIS (target) map is present, then the results from four different simulations are displayed; a frequency plot is also provided for all the LST maps of each example-date.

Each group of results is organized as such: on the first row, the MODIS data with the colormap; on the second, Sim-0 (left) and Sim-1 (right); on the third and last, Sim-2 (left) and Sim-3 (right).

4.4.1 7th April 2012

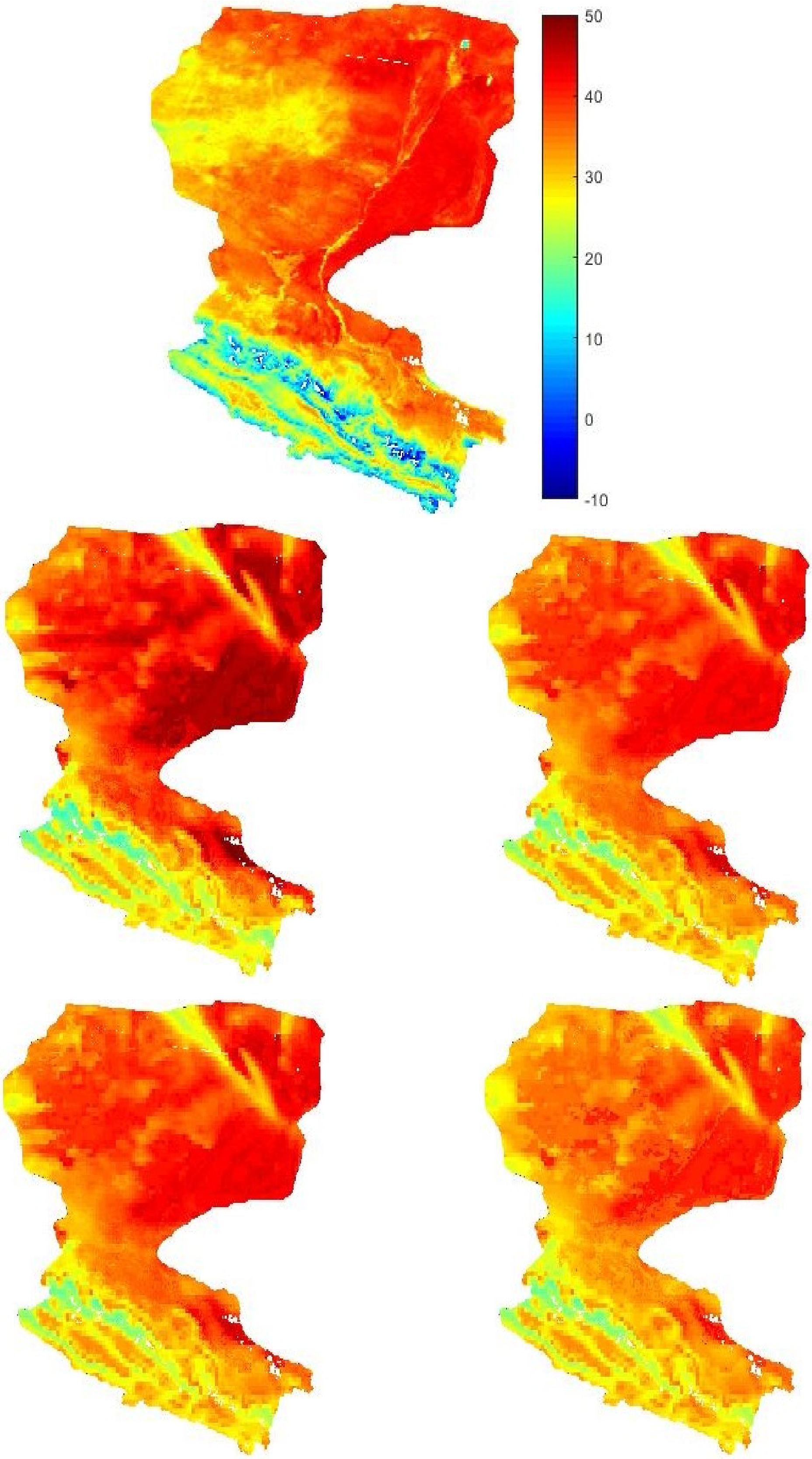

Figure 82 *- LST images on 7th Apr 2012. MODIS (target) image in the first row, with the legend in °C; Sim-0 (left) and Sim-1 (right) in the second row; Sim-2 (left) and Sim-3 (right) in the third row*

Data from the whole first half of the year seems to be more sensible to the calibration process than later one. Simulation-0 shows a consistent temperature overestimation, both in the mountain area and the eastern desert area. This is partly recovered after calibration, as can be seen from the frequency diagram: data from Simulation-1 and Simulation-2 (which appear almost overlapping, in the frequency diagram) are the ones with the best fit to MODIS' product. However, as can be seen from the maps, little progress is made in interpreting the colder temperatures of the mountainous area. The frequency diagram shows how, below 25°C, all simulations fail to emulate the MODIS diagram.

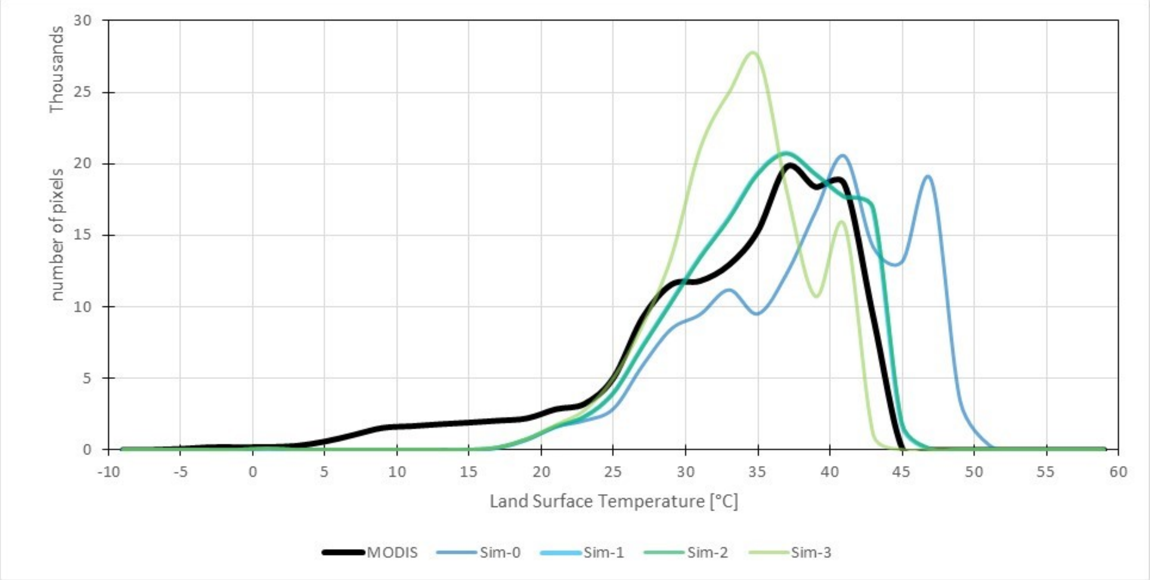

Figure 83 *- Frequency plots for MODIS, Sim-0, Sim-1, Sim-2 and Sim-3 on 7th Apr 2012*

4.4.2 14th July 2012

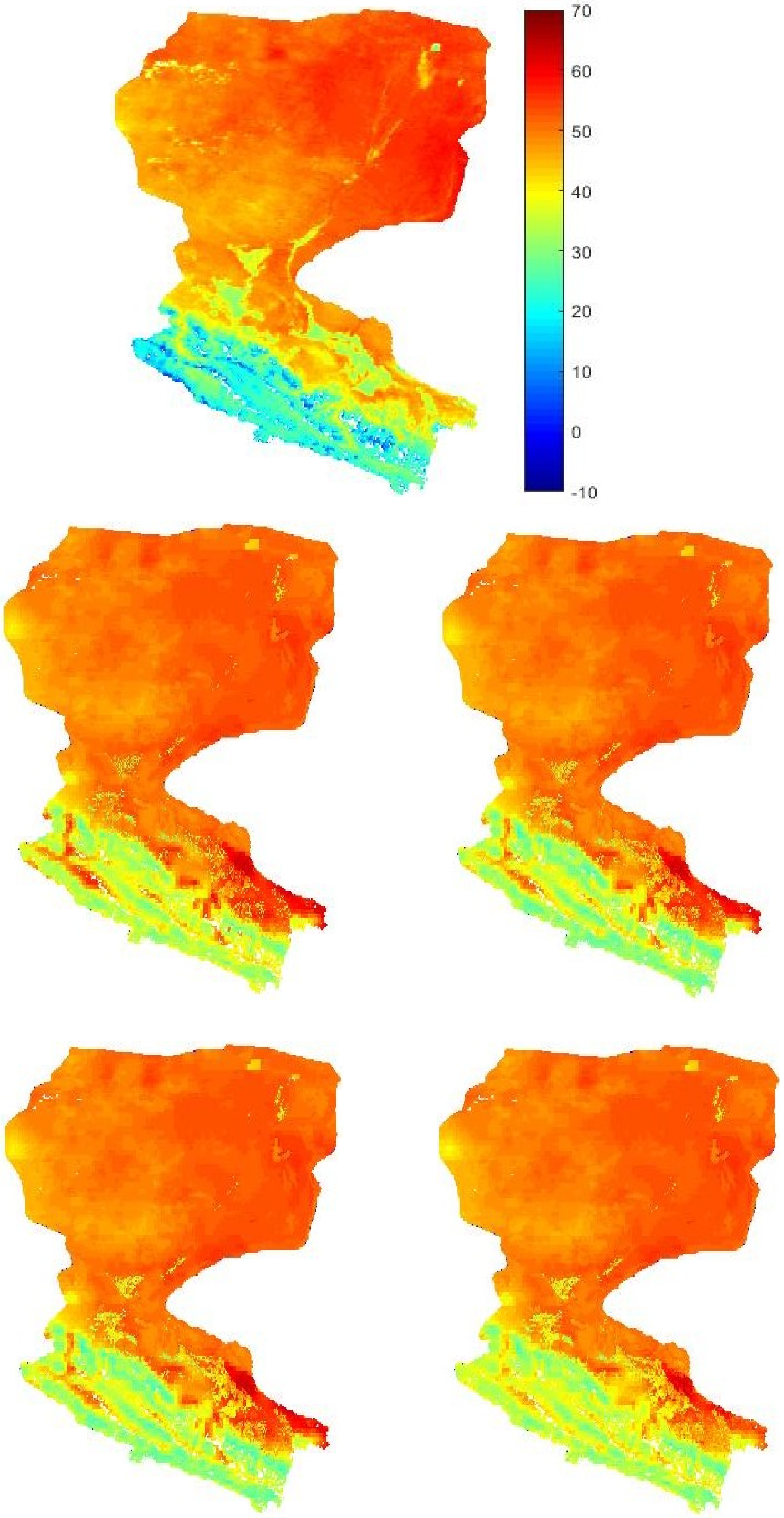

Figure 84 *- LST images on 14th Jul 2012. MODIS (target) image in the first row, with the legend in °C; Sim-0 (left) and Sim-1 (right) in the second row; Sim-2 (left) and Sim-3 (right) in the third row*

Data from this date shows less improvement: the maps before and after calibration look quite alike, as is witnessed by the frequency plots, which do not vary much. However, in this case the desert area of the basin seems well represented: the shape of the frequency plot is sufficiently alike, and the maps all seem fairly representative of the MODIS data. However, the mountainous area is still badly represented, even though the calibration progress, at least in the maps, seem to make some progress in that sense.

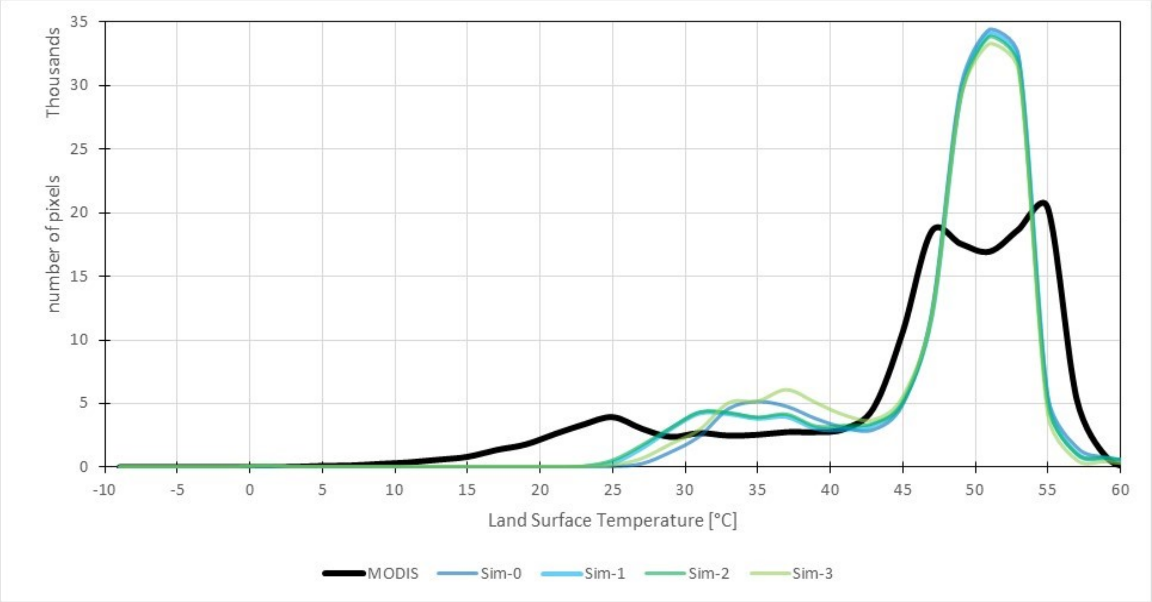

Figure 85 *- Frequency plots for MODIS, Sim-0, Sim-1, Sim-2 and Sim-3 on 14th Jul 2012*

4.4.3 5th October 2012

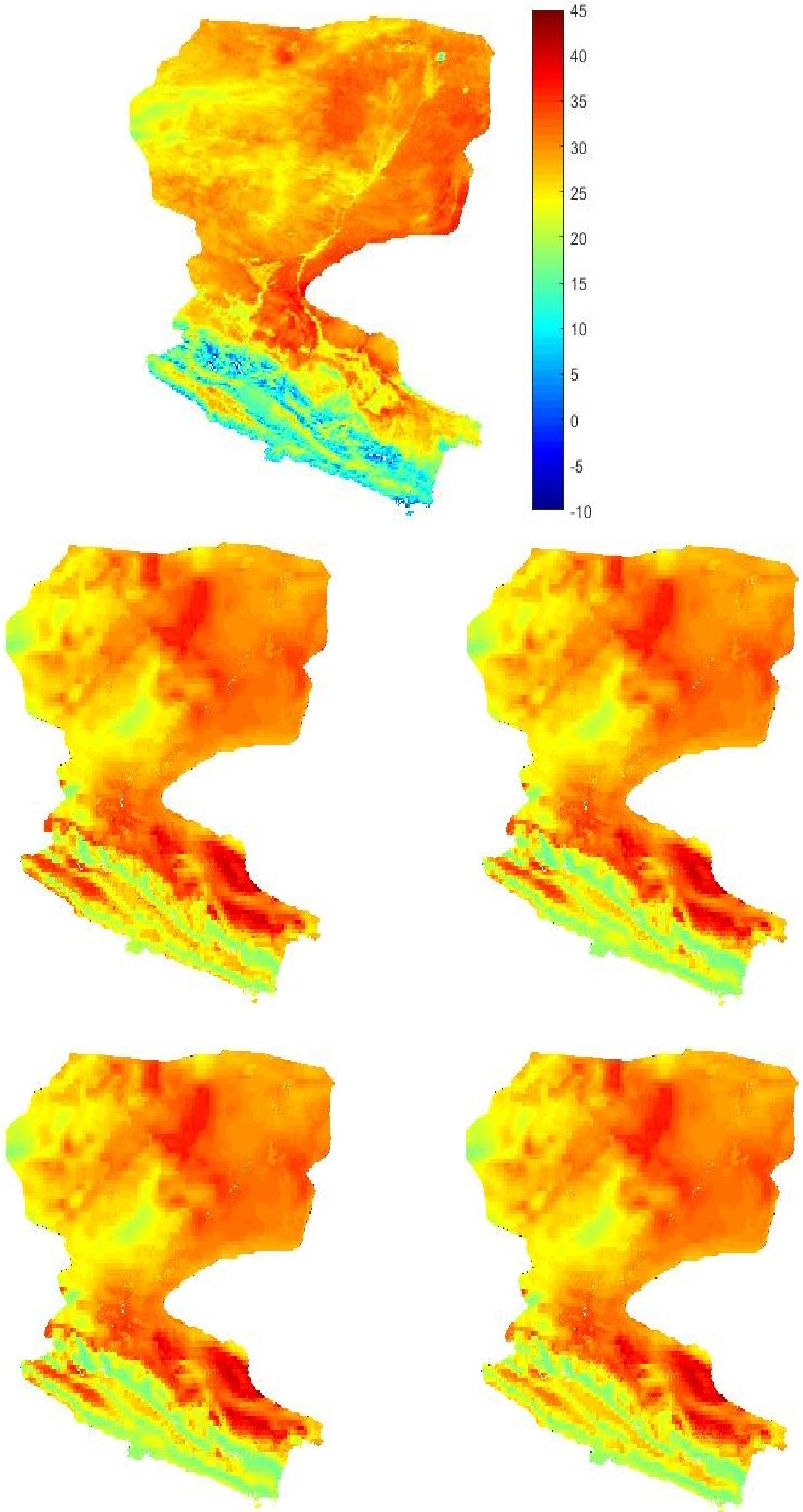

Figure 86 *- LST images on 5th Oct 2012. MODIS (target) image in the first row, with the legend in °C; Sim-0 (left) and Sim-1 (right) in the second row; Sim-2 (left) and Sim-3 (right) in the third row*

For the 5th October, the model shows less variability than the model. Overall, this may be one of the best results for the model, even without a sensible help from calibration, as testified by the frequency plots, all almost overlapping. However, the "tail" of the MODIS plot towards the lower temperatures, which accounts for the mountain area is still missed by the model, independently from calibration.

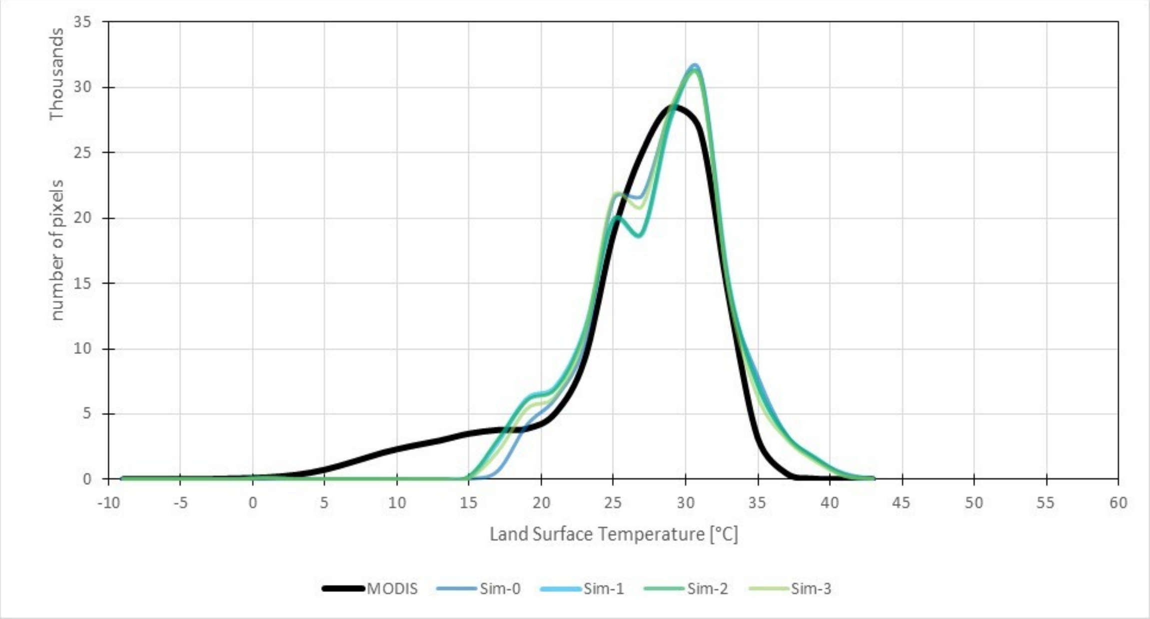

Figure 87 *- Frequency plots for MODIS, Sim-0, Sim-1, Sim-2 and Sim-3 on 5th Oct 2012*

4.5 Parameter evolution

4.5.1 Brooks-Corey Index

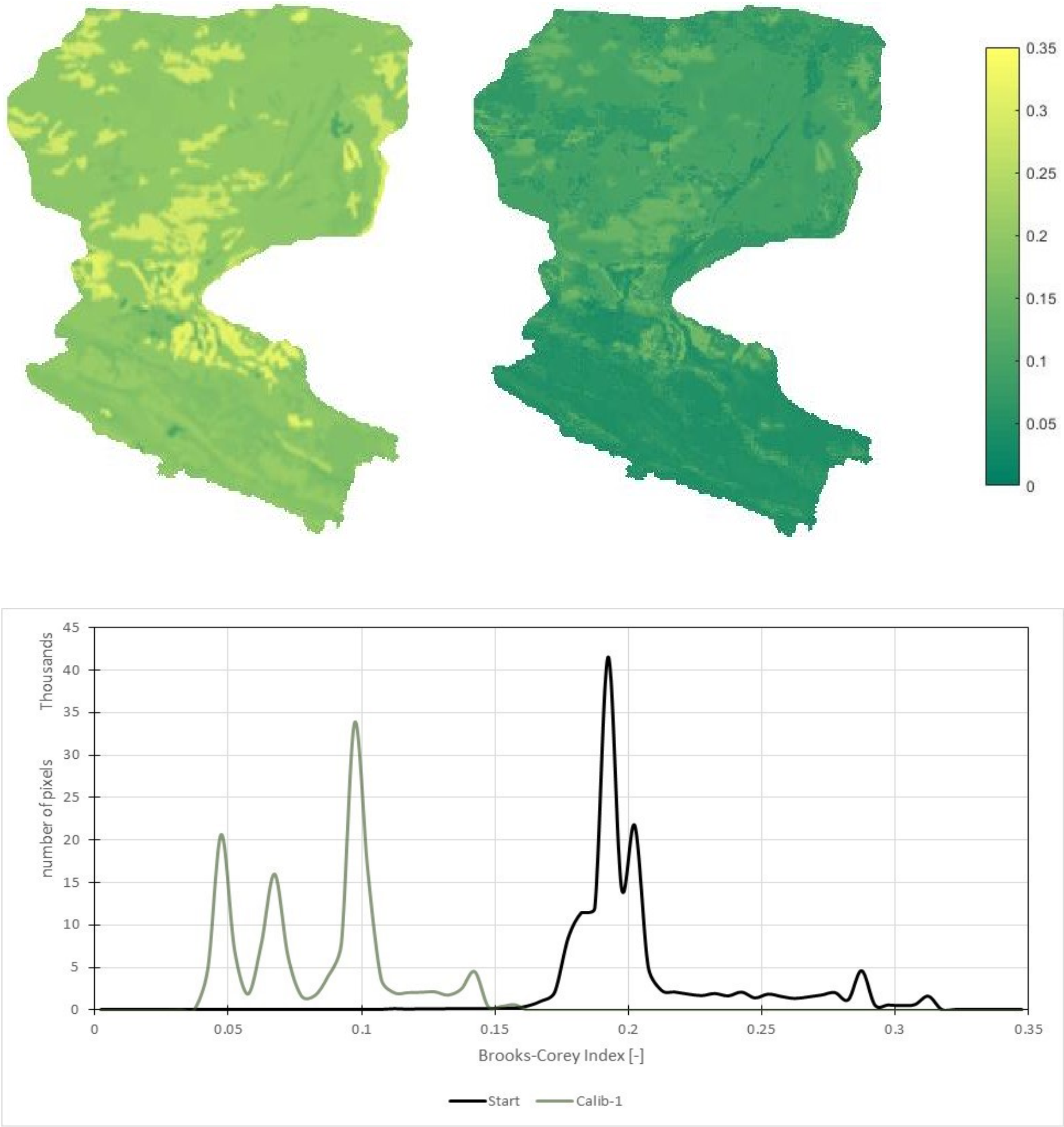

Figure 88 *- Brooks-Corey index maps and frequency plot. The input map on the left, the calibrated version on the right. The legend is adimensional.*

The pore-size distribution index has been strongly lowered for most values, in some cases even by a full order of magnitude. Since the degree of the parameter modification depends upon the temperature difference obtained for each pixel, the mountainous area has been the area more affected by calibration, in this case as for the other parameters.

4.5.2 Soil Depth

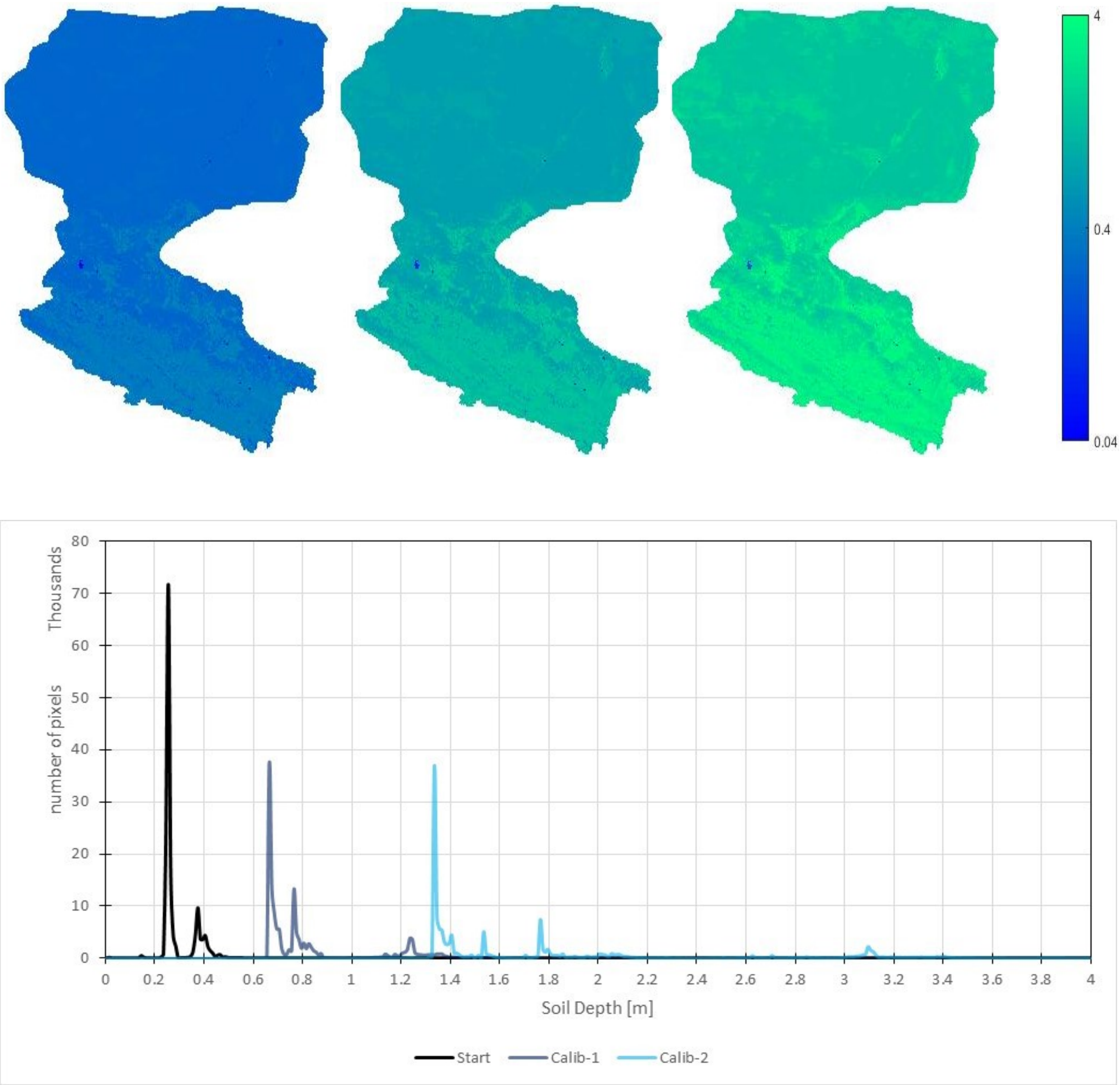

Figure 89 *- Soil depth maps and frequency plot. The input map on the left, the calibrated versions in the middle (calib-1) and on the right (calib-2). The legend (in logarithmic scale) is in meters [m].*

Soil depth is calibrated twice, each time more than doubling its value. As testified by the frequency plots, in the last calibration stage the values reach even 4m of soil depth. Once again, the most important increase is reserved for the mountainous area. The calibration process, in this case, has required a logarithmic scale to plot the different version of the parameter, as the changes were quite intense. Moreover, the starting plot was quite homogeneous, with a very high frequency for values around 0.3 m of depth; after the calibration, the parameter gained in heterogeneity, surely getting closer to reality.

4.5.3 Hydraulic Conductivity at saturation

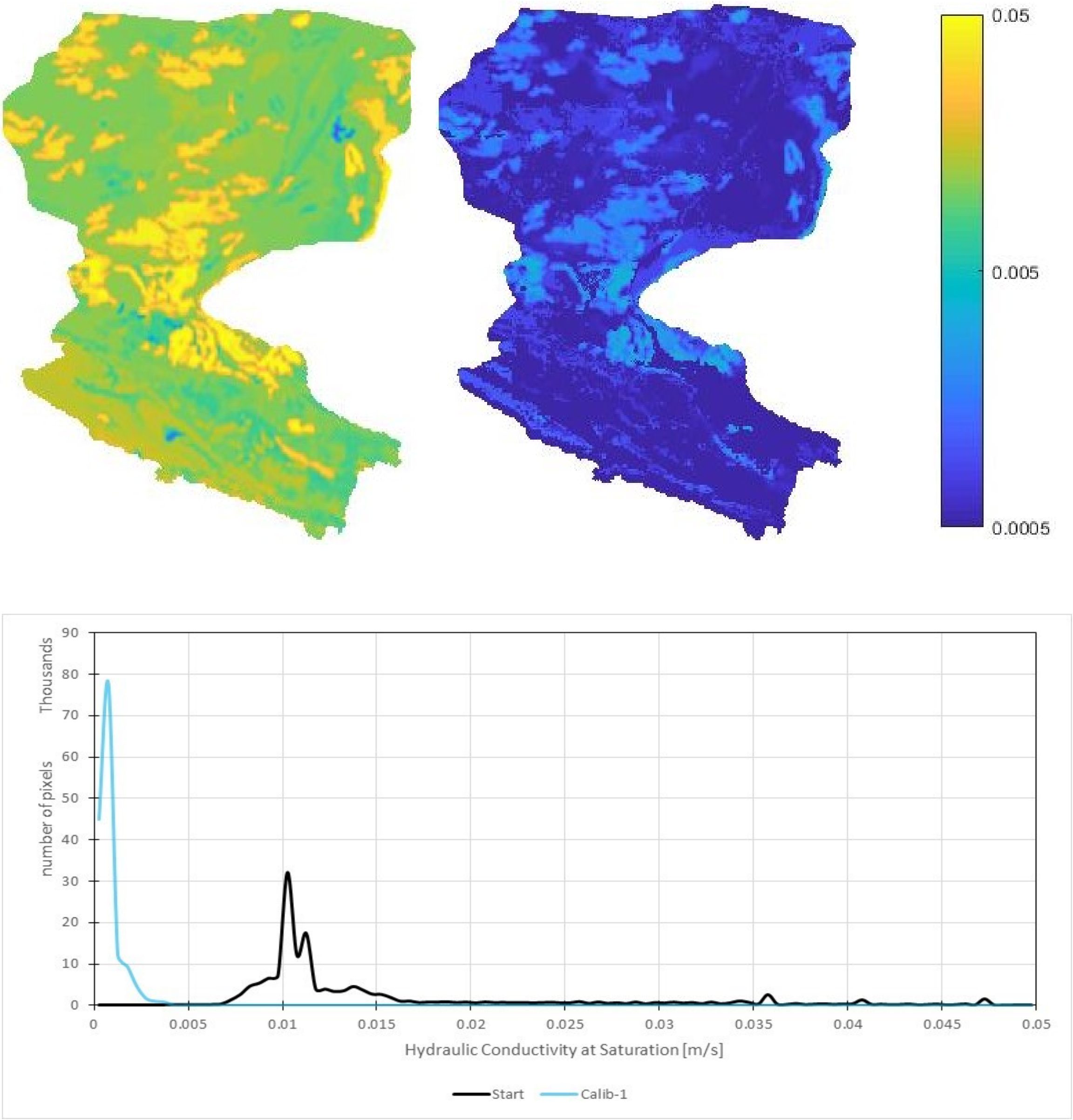

Figure 90 *- Hydraulic Conductivity at Saturation maps and frequency plot. The input map on the left, the calibrated version on the right. The legend (logarithmic scale) is in [m/s].*

Hydraulic conductivity is a parameter quite difficult to simulate, especially without point-wise on-field measurements. In this case, it has been lowered a lot (requiring a logarithmic sale for mapping), evidently because the particular structure of the soil matrix was not sufficiently interpreted by the input data.

4.5.4 Minimum stomatal resistance

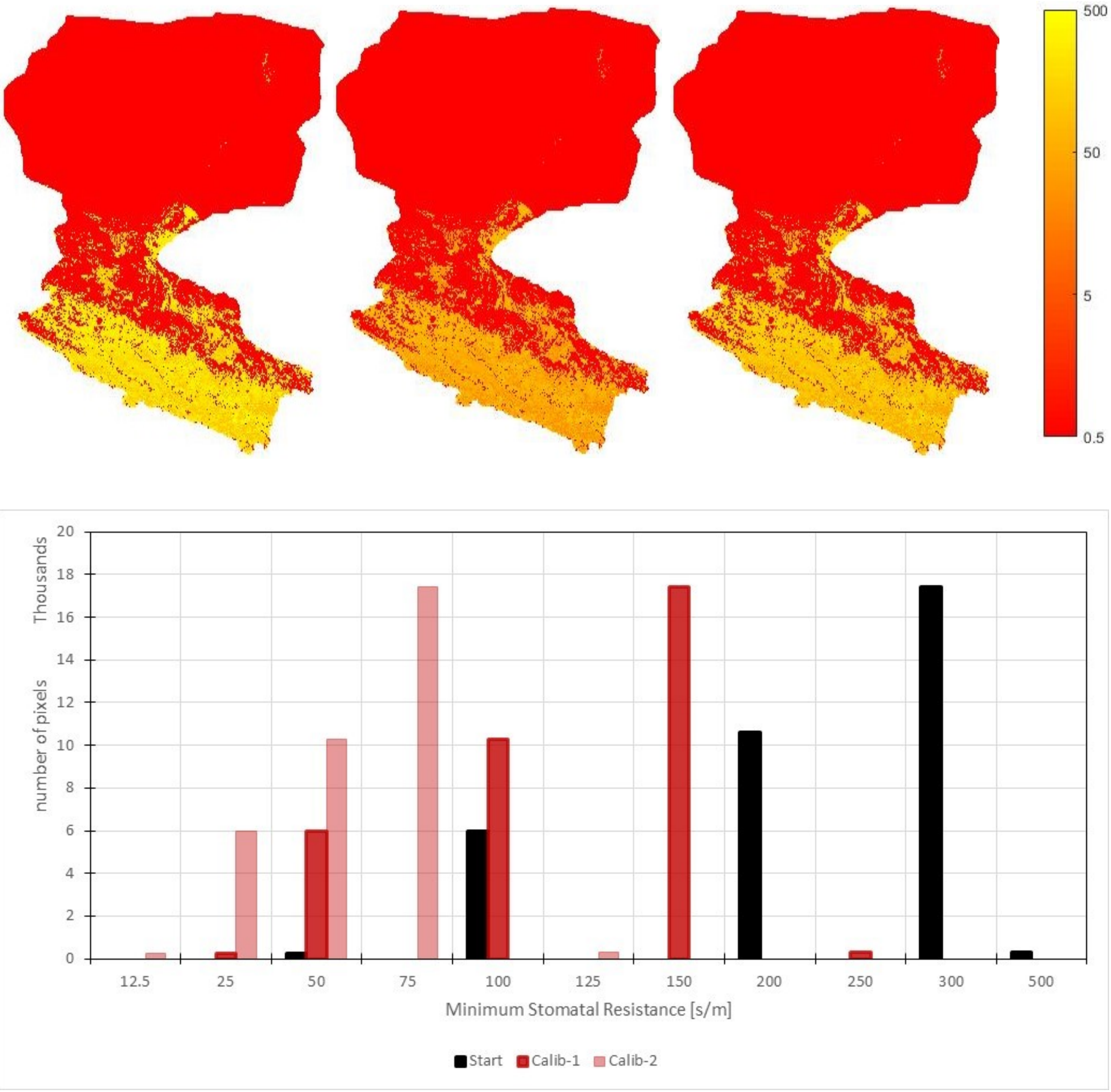

Figure 91 *- Minimum stomatal resistance maps and histogram. The input map on the left, the calibrated versions in the middle (calib-1) and on the right (calib-2). The legend is in [s/m].*

Minimum stomatal resistance has been calibrated twice because it has significant values for the vegetated area, so the mountainous sub-region. The values of this parameter are not continuous, so the (out-of-scale) frequency plot shows how starting values, quite high, are lowered down to the final values. Such low resistance to the transfer of water through the stomatal apparatuses of the leaves allows for more water to be transpired and a higher amount of the solar radiation to be absorbed by the leaf itself.

Conclusions & Recommendations

In this study, a survey of four Land Surface Temperature sources has been conducted, applying different downscaling techniques when necessary, with the aim of determining the most useful for the calibration of a distributed hydrological model on a Chinese inland river basin; lastly, the calibration has been performed.

Data from the ETM+ instrument aboard satellite LANDSAT 7, anyhow with high spatial resolution, provides too few images for a successful calibration, and cannot cover the whole basin in one single image. Data from MODIS instrument aboard Terra, resampled to a 30m resolution from its original 1000m, manages to provide high-quality data, especially when looking at desert data (the most frequent in the basin of interest). A temperature downscaling algorithm developed by Kustas provides data quality slightly inferior to MODIS, however requiring a more time-consuming computational effort; thus, MODIS is a better choice. An alternative downscaling algorithm, developed at TU Delft (Netherlands) and named "StarFM", tries to combine reflectance data from MODIS and ETM+ to obtain every day data at LANDSAT 7 high resolution. However accurate in its preceding applications, this algorithm has struggled when applied to a basin so extended, and with input data quality worsened by some technical problems with LANDSAT 7. Thus, because of its easily-retrieved data and its good performances, MODIS data has been selected for the calibration process of the distributed hydrological model FEST-EWB.

The calibration process has focussed on LST data from 2012, acting at pixel level and modifying four soil and vegetation parameters according to the error of the model with respect to MODIS measurements. Three steps have improved the statistics of the model, in particular in the first half of the year. The best results for the model are found around summer, while the poorest between late autumn and the winter season. This, together with the fact that only two autumn dates and just one winter date have been employed in this study, means that the application of the model and its calibration to these parts of the year require further studies.

This study leaves open a number of questions for further speculation: would a detailed analysis on snow dynamics and snow cover evolution during the year improve the results of the model? Which parameters can improve the LST estimates? Which is the accuracy of the meteorological inputs? How would an accurate knowledge of the irrigation volumes and schemes improve the simulations?

Bibliography

Akiyama et al, 2007 T. Akiyama, A. Sakai, Y. Yamazaki, G. Wang, K. Fujita, M. Nakawo, J. Kubota, Y. Konagaya – *"Surfacewater-groundwater interaction in the Heihe River basin, Northwestern China"* – Bulletin of Glaciological Research – 24 (2007): 87-94

Campo et al, 2012 L. Campo, F. Castelli, F. Caparrini, D. Entekhabi – *"An assimilation algorithm of satellite-derived LST observations for the operational production of soil moisture maps"* – IEEE International Geoscience and Remote Sensing Symposium, Remote Sensing for a Dynamic Earth – 22-27 July 2007

Arnold et al, 2012 J. Arnold, J. Kiniry, R. Srinivasan, J. Williams, E. Haney, S. Neitsch – *"Soil&Water Assessment Tool"* – Texas Water Resources Institute

Assouline, 2005 S. Assouline – *"On the relationships between the pore size distribution index and characteristics of the soil hydraulic functions"* – Water Resources Research – 41 (2005): W07019, doi:10.1029/2004WR003511

Bastiaanssen et al, 1998 Bastiaanssen, Menenti, Feddes, Holtslag – *"Remote sensing surface energy balance algorithm for land (SEBAL)"* – Journal of Hydrology, 212-213(1-4), 198-212.

Brooks-Corey, 1964 R. H. Brooks, A. T. Corey – *"Hydraulic properties of porous media"* – Hydrology Papers, Colorado State University – 3 (1964)

Coll et al, 2010 C. Coll, J. Galve, J. Sánchez, V. Caselles – *"Validation of Landsat-ETM Thermal-Band Calibration and Atmospheric Correction With Ground-Based Measurements"* – IEEE Transactions on Geoscience and Remote Sensing – Vol.48 (2010), 1

Corbari et al, 2008 C. Corbari, G. Ravazzani, J. Martinelli, M. Mancini – *"Elevation based correction of snow coverage retrieved from satellite images to improve model calibration"* – Hydrology and Earth System Sciences – 13 (2009): 639-649

Corbari et al, 2010 C. Corbari, J. A. Sobrino, M. Mancini, V. Hidalgo – *"Land surface temperature representativeness in a heterogeneous area through a distributed energy-water balance model and remote sensing data"* – Hydrology and Earth System Sciences – 14 (2010): 2141-2151

Corbari et al, 2012 C. Corbari, J. A. Sobrino, M. Mancini, V. Hidalgo – *"Mass and energy flux estimates at different spatial resolutions in a heterogeneous are through a distributed energy-water balance model and remote-sensing data"* – International Journal of Remote Sensing – (2013): 1-23

Corbari-Mancini et al, 2015 C. Corbari, M. Mancini, J. Li, Z. Su – *"Can satellite land surface temperature data be used similarly to river discharge measurements for distributed hydrological model calibration?"* – Hydrological Sciences Journal – Vol.60 (2015), n°2

Corbari et al, 2015 C. Corbari, W. Timmermans, A. Andreu – *"Intercomparison of Surface Energy Fluxes Estimates from the FEST-EWB and TSEB Models over the Heterogeneous REFLEX 2012 Site (Barrax, Spain)"* – Acta Geophysica – Vol.63 (2015), n°6: 1609-1638

Corbari-Mancini, 2014 C. Corbari, M. Mancini – *"Calibration and Validation of a Distributed Energy-Water Balance Model Using Satellite Data of Land Surface Temperature and Ground Discharge Measurements"* – Journal of Hydrometeorology – Vol.15 (2014)

Corbari-Ravazzani-Mancini, 2012 C. Corbari, G. Ravazzani, M. Mancini – *"A distributed thermodynamic model for energy and mass balance computation: FEST-EWB"* – Hydrological Processes – Vol.25 (2011): 1443-1452

Cuenca et al, 2013 R. H. Cuenca, S. P. Ciotti, Y. Hagimoto – *"Application of Landsat to Evaluate Effects of Irrigation Forbearance"* – Remote Sensing – Vol.5 (2013): 3776-3802

Cui et al, 2016 T. Cui, Y. Wang, R. Sun, C. Qiao, W. Fan, G. Jiang, L. Hao, L. Zhang – *"Estimating Vegetation Primary Production in the Heihe River Basin of China with Multi-Source and Multi-Scale Data"* – PloS ONE – Vol.11 (2016), n°4

de Boer, 2014 T. de Boer – *"Assessing the Accuracy of Water Temperature Determination and Monitoring of Inland Surface Waters Using Landsat 7 ETM+ Thermal Infrared Images*

– *A ase Study on the Rhine River, North Sea Canal, and Hollands Diep"* – MSc Thesis, Technische Universiteit Delft (NL)

Fan et al, 2016 J. Fan, Y. Wang, Z. Zhou, N. You, J. Meng – *"Dynamic Ecological Risk Assessment and Management of Land Use in the Middle Reaches of the Heihe River Based on Landscape Patterns and Spatial Statistics"* – Sustainability – Vol. 8 (2016): 536

Farg et al, 2016 E. Farg, S. Arafat, M. S. Abd El-Wahed, A. El-Gindy – *"Evaluation of water distribution under pivot irrigation systems using remote sensing imagery in eastern Nile delta"* – The Egyptian Journal of Remote Sensing and Space Sciences – Vol.20 (2017): S13-S19

Gao et al, 2006 F. Gao, J. Masek, M. Schwaller, F. Hall – *"On the Blending of the Landsat and MODIS Surfaces Reflectance: Predicting Daily Landsat Surface Reflectance"* – IEEE Transactions on Geoscience and Remote Sensing – Vol.44 (2006), n°8

Geng et al, 2015 X. Geng, X. Wang, H. Yan, Q. Zhang, G. Jin – *"Land Use/Land Cover Change Induced Impacts on Water Supply Service in the Upper Reach of Heihe River Basin"* – Sustainability – Vol.7 (2015): 366-383

Gutierrez et al, 2012 J. M. Gutiérrez, D. San-Martin, S. Brands, R. Manzanas, S. Herrera – *"Reassessing Statistical Downscaling Techniques for Their Robust Application under Climate Change Conditions"* – Journal of Climate – doi:10.1175/JCLI-D-11-00687.1

Hamlet et al, 2010 A. F. Hamlet, E. P. Salathé, P. Carrasco – *"Statistical Downscaling Techniques for Global Climate Model Simulations of Temperature and Precipitation with Application to Water Resources Planning Studies"* – Final Report for the Columbia Basin Climate Change Scenarios Project (2010)

Handbook of Hydrology VV.AA., David Maidment (editor in chief) – *"Handbook of Hydrology"* – Mcgraw-Hill, Inc. (1993)

Handcock et al, 2012 R. N. Handcock, C. E. Torgersen, K. A. Cherkauer, A. R. Gillespie, K. Tockner, R. N. Faux, J. Tan – *"Thermal Infrared Remote Sensing of Water Temperature in Riverine Landscapes"* – Fluvial Remote Sensing for Science and Management, First Edition – 2012, John Wiley & Sons, Ltd.

Herrero-Huerta et al, 2017 M. Herrero-Huerta, S. Lagüela, S. M. Alfieri, M. Menenti – *"Generating high-temporal and spatial resolution TIR image data"* – The International Archives of Photogrammetry, Remote Sensing and Spatial Information Sciences – Vol.XLII-2/W7 (2017)

Hu et al, 2017 N. Hu, X. Li, L. Luo, L. Zhang – *"Ancient Irrigation canals mapped from Corona Imageries and Their Implications in Juyan Oasis along the Silk Road"* – Sustainability – Vol.9 (2017) – 1283

Huang et al, 2017 S. Huang, Q. Feng, Z. Lu, X. Wen, R. C. Deo – *"Trend Analysis of Water Poverty Index for Assessment of Water Stress and Water Management Polices: A Case Study in the Hexi Corridor, China"* – Sustainability – Vol.9 (2017): 756

Huang, 2015 G. Huang – *"From Water-constrained to Water-driven Sustainable Development – A case of Water Policy Impact Evaluation"* – Sustainability – Vol.7 (2015): 8950-8964

Kustas et al, 2013 W. P. Kustas, J. M. Norman, M. C. Anderson, A. N. French – *"Estimating subpixel surface temperatures and energy fluxes from the vegetation index-radiometric temperature relationship"* – Remote Sensing of Environment – Vol.85 (2003): 429-440

Landsat 7 Handbook National Aeronautics and Space Administration – *"Landsat 7 Science Data Users Handbook"* - https://landsat.gsfc.nasa.gov/

Li et al, 2015 Z. Li, X. Deng, F. Wu, S. S. Hasan – *"Scenario Analysis for Water Resources in Response to Land Use change in the Middle and Upper Reaches of the Heihe River Basin"* – Sustainability – Vol.7 (2015): 3086-3108

Li et al, 2018 X. Li, G. Cheng, Y. Ge, H. Li, F. Han, X. Hu, W. Tian, Y. Tian, X. Pan, Y. Niang, Y. Zhang, Y. Ran, et al, - *"Hydrological Cycle in the Heihe River Basin and Its Implication for Water Resource Management in Endorheic Basins"* – Journal of Geophysical Research – Vol.123 (2018) n°2: 890-914

Liu et al, 2013 J. Liu, C. Zang, S. Tian, J. Liu, H. Yang, S. Jia, L. You, B. Liu, M. Zhang – *"Water conservancy project in China: Achievements, challenges and way forward"* – Global Environmental Change – 2013

Lu et al, 2017 L. Lu, C. Liu, X. Li, Y. Ran – *"Mapping the Soil Texture in the Heihe River Basin Based on Fuzzy Logic and Data Fusion"* – Sustainability – Vol.9 (2017): 1246

Mancini, 1990 M. Mancini – "La modellazione distribuita della risposta idrologica: effetti della variabilità spaziale e della scala di rappresentazione del fenomeno dell'assorbimento" – PhD Thesis – Politecnico di Milano (IT)

Montaldo-Albertson, 2001 N. Montaldo, J. D. Albertson – *"On the Use of the Force-Restore SVAT Model Formulation for Stratified Soils"* – Journal of Hyrometeorology – Vol.2 (2001)

Norman et al, 1995 J. M. Norman, W. P. Kustas, K. S. Humes – *"Source approach for estimating soil and vegetation energy fluxes in observations of directional radiometric surface temperature"* – Agr. Forest Meteorol. – Vol.77 (1995), n°3-4: 263-293

Pang et al, 2017 B. Pang, J. Yue, G. Zhao, Z. Xu – *"Statistical Downscaling of Temperature with the Random Forest Model"* – Hindawi, Advances of Meteorology – 2017

Parida et al, 2007 B. R. Parida, B. Oinam, N. R. Patel, N. Sharma, R. Kandwal, M. K. Hazarika – *"Land surface temperature variation in relation to vegetation type using MODIS satellite data in Gujurat state of India"* – International Journal of Remote Sensing – Vol.29 (2008), n°14: 4219-4235

Platonov et al, 2008 A. Platonov, P. S. Thenkabail, C. M. Biradar, X. Cai, M. Gumma, V. Dheeravath, Y. Cohen, V. Alchanatis, N. Goldshlager, E. Ben-Dor, J. Vithanage, H. Manthrithilake, S. Kendjabaev, S. Isaev – *"Water Productivity Mapping (WPM) Using Landsat ETM+ Data for the Irrigated croplands of the Syrdarya River Basin in central Asia"* – Sensors – Vol.8 (2008): 8156-8180

Rabuffetti et al, 2008 D. Rabuffetti, G. Ravazzani, C. Corbari, M. Mancini – *"Verification of operational Quantitative Discharge Forecast (QDF) for a regional warning system? The AMPHORE case studies in the upper Po River"* – Natural Hazards and Earth System Science – Vol.8 (2008), n°1: 166-173.

Schneider et al, 2012 S. Schneider, D. Mallants, D. Jacques – *"Determining hydraulic properties of concrete and mortar by inverse modelling"* – Materials Research Society – Vol.1475 (2012)

Senay et al, 2016 G. B. Senay, M. Friedrichs, R. K. Singh, N. M. Velpuri – *"Evaluating Landsat 8 evapotranspiration for water use mapping in the Colorado River Basin"* – Remote Sensing of Environment – Vol.185 (2016): 171-185

Shi et al, 2014 M. Shi, X. Wang, H. Yang, T. Wang – *"Pricing or Quota? A solution to water scarcity in Oasis Regions in China: A case study in the Heihe River Basin"* – Sustainability – Vol.6 (2014): 7601-7620

Shi et al, 2016 M. Shi, Y. Xie, Q. Cao – *"Spatiotemporal changes in rural settlement land and rural population in the middle basin of the Heihe River, China"* – Sustainability – Vol.8 (2016): 614

Smid-Costa, 2017 M. Smid, A. C. Costa – *"Climate projections and downscaling techniques: a discussion for impact studies in urban system"* – International Journal of Urban Sciences – 2017

Su, 2002 Z. Su – *"The Surface Energy Balance System (SEBS) for estimation of turbulent heat fluxes"* – Hydrology and Earth System Sciences – Vol.6 (2002), n°1: 85-99

Tan et al, 2016 J. Tan, P. Zhang, K. Lo, J. Li, S. Liu – *"The Urban Transition Performance of Resource-Based cities in Northeast China"* – Sustainability – Vol.8 (2016): 1022

Tarpanelli et al, 2011 A. Tarpanelli, L. Brocca, T. Lacava, M. Faruolo, F. Melone, T. Moramarco, N. Pergola, V. Tramutoli – *"River discharge estimation through MODIS data"* – Remote Sensing for Agriculture, Ecosystems, and Hydrology XIII – Vol.8174 (2011)

Timmermans et al, 2011 J. Timmermans, C. van der Tol, A. Verhoef, W. Verhoef, Z. Su, M. van Helvoirt, L. Wang – *"Quantifying the uncertainty in estimates of surface-atmosphere fluxes through joint evaluation of the SEBS and SCOPE models"* – Hydrology and Earth System Sciences Discussions – Vol.8 (2011): 2861-2893

Wang et al, 2009 L. Wang, T. Koike, K. Yang, P. Jen, G. Yeh – *"Assessment of a distributed biosphere hydrological model against streamflow and MODIS land surface temperature in the upper Tone River Basin"* – Journal of Hydrology – 2009

Wang et al, 2011 X. Wang, M. Ma, G. Huang, F. Veroustraete, Z. Zhang, Y. Song, J. Tan – *"Vegetation primary production estimation at maize and alpine meadow over the Heihe River Basin, China"* – International Journal of Applied Earth Observation and Geoinformation – 2001

Wang et al, 2015 Z. Wang, J. Yang, X. Deng, X. Lan – *"Optimal Water Resources Allocation under the Constraint of Land Use in the Heihe River Basin of China"* – Sustainability – Vol.7 (2015): 1558-1575

Weng et al, 2014 Q. Weng, P. Fu, F. Gao – *"Generating daily land surface temperature at Landsat resolution by fusing Landsat and MODIS data"* – Remote Sensing of Environment – Vol.145 (2014): 55-67

Wu et al, 2014 F. Wu, J. Zhan, Q. Zhang, Z. Sun, Z. Wang – *"Evaluating Impacts of Industrial Transformation on Water Consumption in the Heihe River Basin of Northwest China"* – Sustainability – Vol.6 (2014): 8283-8296

Yan et al, 2014 H. Yan, J. Zhan, B. Liu, Y. Yuan – *"Model Estimation of Water Use Efficiency for Soil Conservation in the Lower Heihe River Basin, Northwest China during 2000-2008"* – Sustainability – Vol.6 (2014): 6250-6266

Yang et al, 2015 Y. Yang, D. Long, H. Guan, W. Liang, C. Simmons, O. Batelaan – *"Comparison of three dual-source remote sensing evapotranspiration models during the MUSOEXE-12 campaign: Revisit of model physics"* – Water Resources Research – Vol.51 (2015): 3145-3165

Yi Teah et al, 2016 H. Yi Teah, T. Akiyama, R. San Carlos, O. Vargas Rayo, Y. Ting, J. Khew, S. Zhao, L. Zheng, M. Onuki – *"Assessment of Downscaling Planetary Boundaries to Semi-Arid Ecosystems with a Local Perception: A Case Study in the Middle Reaches of Heihe River"* – Sustainability – Vol.8 (2016): 1233

Yin et al, 2015 D. Yin, X. Li, Y. Huang, Y. Si, R. Bai – *"Identifying Vegetation Dynamics and Sensitivities in Response to Water Resource Management in the Heihe River Basin in China"* – Hindawi, Advances in Meteorology – Vol.2015: 861928

Yin et al, 2017 Z. Yin, Q. Feng, L. Yang, X. Wen, J. Si, S. Zou – *"Long Term Quantification of Climate and Land Cover Change Impacts on Streamflow in an Alpine River Catchment, Northwestern China"* – Sustainability – Vol.9 (2017): 1278

Zhang et al, 2014 G. Zhang, T. Yao, H. Xie, J. Qin, Q. Ye, Y. Dai, R. Guo – *"Estimating surface temperature changes of lakes in the Tibetan Plateau using MODIS LST data"* – Journal of Geophysical Research: Atmospheres – Vol.119 (2014)

Zhang et al, 2017 Y. Zhang, L. Zhang, J. Hou, J. Gu, C. Huang – *"Development of an Evapotranspiration Data Assimilation Technique for Streamflow Estimates: A Case Study in a Semi-Arid Region"* – Sustainability – Vol.9 (2017), 1658